

UC Berkeley

UC Berkeley Electronic Theses and Dissertations

Title

Engineering Dilute Nitride Semiconductor Alloys for Intermediate Band Solar Cells

Permalink

<https://escholarship.org/uc/item/3cg116f2>

Author

Luce, Alexander Vallejo

Publication Date

2015

Peer reviewed|Thesis/dissertation

**Engineering Dilute Nitride Semiconductor Alloys for Intermediate Band
Solar Cells**

by

Alexander Vallejo Luce

A dissertation submitted in partial satisfaction of the
requirements for the degree of
Doctor of Philosophy

in

Engineering-Materials Science and Engineering

in the

Graduate Division
of the
University of California, Berkeley

Committee in charge:

Professor Oscar D. Dubon, Co-Chair
Professor Junqiao Wu, Co-Chair
Professor Ali Javey

Spring 2015

**Engineering Dilute Nitride Semiconductor Alloys for Intermediate Band
Solar Cells**

Copyright 2015
by
Alexander Vallejo Luce

Abstract

Engineering Dilute Nitride Semiconductor Alloys for Intermediate Band Solar Cells

by

Alexander Vallejo Luce

Doctor of Philosophy in Engineering-Materials Science and Engineering

University of California, Berkeley

Professor Oscar D. Dubon, Co-Chair

Professor Junqiao Wu, Co-Chair

The growth and characterization of GaAs nanowires and GaNPAs thin-films is discussed within the context of finding a material system that is suitable as an intermediate band solar cell (IBSC) absorber. The IBSC is an attractive concept proposed to exceed the Shockley-Queisser detailed balance limit for photovoltaic efficiency. These solar cells have an additional intermediate band, allowing for the absorption of below bandgap photons, thus resulting in an increase in photocurrent and higher efficiency. Suitable materials systems for the implementation of the IBSC concept, however, are presently lacking. Recent work on the highly-mismatched alloy (HMA) GaAsN has shown that the unique features of the electronic band structure demonstrate optical activity of three energy bands and have led to the realization of a proof-of-concept IBSC. GaAsN, however, is not without shortcomings. Another HMA material, GaNPAs, which offers a wide range of bandgap tunability and is better matched to the solar spectrum is proposed. This work covers the optical characterization of both GaAs nanowires and GaAsPN using traditional visible-light semiconductor characterization techniques including optical absorption spectroscopy, photo-modulated reflectance, steady-state photoluminescence, and spectral photoconductivity. Additionally, photovoltaic devices based on GaNPAs are demonstrated and assessed as potential IBSCs.

Contents

List of Figures	v
List of Tables	x
Notation and Symbols	xi
1 Introduction	1
1.1 The 12 million mile problem	2
1.1.1 A moonshot for solar	3
1.2 Introduction to Photovoltaics	3
1.2.1 The Shockley-Queisser limit	3
1.3 Third-generation photovoltaics: beyond the Shockley-Queisser limit	6
1.4 Organization of this dissertation	6
2 Intermediate band solar cells	8
2.1 Introduction	9
2.2 Theory	9
2.2.1 The effect of concentration	10
2.2.1.1 Low injection	12
2.2.2 IBSC efficiency with a realistic solar spectrum	12
2.3 Key technical challenges	13
2.3.1 Identification of semiconductor material systems that result in intermediate bands	13
2.3.2 Selecting high-quality absorber materials	14
2.4 Experimental efforts	15
2.4.1 Quantum dots	15
2.4.2 Highly-mismatched alloys	18
2.5 Summary of requirements for viable intermediate band solar cells	20
2.6 Summary	21
3 Dilute nitride nanowires	22
3.1 Background	23

3.1.1	Nanowires for PV	23
3.1.2	Growth	24
3.2	Molecular Beam Epitaxy Growth of III-V and highly-mismatched alloy nanowires	25
3.2.1	Growth of GaAs nanowires	27
3.2.2	Growth of GaAsN nanowires	27
	3.2.2.1 Core-shell GaAs/GaAsN nanowires	27
	3.2.2.2 Axial GaAs/GaAsN nanowires	28
3.3	Structural Characterization	29
3.3.1	X-ray diffraction	29
3.3.2	GaAs Nanowires	30
3.3.3	GaAs/GaAsN nanowires	32
	3.3.3.1 Core-shell GaAs/GaAsN nanowires	32
3.4	Optical Characterization	32
3.4.1	Photoluminescence	33
	3.4.1.1 Transferred Nanowires	34
3.4.2	Photoreflectance	37
	3.4.2.1 Experimental Description	37
	3.4.2.2 Results	38
3.5	Outlook	41
4	Electronic band structure of GaNPAs	42
4.1	Theory	43
	4.1.1 Band anticrossing model	43
	4.1.2 Density of states	45
	4.1.3 Optimum GaNPAs alloy composition for IBSC application	48
	4.1.4 k.p calculation	49
4.2	Growth of GaNPAs thin films	49
4.3	Optical measurements	52
	4.3.1 Experimental setup	52
	4.3.2 Photoluminescence	52
	4.3.3 Photoreflectance	53
	4.3.3.1 Influence of thermal annealing	56
	4.3.4 Absorption	57
4.4	Conclusion	60
5	Towards GaNPAs based IBSC devices	61
5.1	Introduction	62
5.2	Growth of doped GaNPAs layers	62
	5.2.1 Growth of doped GaNPAs layers	62
5.3	Characterization of doped GaNPAs layers	62
	5.3.1 Electrical properties	62

5.3.2	Optical properties	64
5.3.3	Time-resolved PL	64
5.4	Design of GaNAsP IBSC device	64
5.5	Construction of GaNAsP IBSC device	69
5.6	Characterization of IBSC devices	69
5.6.1	EQE	69
5.6.2	JV characteristics	71
5.6.3	Two photon excitation	72
5.7	Conclusion	74
6	Conclusions and future directions	75
	Bibliography	77
A	Additional data and figures	88
A.1	Selected Properties of III-V Semiconductors	89
A.2	$\text{GaN}_x\text{P}_{1-x-y}\text{As}_y$	90
A.3	k.p calculation of GaNPAs bandstructure	92
B	Growth of GaAs nanowires on patterned silicon substrates	93
B.1	Background	94
B.2	Femto-second laser patterning of silicon (111)	94
B.3	Results	94
C	Transmission Electron Microscopy of GaAs Nanowires	100
D	<i>Mathematica</i> code	108

List of Figures

1.1	Area required to meet global energy needs with photovoltaics, assuming 8% conversion efficiency. Original calculation by Matthias Loster [1]. . . .	2
1.2	Current-voltage curve for a solar cell. At zero voltage, the current is equal to the short circuit current (J_{SC}). At zero current, the voltage is equal to the open circuit voltage (V_{OC}). The power delivered to the external load is determined by the maximum power point (Max PP). Figure courtesy of Greg Brown.	4
1.3	The “Three Generations” of Photovoltaics, as a Function of Cost and Efficiency. The ‘Present Limit’ is the SQ limit for a single junction cell, and the ‘Thermodynamic Limit’ is the maximal possible efficiency achievable under concentration. From Ref. [2].	4
1.4	The efficiency limit, η , for an ideal solar cell with a single bandgap.	5
1.5	Fundamental loss processes in a standard solar cell.	5
1.6	PV loss processes. Adapted from S. Byrnes [3].	6
2.1	In a conventional PV, there is only one primary optical transition. In an intermediate band PV, the primary optical transition is augmented by an additional sequential series of lower-energy photon absorptions that can also promote a carrier across the bandgap.	9
2.2	IBSC band diagram using the notation defined in ref. [4].	10
2.3	Contour plot of ideal IBSC efficiency limit (shown in the color bar) calculated as a function of both the total bandgap ϵ_G , and smaller bandgap ϵ_I	11
2.4	Effect of concentration factor X on the short circuit current density of a GaAs-based IBSC. From [5]	13
2.5	Efficiency contour plots for ideal IBSC under AM 1.5 irradiation. From [6].	14
2.6	Representative energy band diagram of an IBSC shown alongside the solar spectrum.	16
2.7	Columns III-VI of the periodic table relevant to the semiconductors in this work. Shown are the Pauling scale of electronegativity and the atomic radius.	17

2.8	Band structure calculation using the band anticrossing model for the nitrogen defect level in (a) the conduction band, such as GaAsN; and (b) below the conduction band, such as GaNPAs. Figure courtesy of R. Broesler. . . .	17
2.9	Calculated efficiency of ideal GaAs _{1-x} N _x IBSC as a function of N concentration, x	19
2.10	Band offsets relative to vacuum of the GaAs _{1-y} P _y alloy system for $y = 40\%$ (left), and schematic band structure showing the nitrogen level and the Γ and X CB minima.	19
2.11	Calculated $E [k]$ diagram for dilute-nitride GaAsPN with $\sim 2\%$ nitrogen. The interaction with localized N states splits the original host GaAsP conduction band into lower (E_-) and upper (E_+) conduction sub-bands, which become the IB and CB, respectively, in the intermediate band solar cell device scheme. The 3 allowed optical transitions are also shown.	20
3.1	Calculated efficiency (η) as a function of nitrogen concentration for an ideal IBSC based on GaAsN nanowires.	24
3.2	Schematic of MBE growth fitted with DC constricted plasma source for N. Adapted from [7].	26
3.3	The DC constricted plasma source.	26
3.4	Diagram of X-ray diffraction	29
3.5	XRD symmetric $2\theta-\omega$ scan of GaAs (A.17) and GaAsN(A.19). Shown are the Si(111) peak from the substrate at 28.5 degrees, and zinc-blende GaAs peak, which shifts from 27.2 degrees to 27.4 degrees with increasing nitrogen concentration.	30
3.6	SEM images of GaAs NW's.	31
3.7	(a) SEM image of Type B GaAs nanowire transferred to silicon wafer. The wires shown are approximately 1-1.2 μm in length. Scale bar: 500nm. (b) EDAX spectra of GaAs nanowire body. The large silicon peak is due to the Si substrate.	31
3.8	GaAs/GaAsN core-shell nanowires grown with plasma current $I = 10\text{mA}$ and flow rate $F = 1.5$ SCCM.	32
3.9	GaAs/GaAsN core-shell nanowires grown with plasma current $I = 40\text{mA}$ and flow rate $F = 1.0$ SCCM.	32
3.10	GaAs/GaAsN axial nanowires grown with plasma current $I = 10\text{mA}$ and flow rate $F = 2.0$ SCCM.	33
3.11	PL spectra of single GaAs nanowire at different excitation power from 50 μW to 1 mW at $T = 4$ K. Inset shows the excitation power dependence of the PL intensity for the 1.48eV peak (wurtzite phase) and the 1.52 eV phase (zinc blende phase).	35
3.12	PL spectra of GaAsN nanowire array at 4 K, with inset showing the excitation power dependence of the PL intensity of the GaAsN nanowire array.	36
3.13	Micro-PL spectra of single GaAsN nanowire at $T = 4$ K.	37

3.14	PR spectra of GaAs nanowires together with fitted curve (solid line) and decomposition of the individual modulus of PR resonance.	39
3.15	PR spectra of GaAsN nanowires together with fitted curve (solid line) and decomposition of the individual modulus of PR resonance. Inset: root-mean-squared curve-fitting error for different m relative to $m=3$	40
4.1	Illustration of simple 2 level system.	44
4.2	Calculated DOS of (a) $\text{GaN}_x\text{As}_{1-x}$ and (b) $\text{GaN}_x\text{P}_{0.4}\text{As}_{0.6-x}$ for different N content x . The dashed vertical lines indicate the position of the N level in the matrix materials.	47
4.3	Energy gap between the top of valence band and the bottom of conduction band at the Γ (solid black line), X (dashed green line), and L (dashed blue line) points for GaPAs (thin lines) and $\text{GaN}_{0.02}\text{P}_y\text{As}_{0.98-y}$ (thick lines) alloys with various P concentrations. The solid red line shows the position of nitrogen level in GaPAs host.	48
4.4	Band structure of $\text{GaP}_{0.4}\text{As}_{0.6}$ host (grey lines) obtained within the 8-band $\mathbf{k} \cdot \mathbf{p}$ model and $\text{GaN}_{0.02}\text{P}_{0.40}\text{As}_{0.58}$ (black lines) calculated within the BAC model with following parameters: $E_N=1.86\text{eV}$, $V_{N\Gamma}=2.84\text{eV}$, and $V_{NX} = C_{NL} = C_{N\Gamma}/4$	49
4.5	(a) Overview of gas source MBE used for growth of metamorphic GaNAsP samples, courtesy Y. Kuang, UCSD. (b) RHEED images from sample growth.	50
4.6	The designed structure (left) of GaNPAs and the measured composition profile by Rutherford back scatteringspectrometry and nuclear reaction analysis (right).	51
4.7	(a) RBS measurement geometry, image courtesy K.M. Yu. (b) Channeling RBS measurement of and (c) channeling NRA of $\text{GaN}_{0.015}\text{P}_{0.445}\text{As}_{0.54}$ sample.	51
4.8	Room-temperature photoluminescence of GaAsP (S205A), GaNAsP (S205B) and GaNAsP after rapid thermal annealing (S205B RTA).	53
4.9	Room-temperature photoreflectance and absorption spectra for $\text{GaP}_{0.46}\text{As}_{0.54}$ (a), as-grown $\text{GaN}_{0.015}\text{P}_{0.445}\text{As}_{0.54}$ (b), and annealed $\text{GaN}_{0.015}\text{P}_{0.445}\text{As}_{0.54}$ (c) samples.	54
4.10	Room-temperature photoreflectance and absorption spectra for $\text{GaP}_{0.38}\text{As}_{0.62}$ (a), as-grown $\text{GaN}_{0.012}\text{P}_{0.38}\text{As}_{0.608}$ (b), and annealed $\text{GaN}_{0.012}\text{P}_{0.38}\text{As}_{0.608}$ (c) samples.	55
4.11	Energies of the E_1 and E_+ transitions for as-grown (solid points) and annealed (open points) GaNPAs layers, along with theoretical predictions obtained within the BAC model.	57
4.12	Absorption coefficients of GaAsP (S205A) and GaNAsP (S205B) samples.	58
4.13	(a) Room-temperature absorption spectra of GaNPAs samples of various contents. (b) Absorption coefficient α_0 determined for GaNPAs alloys of various contents.	59

5.1	Resistivity and mobility of n-type doped GaAsPN:Si.	63
5.2	Photoreflectance of n-type doped GaNPAs, showing evidence of both the VB E_- and VB to E_+ transitions. At higher electron concentrations, the modulation band-bending is drastically decreased.	65
5.3	Photoreflectance of n-type (b,c,d), and p-type (e,f) doped GaNPAs samples. At higher electron concentrations, the modulation band-bending is drastically decreased and the spectral features associated with transitions from VB to either E_- or E_+ are absent.	66
5.4	Illustrative band diagram of (a) undoped GaNPAs sample and (b) n-type GaNPAs:Si, which much higher band bending at the surface as a result of the formation of a surface depletion layer.	67
5.5	Band diagram depicting the change in band bending in (a) Si doped GaNPAs with a dopant concentration of n_1 and a depletion layer width of d_1 , and (b) band-bending for the case of higher dopant concentration n_2 , where $n_2 > n_1$, and the resulting depletion layer width $d_2 < d_1$	67
5.6	Block diagram of IBSC structures with (left) and without (right) an electron blocking layer to electrically isolate the IB.	68
5.7	The completed GaNAsP IBSC device mounted on a glass slide. The device measures	69
5.8	Photoreflectance (top) and EQE of Blocked Intermediate Band (BIB) GaNAsP based IBSC.	70
5.9	J-V curve of Blocked Intermediate Band (BIB) and Unblocked Intermediate Band (UIB) GaNAsP structures.	71
5.10	2-photon excitation (TPE) for intermediate band solar cell. (a) Schematic band diagram of 2-photon excitation experiment. (b) Overview of the 2-photon excitation experiment design.	72
5.11	Change in quantum efficiency (QE) as result of illumination with IR light source	73
A.1	Calculated energy positions of the N level and the Γ , X, and L conduction bands of the GaAs $_{1-y}$ Py alloy system. At a P content y of > 0.3 the local N level E_N drops below the conduction band E_Γ , creating the conditions required to make a multiband semiconductor. An upper limit to the P content is set by the appearance of an indirect band gap ($E_X < E_\Gamma$) at $y > 0.5$. Figure from [8].	90
A.2	GaN $_x$ As $_y$ P $_{1-x-y}$: Target Composition	91
B.1	Patterning conditions used on silicon (111) substrate.	95
B.2	Resulting dot size with respect to laser pulse energy used.	96
B.3	Detail of dot with 1.1 μ m diameter.	97
B.4	Detail view of the region with 1 μ m diameter dots. Nanowires can be seen protruding from the laser-patterned dots.	98

B.5	Detail of both a corner (left) and edge (right) showing the GaAs growth is primarily over the patterned region. The spots that form on the outside could be due to dust deposits on the surface.	99
B.6	EDX linescan of the post-growth sample confirming the gallium arsenide content is selectively deposited. Red, green, and blue denote the concentration of Ga,As, and Si along the line, respectively.	99
C.1	Low magnification TEM image of a ~53nm diameter GaAs NW.	102
C.2	TEM image of GaAs nanowire showing detail of tip and stacking faults near the tip.	103
C.3	Selective area diffraction pattern (SADP) of GaAs NW showing ZB type diffraction pattern.	104
C.4	High-magnification TEM image of GaAs nanowire showing stacking faults.	105
C.5	Bright field (BF) TEM image of GaAs NW.	106
C.6	FFT images of BF and DF TEM images.	107

List of Tables

2.1	Conditions necessary for an ideal IBSC, from Ref. [4]	11
2.2	Summary of approaches towards realization of IBSCs	16
3.1	Published growth conditions for III-V nanowires	28
3.2	Nanowire growth conditions	29
3.3	Nanowire transfer methods	34
4.1	Materials parameters used in DOS calculations	47
5.1	measured IBSC J-V characteristics	72

Notation and Symbols

α_0	absorption coefficient
Δ_{SO}	Spin-orbit splitting energy
η	Efficiency
χ	Electron affinity
BAC	Band anticrossing
BEP	Beam equivalent pressure
BIB	Blocked intermediate band
BTU	British thermal unit
c	Speed of light
CB	Conduction band
CPV	Concentrating photovoltaic
DNI	Direct normal irradiance
DOS	Density of states
e	Electron charge
E	Energy
E_-	Lower conduction sub-band
E_+	Upper conduction sub-band
E_F	Fermi energy
E_{FS}	Fermi stabilization energy

E_g	Bandgap energy
E_M	Energy of host matrix
E_N	Energy of nitrogen (defect) level
EBL	Electron blocking layer
EDAX	Energy dispersive x-ray analysis
EQE	External quantum efficiency
FF	Fill factor
FWHM	Full width at half maximum
h	Planck's constant
HMA	Highly-mismatched alloy
I	Current
III-V	compound semiconductor consisting of group III and V elements
IB	Intermediate band
IBSC	Intermediate band solar cell
J	Current density
J_{sc}	Short circuit current density
k	electron wave vector
k_B	Boltzmann constant
K	Kelvin, unit of temperature
LED	Light emitting diode
m_0	Electron rest mass
m_e^*	Electron effective mass
m_{hh}	Mass of heavy holes
m_{hh}	Mass of split-off valence band
MBE	Molecular beam epitaxy

MOCVD	Metal organic chemical vapor deposition
n	Electron concentration
n_c	Free carrier concentration
N_A	Acceptor concentration
N_D	Donor concentration
n_r	Index of refraction
NRA	Nuclear reaction analysis
NW	Nanowire
PL	Photoluminescence
PR	Photoreflectance
PV	Photovoltaic
q	Fundamental unit of charge
QD	Quantum dot
QE	Quantum efficiency
QW	Quantum well
R	Molar gas constant
RBS	Rutherford backscattering spectrometry
RTA	Rapid thermal anneal
SEM	Scanning electron microscope
SO	Split-off valence band
SQ	Shockley-Queisser
SRH	Shockley Reed Hall
t	Film thickness
T	Temperature
T_a	Solar absorber operating temperature

TEA	Techno-economic analysis
TEM	Transmission electron microscopy
TRPL	Time-resolved photoluminescence
TW	Terawatt (10^{12} watt)
UIB	Unblocked intermediate band
V	Voltage
VB	Valence band
V_{MN}	Coupling constant
x	Nitrogen content
XRD	X-ray diffraction
y	Phosphorus content
Z	Atomic number

Chapter 1

Introduction

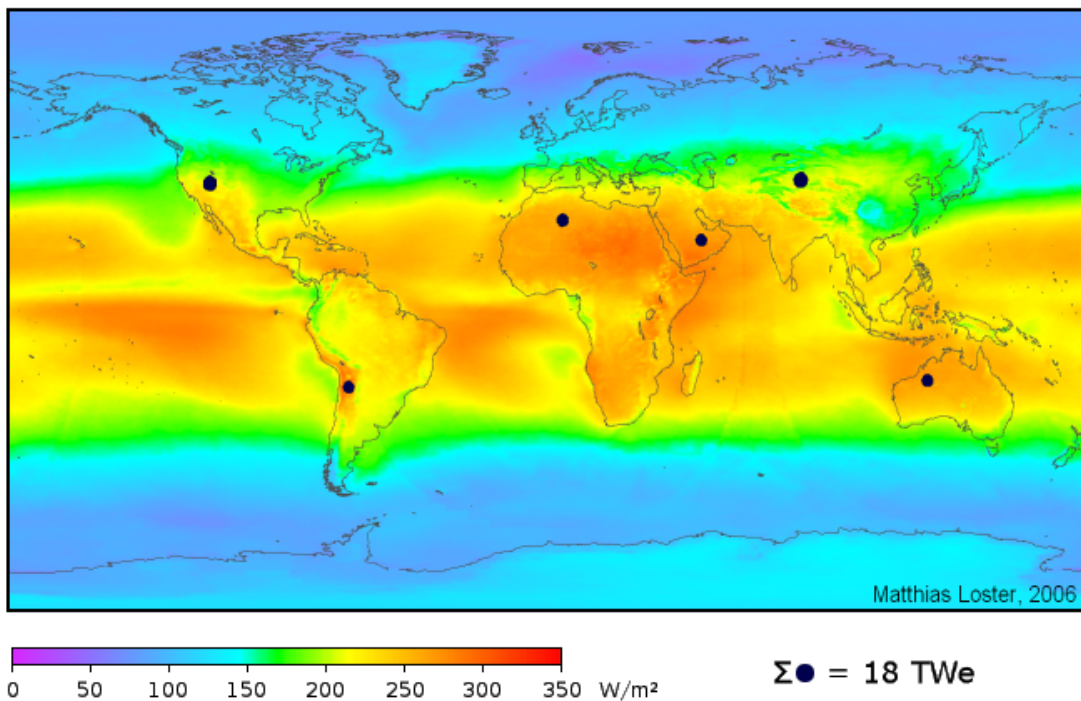


Figure 1.1: Area required to meet global energy needs with photovoltaics, assuming 8% conversion efficiency. Original calculation by Matthias Loster [1].

1.1 The 12 million mile problem

In the year 2012, the equivalent of nearly 9,000 million tons of oil¹ were consumed as energy worldwide[9]. The magnitude of this number sounds staggering. In comparison, however, it is less than half of the total energy from the sun that hits the earth in just one hour. In spite of this, the amount of actual energy generated from solar power sources, both photovoltaics (PV) and concentrated solar power (CSP), accounts for the equivalent of just 3 of those 9,000 million tons. The majority of energy supplied bring from non-renewable resources such as coal, oil, and gas.

Given the amount of sunlight hitting the earth, it becomes a nice exercise to consider a scenario where all of the worlds energy needs could be met by solar power². Suppose that massive solar farms are placed in the desert, in areas having high sunlight and little population. These solar farms, each of which has a conversion efficiency of only 8%, taken

¹18,979 million tons of oil equivalent (Mtoe) per year is approximately 12 TW.

²Accounting for differences in energy supply and energy consumption arising from energy loss, the global need is about 20 TW per year.

together could supply all of the energy needed worldwide. This calculation has been done before and is shown in Figure 1.1. However, the amount of land masse in one single solar farm, shown as black disc on the map³, small as though it may seem, is greater than that of all the paved roads in the entire world, or 12 million miles of pavement.

Solar power though, if done cheaply, is still poised to become a significant source of electricity generation in the future. In fact, the International Energy Agency estimates that between 6-10% of all electricity generation worldwide could come from solar power by 2035, depending on the policy environment in place[9]. For solar PV, this would be a 26-fold increase since 2010. Clearly, improved solar technologies, when coupled with a supportive policy and economic environment, are needed to meet these projections.

1.1.1 A moonshot for solar

In 2010, the United States Department of Energy set out to make solar electricity cost competitive with electricity from non-renewable resources in the U.S. The result of this was the Sunshot Program, launched in 2011, with the goal of achieving a \$1/Watt installed system price for utility scale PV by 2020. This \$1/W price would enable PV to provide 14% of the energy across the country by 2030. To do this, however, requires that significant barriers to integrating high penetrations of PV on the grid, from generation to distribution and transmission, be overcome[10].

1.2 Introduction to Photovoltaics

A substantive introduction to solar cell device operation can be found in numerous textbooks, e.g., Refs. [11, 12, 13], The following is meant to be an overview of only the key fundamental principles related to this dissertation.

1.2.1 The Shockley-Queisser limit

The theoretical maximum efficiency of a single junction solar cell can be calculated using the detailed balance model first introduced by Shockley and Queisser, with the maximum efficiency at a given bandgap typically referred to as the Shockley-Queisser (SQ) limit [14]. Figure 1.4 plots the efficiency limit, η , for an ideal solar cell with a single bandgap according to the detailed balance model. In order to determine the efficiency limit of a single junction PV, the assumptions are as follows:

1. The absorption of one photon produces only one electron-hole pair. Thus the quantum yield is 1.
2. Only photons with energy greater than the bandgap energy, $h\nu > E_g$, are absorbed.

³About 160,000 square km in area.

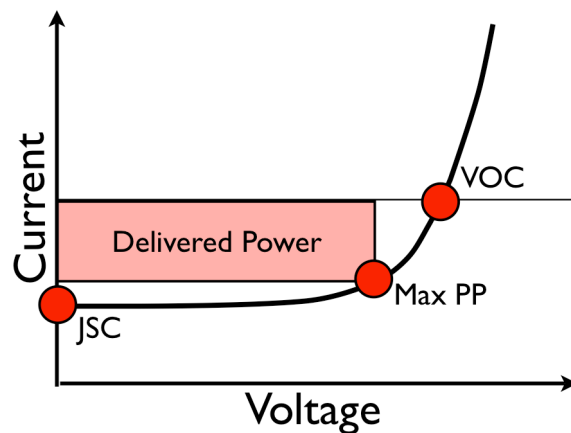


Figure 1.2: Current-voltage curve for a solar cell. At zero voltage, the current is equal to the short circuit current (J_{SC}). At zero current, the voltage is equal to the open circuit voltage (V_{OC}). The power delivered to the external load is determined by the maximum power point (Max PP). Figure courtesy of Greg Brown.

PV Power Costs as Function of Module Efficiency and Cost

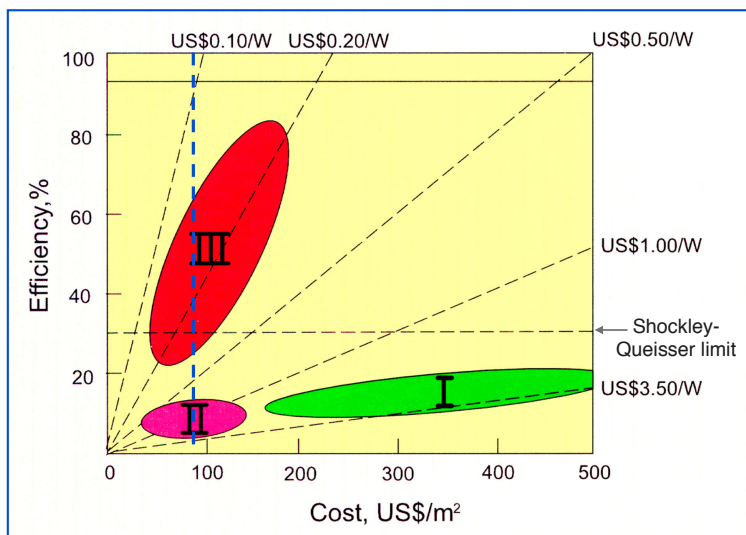


Figure 1.3: The “Thee Generations” of Photovoltaics, as a Function of Cost and Efficiency. The ‘Present Limit’ is the SQ limit for a single junction cell, and the ‘Thermodynamic Limit’ is the maximal possible efficiency achievable under concentration. From Ref. [2].

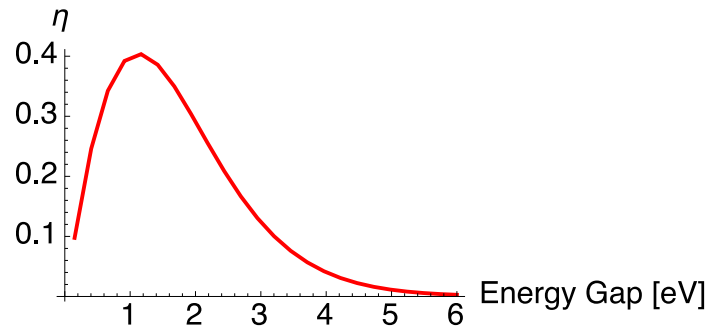


Figure 1.4: The efficiency limit, η , for an ideal solar cell with a single bandgap.

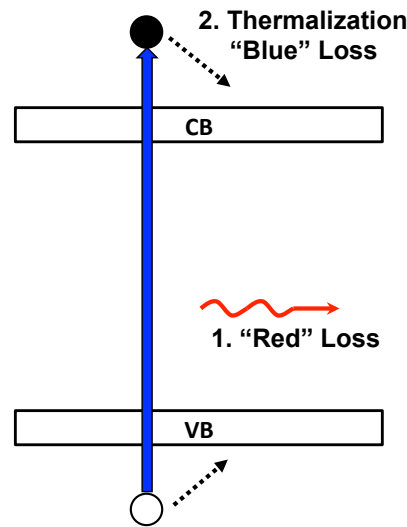


Figure 1.5: Fundamental loss processes in a standard solar cell.

3. Radiative recombination is the only recombination mechanism present.
4. Hot carriers relax down to the band edges through thermalization.
5. The quasi-Fermi level separation throughout the cell is constant. This results in infinite carrier mobility.

Figure 1.5 shows two fundamental loss process in a standard single junction solar cell: (1) “Red” loss, and (2) “Blue” or thermalization loss. Red loss is due to the inability of the semiconductor to absorb below bandgap photons, since it is transparent to photons with energy $h\nu < E_g$. Thermalization loss is due to the fact that photons with higher energy $h\nu \gg E_g$ will relax back to the band edges. Thus only a fraction of the energy they carry, i.e., that equals the bandgap energy⁴, is converted. Not shown are losses due

⁴Actually, this value multiplied by a Carnot factor.

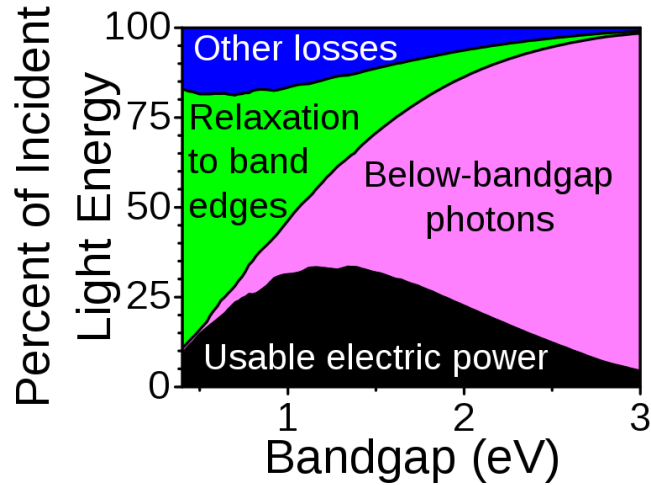


Figure 1.6: PV loss processes. Adapted from S. Byrnes [3].

to the (3) junction, (4) contact voltage, and (5) recombination[2]. However, as shown by Figure 1.6, both red loss and blue loss make up the overwhelming majority of the incident energy lost in PV conversion.

1.3 Third-generation photovoltaics: beyond the Shockley-Queisser limit

This dissertation will focus on two approaches to “beat” the Shockley-Queisser limit through materials engineering of dilute nitride semiconductors. The first, intermediate band nanowires, seeks to couple a material system with very high light absorption (due to the geometry of the nanowires), with bandgap engineering through the use of highly-mismatched semiconductor alloys. The second, intermediate band semiconductors based on the GaNPAs system, presents our work towards achieving a working intermediate band PV device, all the way from theory and basic materials characterization, through device engineering and characterization under a solar simulator.

1.4 Organization of this dissertation

The remainder of this dissertation is organized as follows. Chapter 2 introduces the concept of the intermediate band solar cell (IBSC) and introduces several materials approaches for the realization of IBSCs. Also, an overview of highly-mismatched alloys (HMAs) and, in particular, dilute nitride semiconductors is given. Chapter 3 covers the experimental growth and characterization of III-V HMA nanowires (NW). Samples were grown at the UC Berkeley Integrated Materials Lab. Chapter 4 introduces the HMA

GaNPs alloy system, and presents calculations and experimental results assessing the suitability of its electronic structure for IBSC application. GaNPs samples were grown at the University of California, San Diego. Chapter 5 provides an overview of our efforts to create a working IBSC device based on the GaNPs system.

Chapter 2

Intermediate band solar cells

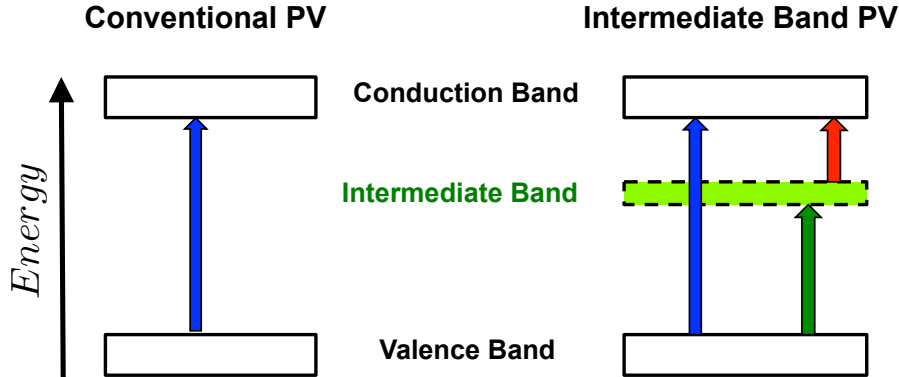


Figure 2.1: In a conventional PV, there is only one primary optical transition. In an intermediate band PV, the primary optical transition is augmented by an additional sequential series of lower-energy photon absorptions that can also promote a carrier across the bandgap.

2.1 Introduction

The intermediate band solar cell (IBSC) concept provides a means to achieve photovoltaic conversion efficiencies exceeding the Shockley-Queissar (SQ) efficiency limit for a single junction solar cell by providing a higher photocurrent while maintaining a high output voltage[14, 15]. In an IBSC, a partially occupied energy band, or “intermediate band” (IB), located within the bandgap region of a semiconductor serves as a ‘stepping stone’ for the absorption of lower energy photons that are otherwise unattainable for photocurrent conversion. Unlike multi-junction cells, the IB solar cell enables photocurrent to be extracted through only a single p-n junction, greatly simplifying the device architecture. Detailed balance calculations show that a single junction cell formed in a material with a proper location of an IB can achieve an theoretical maximum power conversion efficiency of 63%[4].

2.2 Theory

Figure 2.2 shows the band diagram of an intermediate band solar cell, which is a semiconductor with 3 energy bands: the valence band (VB), and conduction band (CB), and the additional intermediate band (IB). With three bands, there are three allowed optical transitions: VB to IB (energy E_{IV}), IB to CB (energy E_{IC}), VB to CB (energy E_{CV}). In 1997, Luque and Martí defined 7 conditions which are necessary to achieve an ideal IBSC, which are used as the basis of calculating the theoretical limiting performance of an ideal IBSC [4], these are summarized in Table 2.1. Thus, from a materials perspective, the ideal IBSC absorber would have negligible non-radiative recombination (IC1), high mobility (IC2), and a strong absorption coefficient (IC4). From a device design per-

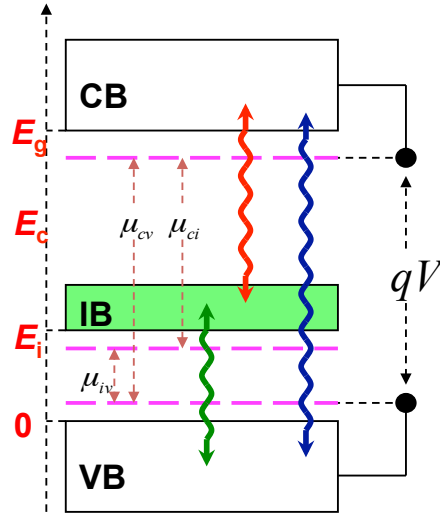


Figure 2.2: IBSC band diagram using the notation defined in ref. [4].

spective, the ideal IBSC device would have an electrically isolated IB with perfect ohmic contacts (IC3), sufficient cell thickness to ensure full absorption (IC4), a high-quality mirror (IC5), and operate under high concentration with an ideal concentrator (IC7), while the absorber maintains an operating temperature, T_a , of 300K. Using these conditions, the limiting efficiency of an ideal IBSC can be determined solely based on the band gaps of the cell. Arithmetically $\epsilon_I + \epsilon_C = \epsilon_G$, where ϵ_I , ϵ_C , and ϵ_G represent the intermediate (smaller) bandgap, the larger bandgap, and the total bandgap, respectively. Thus, the limiting efficiency may be calculated¹ as a function of just the total bandgap ϵ_G and the smaller, or intermediate, bandgap ϵ_I , as shown in Figure 2.3 .

Ideally the intermediate band would be half-filled with carriers that could be promoted to the conduction band. There are two ways to accomplish this: 1) high doping such that the Fermi level is in the middle of the IB, or 2) using high levels of illumination to photo-fill the IB with carriers.

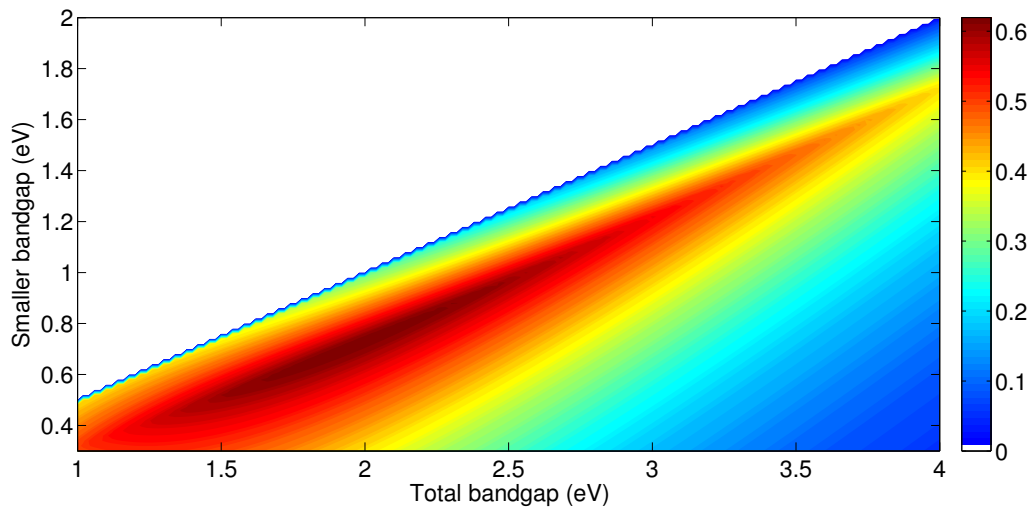
2.2.1 The effect of concentration

A high level of concentration would be required to achieve sufficient photo-filling in the intermediate band. According to the detailed balance theory, the efficiency of a solar cell increases as a function of concentration, X . This is a direct result of an increase in open circuit voltage as shown below.

¹*Mathematica* code based on the method outlined in [4] can be found in Appendix B.

Table 2.1: Conditions necessary for an ideal IBSC, from Ref. [4]

	condition	design implications
IC1	only radiative transitions between bands	keep non-radiative recombination low
IC2	infinite carrier mobility	use high-mobility materials
IC3	no carrier extraction from IB	IB must be electrically isolated
IC4	full absorption of photons at each energy	strong optical absorption coefficient a_0
IC5	photons only escape front of cell	use excellent bottom mirror
IC6	stepwise absorption coefficient at each energy level	materials have high optical absorption coefficients
IC7	isotropic cell illumination	use maximum achievable solar concentration

Figure 2.3: Contour plot of ideal IBSC efficiency limit (shown in the color bar) calculated as a function of both the total bandgap ϵ_G , and smaller bandgap ϵ_I .

2.2.1.1 Low injection

For low injection, if the incident solar flux is increased by a factor X , the short circuit current density will also increase by X , to within a first approximation, and the dark current will remain unchanged². Thus $J_{sc}(X) \approx XJ_{sc}$. The resulting open circuit voltage is

$$qV_{OC}(X) = \mathbf{n}kT \ln \left[\frac{J_{SC}}{J_0} + 1 \right] \approx qV_{OC}(1) + \mathbf{n}kT \ln [X] = nkT \ln \left[\frac{J_{SC}}{J_0} \right] + \mathbf{n}kT \ln [X] \quad (2.1)$$

where $V_{oc}(1)$ is the open circuit voltage under 1 sun illumination, and \mathbf{n} is a diode ideality factor. Equation 2.1 may also be written as

$$qV_{OC}(X) = E_g - kT \ln \left[\frac{I_{SC}}{I_0} \right] + kT \ln \left[\frac{X}{r(\theta)} \right] \quad (2.2)$$

where $r(\theta)$ is the reflectivity for the cone of light with an angle, θ , which impinges the cell from the concentrator[16]. From this we see that $V_{OC}(X)$ increases as the logarithm of X . If the fill factor remains constant, the power output increases by

$$P(X) = P(1) \left[X \left(1 + \frac{\mathbf{n}k_B T}{qV_{OC}(1)} \ln(X) \right) \right] \quad (2.3)$$

with the cell efficiency given by

$$\eta(X) = \eta(1) \left[1 + \frac{1 + \mathbf{n}k_B T}{qV_{OC}(1)} \ln(X) \right]. \quad (2.4)$$

However, both realistically and in the field, the dark current is indeed affected by concentration due to: 1) increased carrier density resulting in high injection; () increased operating temperature of the cell. Both these conditions cause deviations from the result obtained in Equation 2.1.

2.2.2 IBSC efficiency with a realistic solar spectrum

In addition to the idealistic material and device properties used above, the IBSC detailed balance calculation assumes that the sun is a perfect blackbody with temperature $T_s=6000$ K, and thus the incident solar irradiation is described by a blackbody spectrum. Other works have investigated the impact of using a more realistic input spectrum, such as the AM1.5G (under 1 sun) and AM1.5D (under concentrated sunlight), on the IBSC efficiency[6, 17]. The result being that there exist multiple maxima for each concentration level, instead of one global maximum as in the blackbody case. This effect is similar to

²See, for example, section 9.5 of [12] for an excellent treatment on the effect of concentration on solar cell device physics.

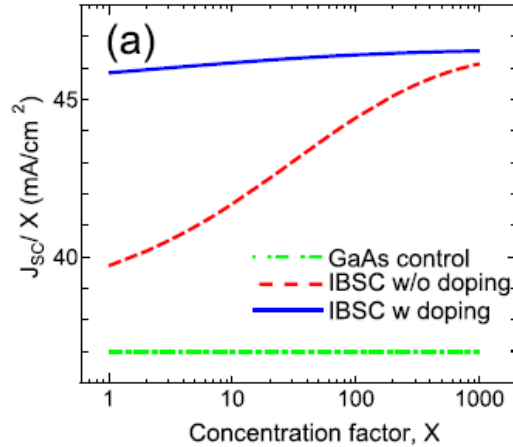


Figure 2.4: Effect of concentration factor X on the short circuit current density of a GaAs-based IBSC. From [5]

the case of tandem solar cells under the AM1.5 spectrum[18]. Furthermore, the energy gap combinations corresponding to each maximum were found to shift by several tens of meVs over a concentration range of $X = 1-10,000$ suns. This has the design implication that a practical IBSC should have the desired concentration ratio taken into account when choosing the absorber bandgap. The effect of concentration ratio on IBSC operation is further explored in Chapter 5.

2.3 Key technical challenges

2.3.1 Identification of semiconductor material systems that result in intermediate bands

Any intermediate band absorber requires a deep level trap species that, in sufficient quantity, can delocalize to form a band. A few different systems have been studied for their potential as intermediate band materials. These include epitaxial quantum dots in quantum wells, highly mismatched III-V and II-VI alloys, and more recently, kesterites[19]. One approach, which has led to previous practical realization of IBSC is through the engineering of both II-VI and III-V highly-mismatched alloys. These materials display radical restructuring of the energy bands by changing the alloy composition and can be used to form intermediate band semiconductors. Two main challenges encountered have been 1) having a long enough carrier lifetime in the intermediate band and 2) having strong optical absorption in the intermediate band. We have recently begun experimentally measuring a new semiconductor material, multi-band GaNPs, which has been demonstrated to have

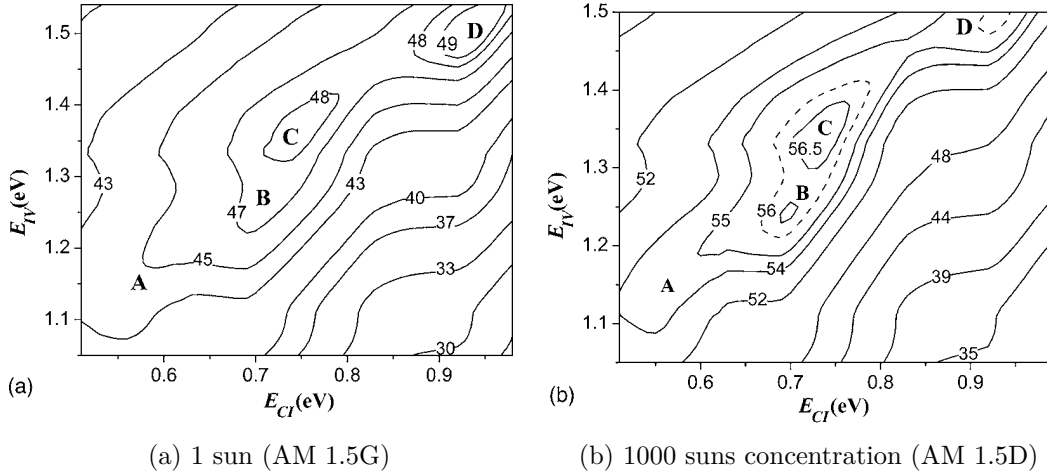


Figure 2.5: Efficiency contour plots for ideal IBSC under AM 1.5 irradiation. From [6].

strong optical absorption due to a direct bandgap and a potentially long carrier lifetime since the indirect band is very close in energy and there is transport between the bands. Furthermore, this alloy offers 2 degrees of freedom to engineer the bandgap so that it could be ideally matched to the solar spectrum[20].

It should be noted that this bulk approach to forming intermediate bands has alternatives, namely the use of energy levels of the confined states in a quantum dot[21], but their nanoscopic, epitaxial fabrication may make them impractical to manufacture at scale. In these systems, quantum confinement or nanoscale layering of different materials results in regions of the material with different band edge energy levels than their surroundings. In this way, the small bandgap regions can create a band within the large bandgap material. The energy levels using confined states in QD's led to a demonstration solar cell in 2004, however solar cells based on QD's typically have low absorption in the IB since the density of QD's in the material is not high enough. Furthermore, there is a problem of tunneling between QD's, which significantly reduces the open-circuit voltage, and hence the efficiency of the device. Despite this, there are reports of cells with efficiencies over 18%[22].

2.3.2 Selecting high-quality absorber materials

Intermediate band absorbers are attractive because of their simplicity compared to multi-junction devices. In a multi-junction device, the different sub-cells, often made of different materials, must be epitaxially matched. The same functionality can be achieved in a single material using an intermediate band absorber[23].

The principle challenge is that incorporating the extraordinary dopant densities required to form the delocalized band often leads to crystallographic phase segregation of the dopants. In this case the alloy is not truly uniform but rather a mixture of two or more

crystallographic phases. As a result, the unique band structure is lost. Non-equilibrium semiconductor growth techniques, such as molecular beam epitaxy and pulsed laser deposition, can be used to incorporate above-equilibrium concentrations of dopants. The idea of putting levels in the middle of the bandgap to increase the photocurrent was first proposed in 1960 and termed a “multi-transition cell”[24]. This idea was rejected initially because it was believed that these levels would act as trap centers for non-radiative recombination and kill the device efficiency. Any material candidate for IBSC application must take steps to inhibit non-radiative recombination, as is the case when density of impurities is high enough to exceed the Mott transition, where the behavior of the impurities effectively transitions from a trap-like state to that of a band[15, 25]. This is done by increasing the density of impurities beyond the density given by the Mott transitions. As a result, an electronic band forms and the electron wave function is delocalized, preventing detrimental Shockley-Reed Hall (SRH) recombination[26].

In addition, the doped material must be isolated from the conducting electron and hole contacts. One of the key requirements of the intermediate band is that the intermediate band is electrically isolated, acting as a “stepping stone” for sub-bandgap photons, which also make it analogous to a 2-terminal triple junction cell. If the intermediate band penetrates to the contact, carriers can be swept out of the intermediate band and the voltage of the device will be characteristic of one where the bandgap is only as large as the optical transition from the valence band to the intermediate band. In practice during thin-film deposition, this has been achieved through electron and hole selective contacts or the use of a wide-gap lattice-matched semiconductor such as AlGaAs as an electron-blocking layer in the case of IBSC based on GaAsN[27, 28] and is further explored in Chapter 5.

2.4 Experimental efforts

2.4.1 Quantum dots

Many experimental efforts to realize IBSC’s have focused on using mini-bands formed by confined states of a quantum dot array[21, 15]. In these systems, quantum confinement or nanoscale layering of different materials results in regions of the material with different band edge energy levels than their surroundings. In this way, the small bandgap regions can create a band within the large bandgap material. However, these quantum dot (QD) IBSC’s have limited success due to low absorption in the IB since the density of QD’s in the material is not high enough. Furthermore, there is the problem of tunneling between QD’s, which significantly reduces the open-circuit voltage, and hence the efficiency of the device[29]. A further review of IBSC experimental results can be found in Ref. [30].

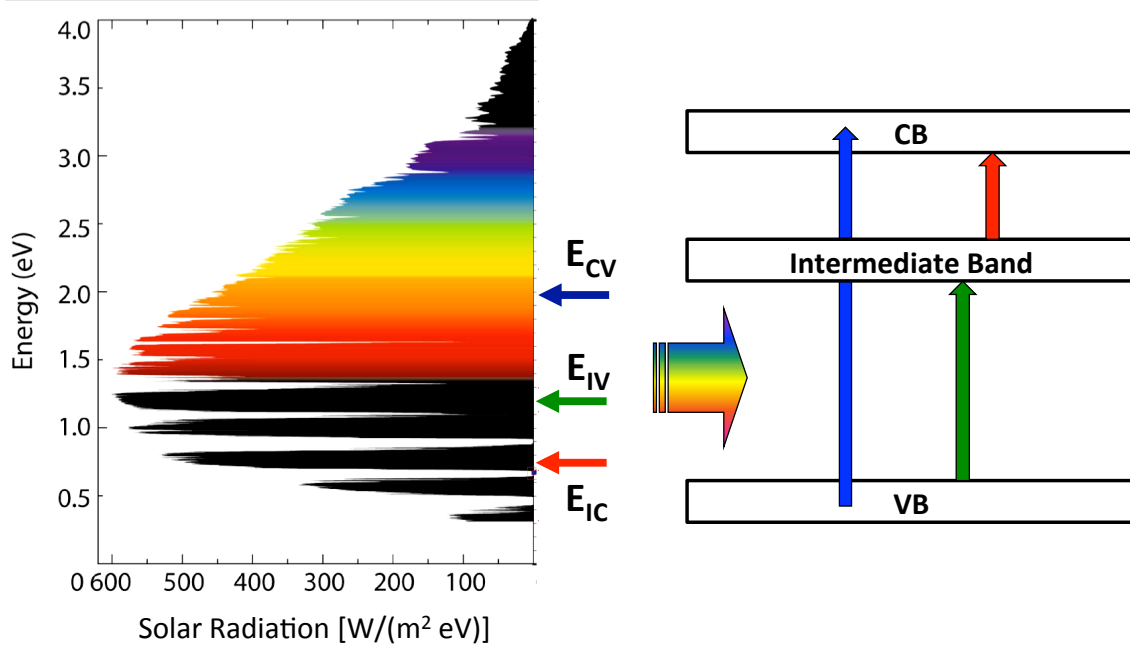


Figure 2.6: Representative energy band diagram of an IBSC shown alongside the solar spectrum.

Table 2.2: Summary of approaches towards realization of IBSCs

approach	material system	ref.
Quantum dots	InGaAs/GaAs	[31]
	InAs/GaNAs	[32]
Transition metal impurity	Ga ₄ P ₃ M and Ga _x P _y M alloys	[33]
	TiGa ₃ As ₄	[34]
	CuGaS ₂ :M (M=Fe,Co,Ni)	[35][36]
HMA's	SnS ₂ :V	[37]
	GaNAs	[28]
	GaNAs	[38]
	ZnOTe	[39, 40, 41]

	III	IV	V	VI
Atomic number	5	6	7	8
	B	C	N	O
Electronegativity	2.05	2.52	3.01	3.47
Atomic Radius (Å)	0.87	0.70	0.65	0.60
	13	14	15	16
	Al	Si	P	S
	1.61	1.82	2.19	2.58
	1.18	1.10	1.00	1.00
	31	32	33	34
	Ga	Ge	As	Se
	1.76	1.77	2.04	2.35
	1.36	1.25	1.15	1.15
	49	50	51	52
	In	Sn	Sb	Te
	1.66	1.61	1.82	2.08
	1.56	1.45	1.45	1.40

Figure 2.7: Columns III-VI of the periodic table relevant to the semiconductors in this work. Shown are the Pauling scale of electronegativity and the atomic radius.

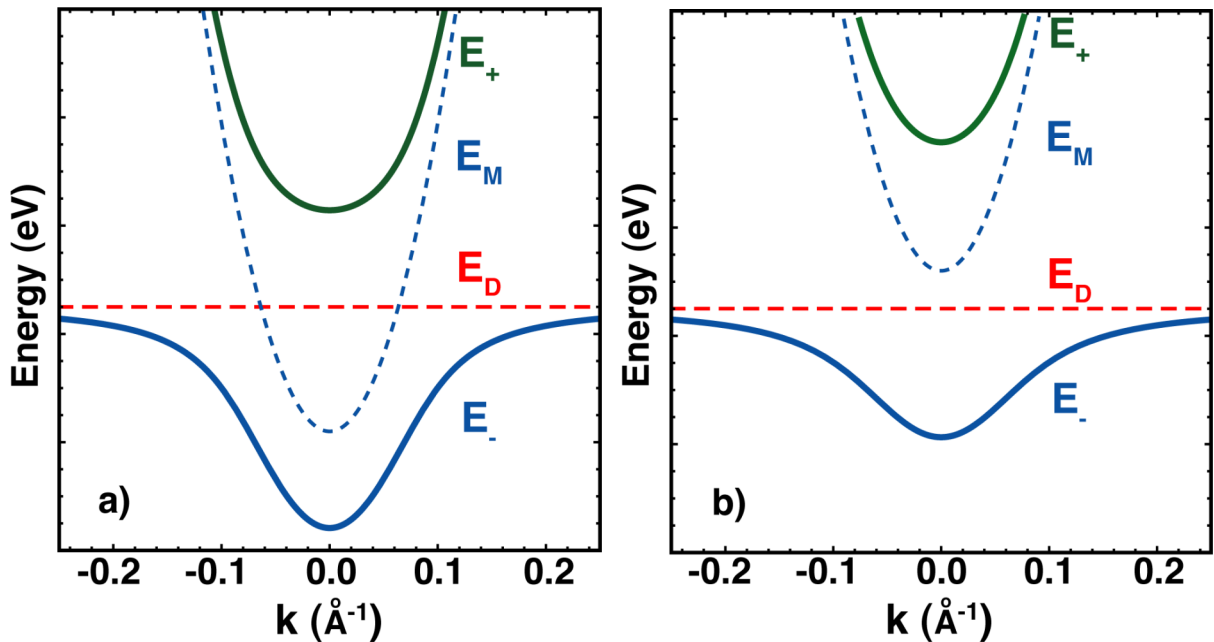


Figure 2.8: Band structure calculation using the band anticrossing model for the nitrogen defect level in (a) the conduction band, such as GaAsN; and (b) below the conduction band, such as GaNPAs. Figure courtesy of R. Broesler.

2.4.2 Highly-mismatched alloys

Another approach using bulk materials is to use highly-mismatched semiconductor alloys (HMA's), such as dilute nitrides[42, 43, 44] and oxides[45], which naturally exhibit an intermediate band. The formation of this intermediate band in HMA's is explained by the band-anticrossing model (BAC)[46] explored further in Chapter 4. The BAC model describes the interaction between the localized isoelectronic impurity level (N in III-V case), and the conduction band of the host semiconductor matrix. This interaction splits the conduction band into two sub-bands, E_- and E_+ . The downward shift of the lower sub-band (E_-) is responsible for the reduction of the fundamental band gap and the optical transition from the valence band to the upper sub-band (E_+) accounts for the high-energy edge. Figure 2.6 depicts a representative IBSC system showing the 3 allowed optical transitions. IBSC proof-of-concept devices have been demonstrated in the II-VI alloy ZnOTe[47]. In 2011, an IBSC device based on the Group III-V highly-mismatched semiconductor GaNAs alloy was shown to have optical activity from the three energy bands. It proved to be a working PV cell where the IB contributed to a measurable increase in photocurrent [28].

Figure 2.9 shows the calculated efficiency of an IBSC based on the $\text{GaAs}_{1-x}\text{N}_x$ system with energy gap values determined by the BAC model (Equation 4.7). Practically, it is very difficult to achieve x greater than 4% without significant degradation of material quality [48]. A key requirement for an efficient intermediate band solar cell is that the intermediate band should be narrow and well separated from the valence band and conduction band[15, 4]. In GaAsN the IB is wider because it is formed by splitting the conduction band into the E_- and E_+ sub-bands and because the nitrogen level is located above the conduction band edge [49, 50].

Calculations based on the band anticrossing model show that the localized nitrogen level lies below the conduction band edge for $\text{GaN}_x\text{P}_{1-x-y}\text{As}_y$ alloys with $y < 0.7$, suggesting that the intermediate band formed will be narrow and hence more suitable as an intermediate band for IBSC's compared with the GaAsN alloy system. Additionally, changing the As/P ratio (y) of the quaternary alloy allows for the modification of the location of the IB (E_-) and the conduction band (E_+) for optimum absorption of the solar spectrum. Furthermore, $\text{GaAs}_y\text{P}_{1-y}$ exhibits a direct-indirect gap crossover at approximately $y=0.5$, and for alloys with compositions $y>0.5$ the photon absorption occurs at the lower energy Γ point through direct-gap absorption, yet electrons could also occupy the X -valley through inter-valley scattering[51, 52]. This could result in an IBSC absorber material with both high absorption coefficient and longer carrier lifetimes[53]. The band structure of the GaNPAs alloy system and its implications for IBSC's is covered in Chapter 4.

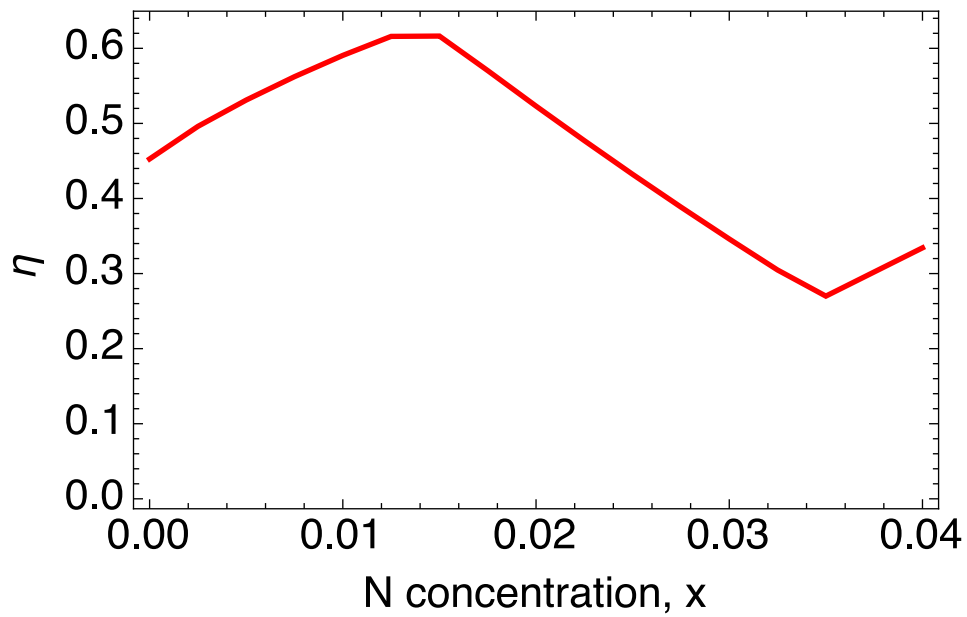


Figure 2.9: Calculated efficiency of ideal GaAs_{1-x}N_x IBSC as a function of N concentration, x .

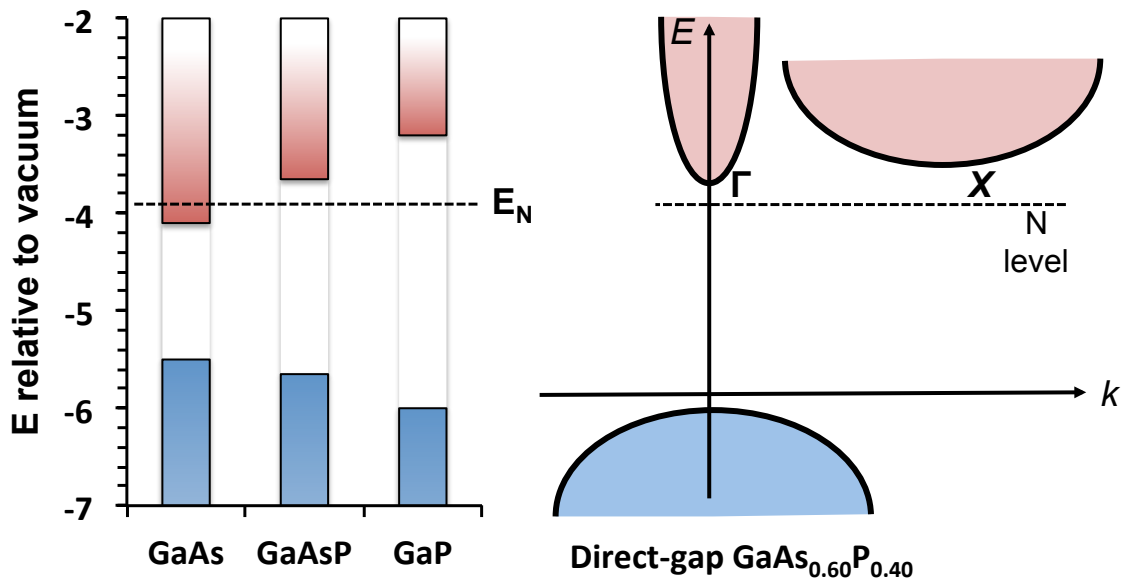


Figure 2.10: Band offsets relative to vacuum of the GaAs_{1-y}P_y alloy system for $y = 40\%$ (left), and schematic band structure showing the nitrogen level and the Γ and X CB minima.

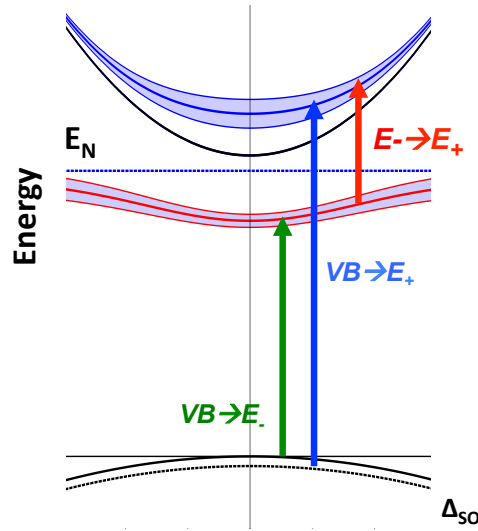


Figure 2.11: Calculated $E[k]$ diagram for dilute-nitride GaAsPN with $\sim 2\%$ nitrogen. The interaction with localized N states splits the original host GaAsP conduction band into lower (E_-) and upper (E_+) conduction sub-bands, which become the IB and CB, respectively, in the intermediate band solar cell device scheme. The 3 allowed optical transitions are also shown.

2.5 Summary of requirements for viable intermediate band solar cells

The material requirements for intermediate band solar cells can be summarized as follows:

- The position of the IB has to be controllable
 - Necessary to optimize the absorption of the solar spectrum
- The IB must have a sufficiently high DOS
 - Non-radiative recombination has to be inhibited
- The IB must be partially filled
 - Has electrons to be promoted to the CB and empty states to receive electrons from the VB
- The IB has to be isolated from the CB
 - High energy electrons will not be thermalized to the IB

- The IB must be electrically isolated from the contacts
 - V_{OC} is determined by the largest gap

2.6 Summary

The dissertation focuses on two dilute nitride alloy systems for IBSC applications: GaAsN and GaNPAs. Though GaAsN has already proven itself as a potentially viable IB absorber material [28], nanowires based on GaAsN would offer the additional benefit of high light absorption and the ability to use a range of low-cost substrates, including silicon. Chapter 3 details the growth and characterization of GaAsN nanowires.

The quaternary GaNPAs alloy system is another candidate material for IBSC's that may overcome some of the shortcomings of the GaAsN system[20]. GaNPAs has the potential to be better suited to PV conversion of the solar spectrum, and has the advantage that, as a quaternary alloy, it offers another degree of electronic structure tunability by varying the As:P ratio in addition to the amount of nitrogen in the alloy. A detailed exploration of the electronic structure of GaNPAs is found in Chapter 4, and the results of GaNPAs IBSC device characterization are found in Chapter 5.

Chapter 3

Dilute nitride nanowires

3.1 Background

3.1.1 Nanowires for PV

Of particular interest, latently, to the PV research community, are PV designs based on, or incorporating, nanostructured materials. They offer the potential to exploit quantum confinement or surface-area to volume effects to enhance PV device efficiency, which may be impracticable or impossible to achieve using bulk materials engineering. Examples include nanocrystals (0-dimensional confinement), nanotubes, nanorods, nanopillars, nanowires (all of which are 1-dimensional confinement), and quantum wells (2-dimensional confinement). These nanostructures can provide advantages both through strong light absorption (high optical absorption coefficient), and efficiency in charge-carrier separation as a result of large surface area to volume [54]. Nanowires have the potential to be exploited for many applications due to their small size and high surface area to volume ratio. These applications range from use as biological[55, 56] and chemical sensors[57], to solid-state batteries, to applications in optoelectronics including the next generation of lasers, solar cells[58, 59, 60], and LED's[61].

The PV community, in particular, is interested in nanowires for PV since they offer the promise of coupling a 1-dimensional direct path for charge transport[62], and a high surface area for light harvesting. Nanowire arrays typically have strong antireflection properties, and exhibit excellent light-trapping effects, all while using less actual material than the comparative bulk design[63]. Furthermore, due to their unique one-dimensionality, nanowires are able to solve certain problems that in the thin-film semiconductor community such as integration of III-V's and other semiconductors directly onto silicon[64]. Nanowires provide a mechanism to relax lattice strain during growth and thus pave the way for optoelectronic semiconductor growth on lattice-mismatched substrates, such as III-V's on silicon and germanium[65, 66]. Additionally, the ability to selectively grow heterostructures and superlattices allows for bandgap engineering and potential to further control optical and electronic behavior of nanowires[67].

Figure 3.1 shows the calculated efficiency limit of an idealized IBSC based on $\text{GaAs}_{1-x}\text{N}_x$ nanowires using the detailed balance theory developed in Chapter 2. There are two maxima, at $x=1.3\%$ and $x=6.5\%$. Due to the relatively large lattice mismatch ($\sim 21\%$) between GaAs and GaAsN, it is difficult to incorporate large amounts of nitrogen in GaAsN. From the standpoint of thin-film growth, the practical nitrogen concentration is in the range between 0% and 4%, where there is both a significant change in the electronic structure due to band anticrossing and the material quality of the film remains high[48]. Thus, for IBSC applications, a nitrogen concentration of approximately $x=1.3\%$ was chosen as the target composition for $\text{GaAs}_{1-x}\text{N}_x$ nanowires.

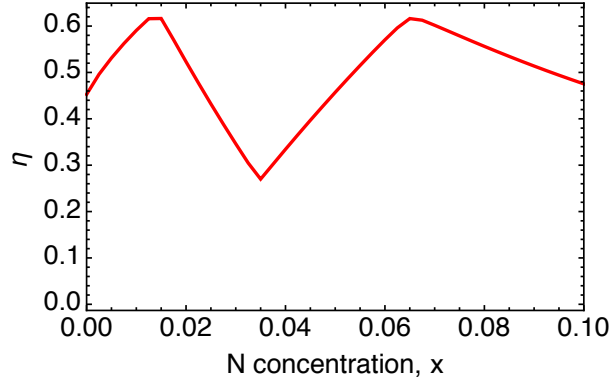


Figure 3.1: Calculated efficiency (η) as a function of nitrogen concentration for an ideal IBSC based on GaAsN nanowires.

3.1.2 Growth

The nanowire growth may be explained in terms of the vapour-liquid-solid (VLS) growth mechanism[68][69]. In VLS growth, the minimum radius of the liquid droplet used for wire nucleation is given as

$$R_{min} = \frac{2V_L}{RT \ln(s)} \sigma_{VL} \quad (3.1)$$

where V_L is the volume of the droplet, σ_{VL} is the vapour-liquid surface free energy, R the molar gas constant, T the temperature, and s the degree of supersaturation in the vapour phase. From this equation it is apparent that a higher substrate temperature will yield a smaller diameter droplet, and hence a nanowire with smaller diameter.

Previously, GaAs nanowires have been grown with molecular beam epitaxy (MBE) without the use of a catalyst seed particle¹, using gallium to catalyze the wire growth[70]. These catalyst-free GaAs nanowires can be grown on a number of substrates, including silicon (111)[71]. Varying the growth conditions allows for control over the physical dimensions of the wires and properties including chemical composition. including the formation of core-shell nanowires[72]. However, there exist few studies on the growth and resulting properties of HMA nanowires. Other works have shown that controlled changes in the alloy composition of the II-VI alloy nanowires $ZnSe_{1-x}Te_x$ can be achieved by varying the growth temperature. The resulting change in electronic structure, namely, an extreme bandgap bowing, is described within the framework of the band anticrossing model[73].

For III-V dilute nitride nanowires, there has been recent work focused on both the GaP/GaPN[74] system and the GaAs/GaAsN system. In the GaP/GaPN system, the authors were able to achieve a nitrogen concentration of up to 0.9% as determined by photoluminescence (PL) spectroscopy[75]. In the case of $GaAs_{1-x}N_x/GaAs$, nanowire

¹Typically gold, nickel, or other metals may be used.

heterostructures with a nitrogen concentration of 0.3% have been achieved using the self-catalyzed technique[76]. Though this work was significant in that it demonstrated the feasibility of growing $GaAs_{(1-x)}N_x$ nanowires, the nitrogen concentration was low, and thus the resulting change in the bandgap energy as measured by PL was relatively small. Though 0.3% of nitrogen is close to the solubility limit in GaAs[77], one of the chief advantages of using a non-equilibrium growth technique such as molecular beam epitaxy is that it enables higher concentrations far exceeding the solid solubility limit. This chapter describes a novel approach for the catalyst-free growth of GaAs nanowires and GaAs/GaAsN core-shell nanowire structures and their resulting structural, electronic, and optical properties .

3.2 Molecular Beam Epitaxy Growth of III-V and highly-mismatched alloy nanowires

The GaAs and GaAsN nanowires were grown by the catalyst-free MBE VLS method[71]. Growth was performed with an Intervac Gen II MBE with solid source Ga and As effusion cells, ion- and cryo- pumps, as well as a reflection high-energy electron diffraction (RHEED) system. A DC constricted-plasma source (CPS)[78] was used as the source of nitrogen, which has been shown to provide high nitrogen incorporation efficiency, growth stability, and reproducibility in GaAsN epitaxial layers [79, 80]. The Nitrogen flow rate during growth was monitored via a Tylan (Millipore) FC-2950M mass flow controller. A Glassman ER series DC voltage source (100mA, 3kV) was used for precise control and regulation of the nitrogen plasma.

With the constricted-plasma source, the plasma is initiated in the gas (diatomic nitrogen in this case) flowing through the source and into the chamber. Though the degree of ionization is low, defined as the ratio of charged monatomic nitrogen species compared to the concentration of neutral diatomic nitrogen species, a considerable amount of excited atoms may still be involved in the growth. The two important parameters which define the plasma are the nitrogen flow rate F into the course and the DC current I passing through the discharge chamber. For a given flow rate, there is a minimum current, I_{min} , required to maintain a stable plasma. Figure 3.3b shows the I_{min} vs F curve for the DC plasma source used[81]. Below a certain flow rate, the plasma is classified as *unstable* and will typically be extinguished after several minutes. This is due to the flow rate dropping low enough to quench the plasma as a result of fluctuations in the nitrogen supply, which may periodically cause a lower than normal flow rate.

Though the flow rate is a crucial parameter in determining the stability of the plasma, previous experiments on the growth of GaAsN layers determined that F only marginally affects the nitrogen incorporation efficiency, η_{in} , in the epilayers. η_{in} is the product of the nitrogen activation efficiency of the plasma source, η_{ac} , and the growth condition dependent sticking coefficient of the active nitrogen species, η_{st} [79]. However, η_{in} was found to depend linearly on the on the plasma discharge current. As shown in Figure

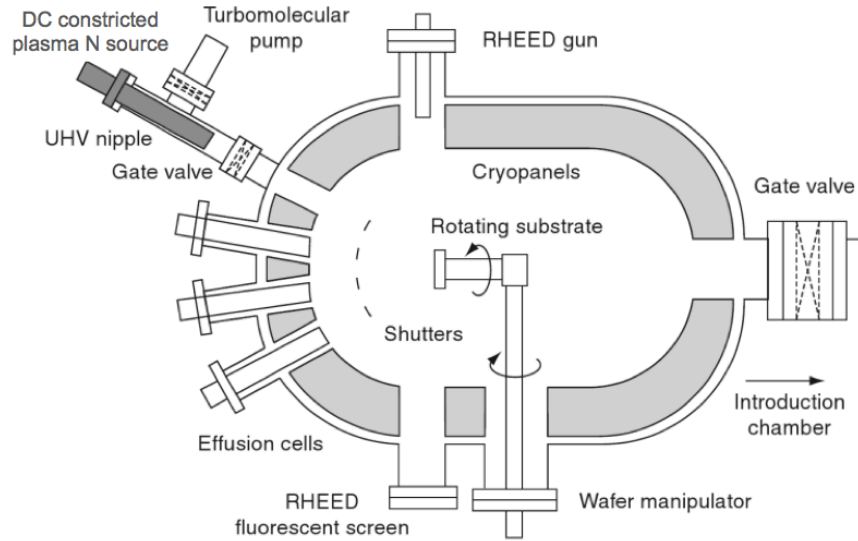


Figure 3.2: Schematic of MBE growth fitted with DC constricted plasma source for N. Adapted from [7].

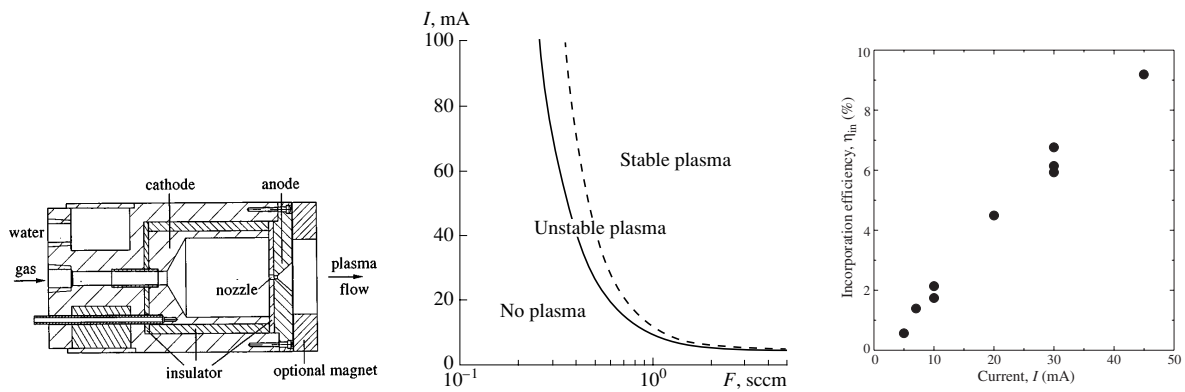


Figure 3.3: The DC constricted plasma source.

3.3c, a maximum η_{in} of nearly 10% was reached at a discharge current of 45 mA. The reason that the incorporation efficiency depends mainly on discharge current is due to the fact the current is directly proportional to the flux density of the ions which generate actively charged nitrogen species during the collision process[79].

All growths were performed on Si (111) substrates with no special surface cleaning or treatment before growth. Other groups report the use of organic chemical solvents to clean the Si (111) surface before transferring to the MBE growth chamber[71], but in our case it was not found to be necessary. Furthermore, the native oxide layer was left intact during all growth runs.

3.2.1 Growth of GaAs nanowires

Growth of GaAs nanowires was performed both without and with a gallium pre-deposition step, hereafter referred to as Type A and Type B GaAs nanowires, respectively. The purpose of the pre-deposition step was to deposit a gallium droplet on the silicon substrate that would act as seed catalyst particle for the VLS nanowire growth. For the wires grown without gallium pre-deposition, the silicon substrate was brought up to 560 °C and then exposed to constant arsenic flux for 5 minutes at a beam equivalent pressure (BEP) of 1.3×10^{-5} Torr. Then, the gallium flux was turned on at a 15:1 As/Ga BEP ratio for 10 minutes to grow the wires. The gallium source was then turned off and the substrate was immediately cooled. After the temperature dropped below 500 °C, the As source was turned off and the wires continued to cool to room temperature. For the wires grown with Ga pre-deposition, the substrate was initially heated to 560 °C and then exposed to Ga flux for 5 seconds, allowing for the formation of Ga droplets on the surface. The As flux was then turned on and GaAs wires were grown in As-rich conditions for 10 minutes at the equivalent 15:1 As/Ga BEP ratio at a flux that would correspond to 1 μ m/hour growth rate for thin-film GaAs, or 1 monolayer/second. A constant substrate rotation of 7 r.p.m. was used during all growths. The table summarizes the growth conditions of both thin-film GaAs, GaAsN, and GaAs NW's.

3.2.2 Growth of GaAsN nanowires

In order to grow GaAsN nanowires, two distinct growth methodologies were used: a core-shell, or radial growth method; and an axial growth method. Each will be discussed in-turn.

3.2.2.1 Core-shell GaAs/GaAsN nanowires

For the core-shell nanowires, the initial procedure was the same as for the growth of GaAs nanowires, as the GaAs wires act as a template or “core” for the growth of the GaAsN shell. First, the initial GaAs nanowire core was grown for 10 minutes, following the recipe above. Next, there was a subsequent 10 minute growth interruption during which

Table 3.1: Published growth conditions for III-V nanowires

Compound	Group III Source	Group V Source	Substrate	Temp	catalyst	ref.
GaAs	Ga	As ₄	GaAs (111)B	585°C	Au	[82]
GaAs	Ga	As	Si(100), Si(111)	530-580°C	Au	[83]
GaAs	Ga 1.4- 4.1x10 ⁻⁷ Torr	As 1.2x10 ⁻⁵ Torr	Si (111)	580°C	Ga (self)	[71]
GaAs	Ga 3.5x10 ⁻⁷ Torr	As 2.0-3.4x10 ⁻⁵ Torr	Si (111)	580°C	Ga (self)	[71]
GaP/GaNP	Ga	PH ₃	Si(111)	580°C	Ga (self)	[75]
GaAs/GaAsN	Ga 3.3x10 ⁻⁷ Torr	As 1.4x10 ⁻⁷ Torr	Si(111)	560-580°C	Ga (self)	this work

the gallium shutter was closed, the nitrogen plasma source was started and stabilized. In the MBE growth of nanowire heterostructures, a growth interruption is used in order to change source materials. For GaAs, this is typically done under a constant arsenic pressure while the gallium source is shuttered. Other studies[71] have shown that a growth interruption will result in a termination of the VLS growth process because the gallium droplet at the tip would evaporate. Also during the growth interruption the temperature was lowered to the desired GaAsN growth temperature of between 450 °C and 565 °C. The nitrogen flow rate used was between 1-2 SCCM, and a plasma current was chosen between 10 and 40 mA depending on the desired amount of nitrogen. After the growth interruption, the sample underwent 1 minute of nitridation under constant As flux, then the gallium shutter was re-opened for 30 minutes while the GaAsN “shell” layer was grown. Finally, the gallium shutter was closed and the nitrogen source was turned off. The sample was left under As flux exposure while the sample was cooled to below 300 °C to prevent GaAs decomposition.

3.2.2.2 Axial GaAs/GaAsN nanowires

For the axial nanowires, GaAs nanowires were first grown for 5 minutes at a substrate temperature of 565 °C under constant N₂ gas flux. This then allowed the nitrogen plasma to be started immediately without a growth interruption, and with continued exposure to As and Ga flux, continuing the VLS growth process. Growth continued with the plasma on, at a voltage of 1.0mA and flow rate of 2 SCCM for 5 minutes. Next, the plasma was switched off, but the growth continued for another 5-15 minutes again under constant N₂ gas flux. Finally, the gallium source was closed and the sample was cooled to room

Table 3.2: Nanowire growth conditions

	thin-film GaAs	GaAs NW	GaAsN
growth rate	1 $\mu\text{m/hr}$	1 $\mu\text{m/hr}$	1 $\mu\text{m/hr}$
As/Ga BEP	20:1	15:1	20:1
Substrate	GaAs	Si(111), SiO_2 coated GaAs	GaAs
Growth temp. ($^\circ\text{C}$)	580	580-600 on Si, 580-630 on GaAs	400-500

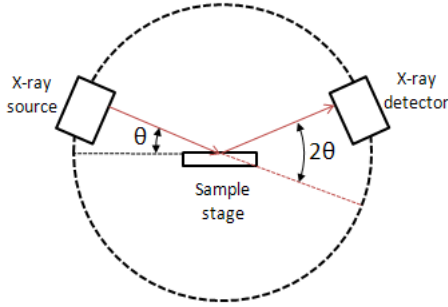


Figure 3.4: Diagram of X-ray diffractometer in the 2θ - ω measurement geometry. From ref. [84].

temperature. The As source was shuttered at $T = 350$ $^\circ\text{C}$.

3.3 Structural Characterization

3.3.1 X-ray diffraction

The size, shape, and areal density of the samples were characterized with scanning electron microscopy (SEM) with energy dispersive x-ray analysis (EDAX). The composition and crystallinity were investigated with hi-resolution X-ray diffraction (XRD), using a Phillips X'pert Pro X-ray diffractometer in the 2θ - ω scan geometry. In this type of symmetric measurement, the source is fixed, the sample is rotated by an angle θ , and the detector rotates by 2θ .

Figure 3.5 shows a symmetric 2θ - ω XRD scan of the GaAs NW, and the $\text{GaAs}_{(1-x)}\text{N}_x$ NW samples. Both samples exhibit the GaAs zinc-blende (111) GaAs peak, confirming crystallinity of the sample, in addition to peaks from the Si (111) growth substrate. In the GaAsN sample, the GaAs (111) peak is shifted to a larger diffraction angle 2θ , consistent with a reduction in crystalline lattice size. Using Vegard's law

$$a_{\text{GaAsN}} = (1 - x)a_{\text{GaAs}} + xa_{\text{GaN}} \quad (3.2)$$

where a_{GaAs} is the lattice parameter of GaAs, and a_{GaN} is the lattice parameter of cubic

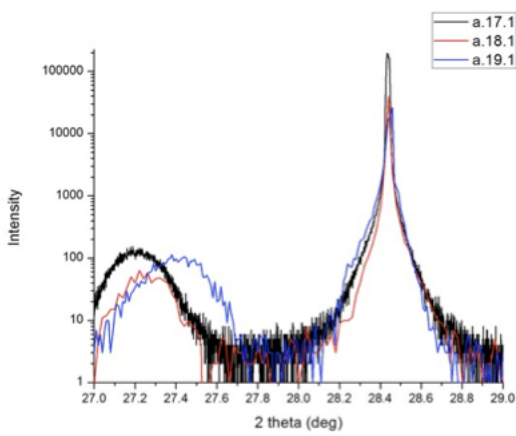
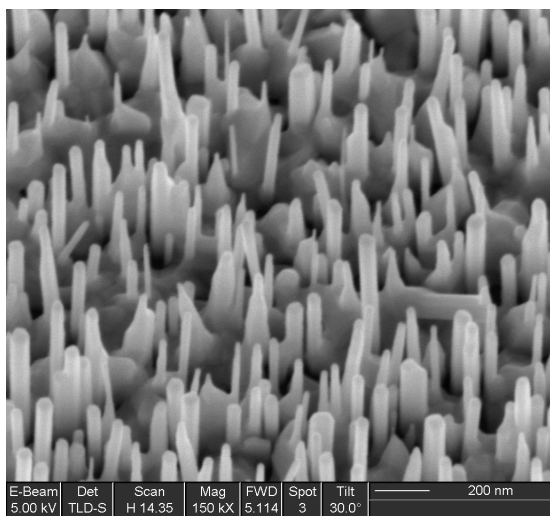


Figure 3.5: XRD symmetric 2θ - ω scan of GaAs (A.17) and GaAsN(A.19). Shown are the Si(111) peak from the substrate at 28.5 degrees, and zinc-blende GaAs peak, which shifts from 27.2 degrees to 27.4 degrees with increasing nitrogen concentration.

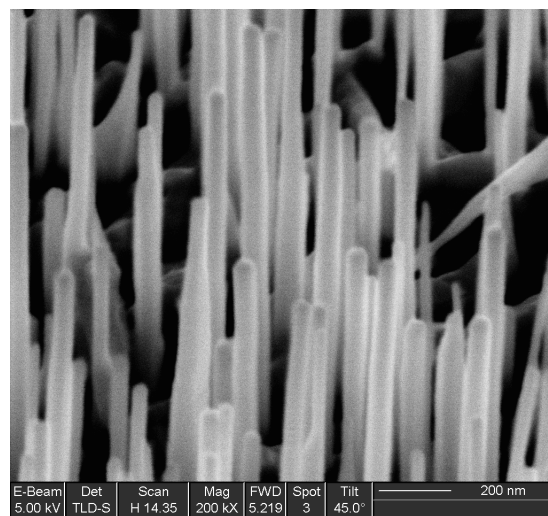
zinc-blende GaN. There is a 0.76 percent reduction in lattice parameter of the GaAsN NW sample due to N incorporation. However, using Vegard's law to estimate the nitrogen composition of GaAsN epilayers results in an overestimation of nitrogen content by up to 30% for $x < 2.5\%$ due to formation of nitrogen-related defects in $GaAs_{1-x}N_x$, which would consequently lead to errors when describing the electronic structure changes in the $GaAs_{1-x}N_x$, namely bandgap reduction with increasing nitrogen incorporation[85]. Thus, we can use the method of Li et al. to set an upper bound of $x = 1.4\% (\pm 0.1)$ in the $GaAs_{(1-x)}N_x$ samples[85].

3.3.2 GaAs Nanowires

Figure 3.6 (a) shows an SEM image of Type A GaAs NW's grown on Si (111) substrate without the Ga pre-deposition step and Figure 3.6 (b) shows the Type B NW's grown with the Ga pre-deposition. In both cases, the NW's are vertically oriented and of uniform areal density. Though the growth time and temperature were the same in both cases, the Type B nanowires were approximately 2-3 longer and diameter appeared to be more uniform among the wires surveyed. As discussed previously, the diameter of the wire is determined by the size of the gallium droplet, which is a function of As or Ga flux during growth, and has been studied in detail in other work[71]. Clearly, using the gallium pre-deposition step (Type B wires) produced better results, and this method was used in all subsequent growths of GaAs/GaAsN wires. Figure 3.7 (b) shows a representative energy-dispersive X-ray analysis (EDAX) scan from a GaAs nanowire. Using EDAX, it was determined that the tip of the nanowire is predominantly gallium, and the Ga:As fraction does not vary significantly along the length of the nanowire.

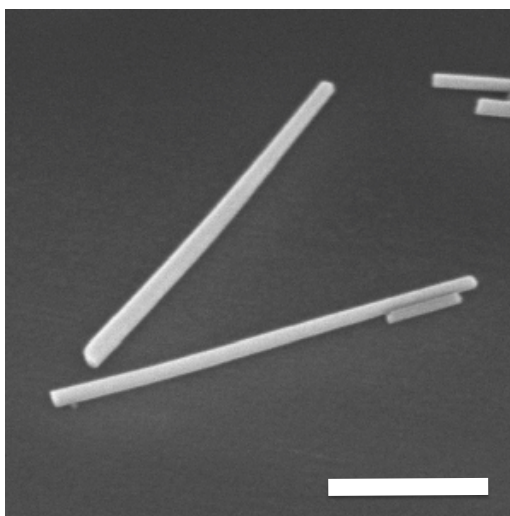


(a) Type A GaAs NW's grown on Si (111) substrate without Ga pre-deposition step.

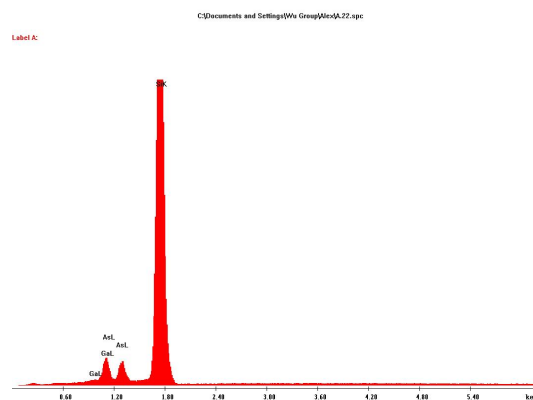


(b) Type B GaAs NW's grown on Si (111) substrate with Ga pre-deposition.

Figure 3.6: SEM images of GaAs NW's.



(a)



(b)

Figure 3.7: (a) SEM image of Type B GaAs nanowire transferred to silicon wafer. The wires shown are approximately 1-1.2 μm in length. Scale bar: 500nm. (b) EDAX spectra of GaAs nanowire body. The large silicon peak is due to the Si substrate.

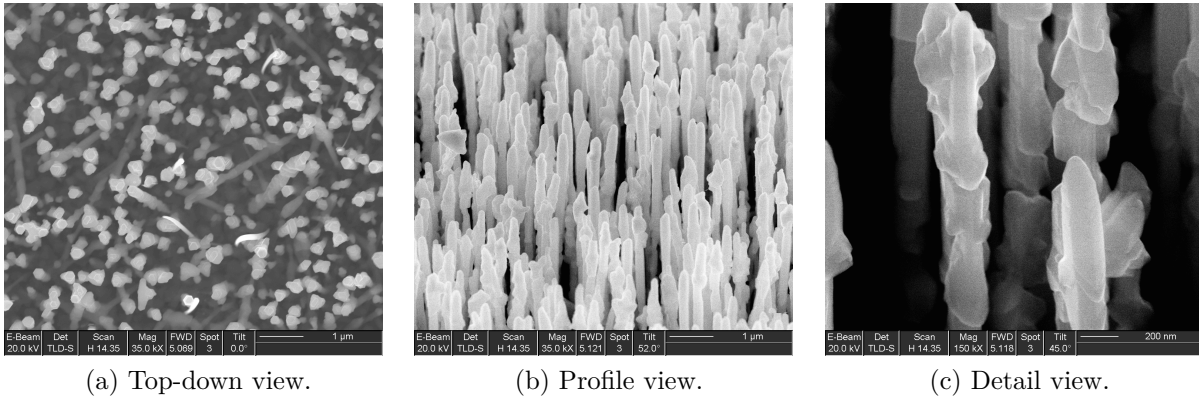


Figure 3.8: GaAs/GaAsN core-shell nanowires grown with plasma current $I = 10\text{mA}$ and flow rate $F = 1.5\text{ SCCM}$.

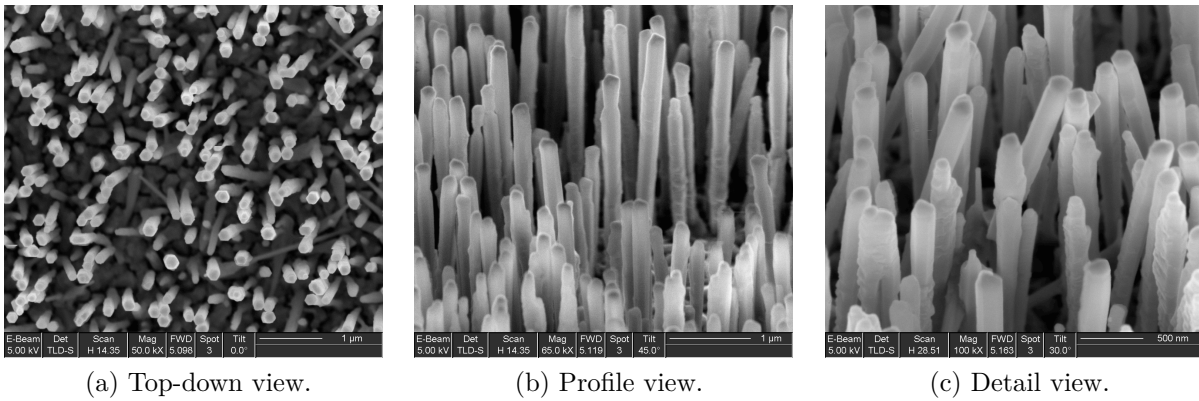


Figure 3.9: GaAs/GaAsN core-shell nanowires grown with plasma current $I = 40\text{mA}$ and flow rate $F = 1.0\text{ SCCM}$.

3.3.3 GaAs/GaAsN nanowires

3.3.3.1 Core-shell GaAs/GaAsN nanowires

Two sets of representative GaAs/GaAsN core-shell NW structure are shown in Figures 3.8 and 3.9.

3.4 Optical Characterization

Optical properties of nanowires were investigated using low-temperature micro-photoluminescence (micro-PL) and photoreflectance (PR) spectroscopy.

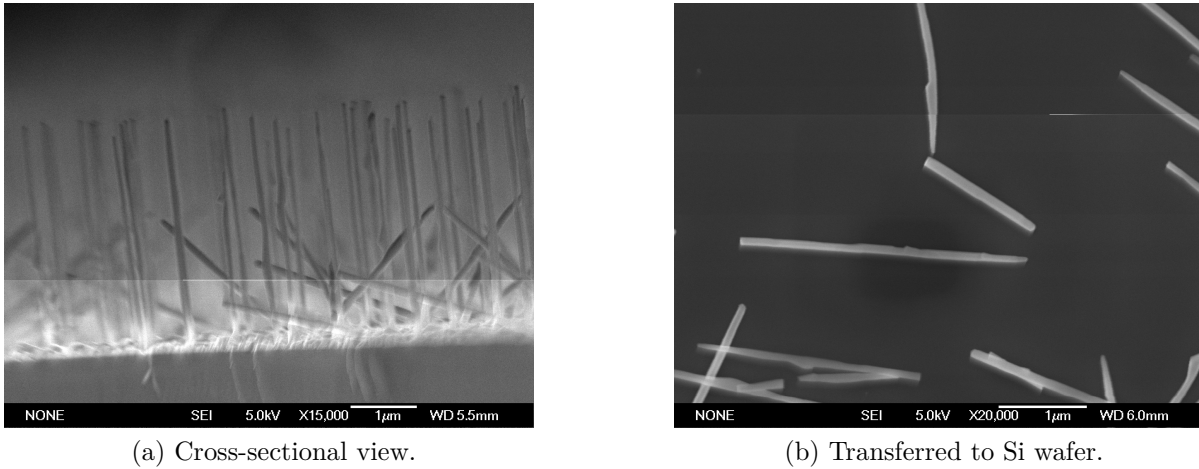


Figure 3.10: GaAs/GaAsN axial nanowires grown with plasma current $I = 10\text{mA}$ and flow rate $F = 2.0\text{ SCCM}$.

3.4.1 Photoluminescence

PL measurements were performed at both room temperature and at 4K. The samples were first measured in the vertically-oriented array geometry. GaAs NW's exhibit room temperature PL, whereas the GaAsN NW's do not. This may be due to the fact that the GaAs/GaAsN core-shell structure has the lower bandgap material on the outside (the "shell") and thus there is no electron confinement which prevents carriers from recombining at the surface. Furthermore, the GaAsN wires appear to have much rougher surface morphology than the GaAs wires as determined by SEM. At low temperature, the GaAsN nanowires exhibit a broad PL at a lower energy, with a luminescence peak centered at 1.31 eV and full-width at half maximum of 0.109 eV. An excitation power dependence of this peak shows that the luminescence can be modeled as a free-to-bound exciton or donor-acceptor pair recombination. The measured power dependence of the PL intensity I was fitted by

$$I \sim L^k \quad (3.3)$$

where L is the power of the exciting laser light, and k is a fitting coefficient. For the data shown, k has a value of 0.89, and it has been shown that for excitation laser energy $h\nu$ lower than the semiconductor bandgap energy Eg , k is generally less than 1 for free-to-bound or donor-acceptor pair recombination[86].

Also observed is the appearance of so-called sharp lines in the GaAsN photoluminescence, which have been reported before as arising from the recombination of carriers through localized and delocalized states[87]. More specifically, the sharp lines are due to the recombination of localized excitons which are confined by radiative centers. The energy and relative intensity of the sharp lines depends on the spatial location of the laser

Table 3.3: Nanowire transfer methods

method	application	description
ultrasonication	TEM samples	ultrasonicate in IPA for 10-60 minutes, transfer via dropper
scratching	not suitable	drag as-grown sample across desired substrate
judicious-tapping	PL & SEM samples	place as-grown sample on desired substrate, tap using tweezers to transfer

spot.

3.4.1.1 Transferred Nanowires

In order to isolate the effect of an individual wire and rule out any effects of either substrate or additional material deposited during the NW growth, micro-PL was performed on NW after transfer to a clean Si(111) substrate. To transfer the wires, three separate methods were used, summarized in Table 3.3. The first, ultrasonication, consisted of placing the as-grown samples in a vial of iso-propyl alcohol (IPA) and sonicating for 10-60 minutes. The sonication process removes the wires from the silicon chip, and the wires can be transferred to another substrate or TEM sample grid by using a dropper. This method was found to be the best for preparing TEM samples. The second method, scratching, involved placing the as-grown sample face down upon another silicon wafer. Tweezers were then used to drag the sample across the transfer substrate, leaving wires deposited on the transfer substrate, albeit many of which may be broken. The third method, “judicious-tapping,” involves placing the as-grown sample face down on another piece of silicon. A pair of tweezers or a diamond scribe are then used to forcefully, but judiciously, tap the back of the the as-grown sample, which results in the transfer or wires to the transfer substrate. This method produced the best results when transferring wires to another silicon chip for PL or SEM studies since it leaves behind a relatively high density of wires in good condition.

The GaAs NW’s exhibit sharp low-temperature PL as shown in Figure 3.11. The luminescence peak at 1.52 eV agrees with results obtained in other works[88] and corresponds to the free exciton emission in zinc-blende GaAs[89], whereas the lower energy peak at approximately 1.48 eV is due to recombination from the wurtzite crystal phase of GaAs, as has been reported previously[90]. From TEM measurements, the samples exhibit mixed zinc-blende and wurtzite phase [91]. This is often the case for GaAs NWs, which typically exhibit highly faulted zinc blende/wurtzite crystal structure and luminescence from both phases is often visible [92, 93]. Both bands also exhibit inhomogenous broadening, likely a result of size dispersion. The relatively large peak width (0.010 eV) could be due to small variations in exciton emission energy caused by strain or compositional inhomogeneities. The intensity of each PL peak as function of excitation power is plotted in the Figure 3.11

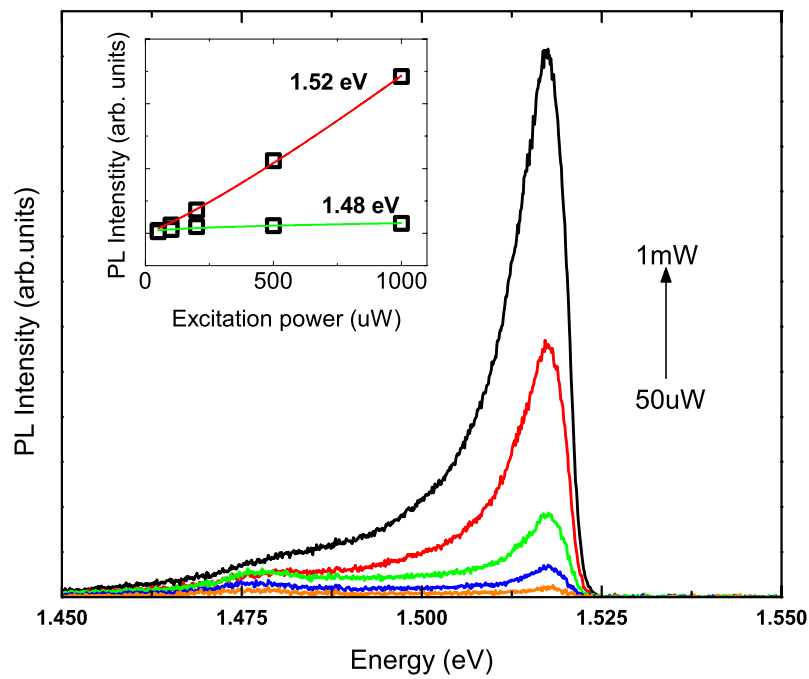


Figure 3.11: PL spectra of single GaAs nanowire at different excitation power from 50 uW to 1 mW at $T=4$ K. Inset shows the excitation power dependence of the PL intensity for the 1.48eV peak (wurtzite phase) and the 1.52 eV phase (zinc blende phase).

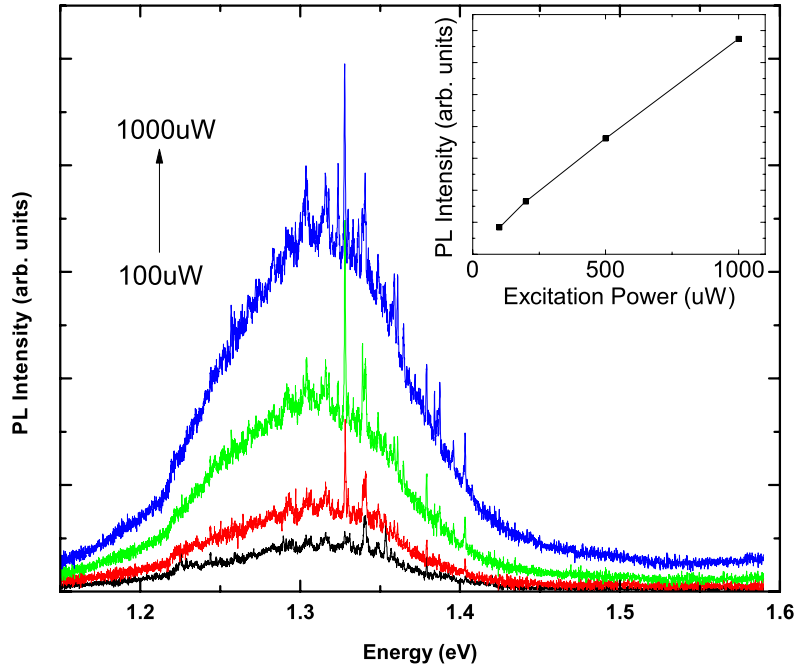


Figure 3.12: PL spectra of GaAsN nanowire array at 4 K, with inset showing the excitation power dependence of the PL intensity of the GaAsN nanowire array.

inset. The luminescence peak associated with the zinc blende GaAs phase has a k value of approximately 1.16, which generally corresponds to a free or bound-exciton emission. For the wurtzite GaAs phase, k is less than 1, which could be indicative of donor-acceptor pair recombination[86].

Micro-PL of the GaAs/GaAsN core-shell structure is displayed in Figure 3.12. The luminescence peak is considerably broadened, due perhaps to the poor quality of the GaAsN layer or lack of a cladding layer. Such degradation of PL efficiency also occurs in GaAsN thin-films, but the efficiency can be improved via post-growth annealing [94]. A shift in luminescence peak to a much lower energy of 1.3 eV is observed, consistent with bandgap reduction due to the incorporation of nitrogen. In Figure 3.13 is shown the low-temperature micro-PL of an individual GaAsN nanowire. The luminescence energy is consistent with that of the vertically-oriented array, and is broad in the region of energy from 1.3-1.35 eV, the sharp lines associated with the recombination of localized excitons are present in the individual wire as well.

Overall, the PL quality of the GaAsN nanowires is poor, and it has been suggested in the literature that an AlGaAs cladding layer has been shown to improve the PL properties of bare GaAs NW's by passivating the GaAs surface[88]. Furthermore, transmission electron microscopy studies of the GaAs and GaAsN nanowires have shown the existence of twinning defects, which have been reported to adversely affect the optical and electronic properties of semiconductor nanowires [95, 96, 97]. Thus, there is considerable room for

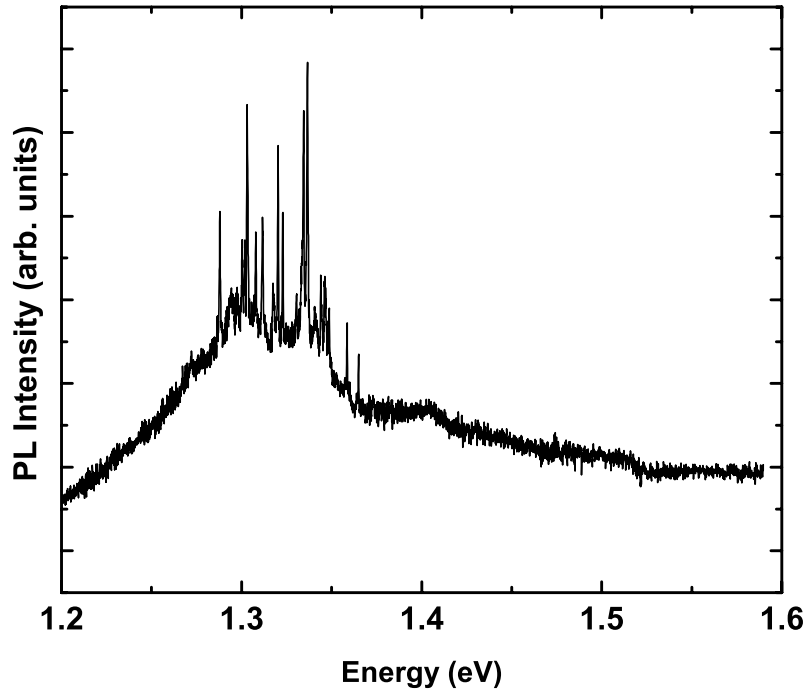


Figure 3.13: Micro-PL spectra of single GaAsN nanowire at $T=4$ K.

improvement in optimizing the optoelectronic properties of these nanowires by improving the structural quality.

3.4.2 Photoreflectance

3.4.2.1 Experimental Description

Photoreflectance (PR) characterization was performed on the samples with the modulation of band bending by a 442 nm line from a chopped HeCd laser with an output power of approximately 30 mW. Monochromatic light was focused on the sample with a Acton double-grating monochromator blazed for 300 nm and collected via the standard lock-in technique. The energy of the pump laser beam determines the highest accessible critical point of the sample under study, thus in this study we are restricted to accessing transitions below 2.8 eV due to the laser energy. Due to the difficulty in measuring PR spectra from NW arrays, which typically exhibit very low reflection, the sample was placed at a 45 degree angle of incidence to the probing beam. All PR measurements were performed at room temperature.

To extract energies of optical transitions in the GaAs and GaAsN NW samples from the PR spectra, these transitions have been fitted by Aspnes' third-derivative functional form of the Lorentzian lineshape[98]

$$\frac{\Delta R}{R}(E) = \text{Re}[C e^{i\theta} (E - E_j + i\Gamma)^{-m}] \quad (3.4)$$

where $\frac{\Delta R}{R}(E)$ is the energy dependence of PR signal, C and θ are the amplitude and phase of the resonance, and E_j and Γ are the energy and the broadening parameter of the optical transition, respectively. The term m depends on the nature of the optical transition, specifically type of critical point: for an excitonic transition $m = 2$, for a three-dimensional one electron transition, $m = 5/2$, and for a two-dimensional one electron transition $m = 3$ [99, 100].

The modulus of the PR resonance ρ was obtained according to Eq. 3.5 with parameters taken from the fit.

$$\Delta\rho(E) = \frac{|C|}{\left[(E - E_j)^2 + \Gamma^2\right]^{\frac{m}{2}}}. \quad (3.5)$$

The integrated modulus of the resonance can be interpreted as the oscillator strength of the optical transition [87, 101]. Broadening is related to both sample quality and temperature. During the fitting, each resonance has to be justified since imaginary transitions can be generated if too many resonances are used to simulate the spectra. To facilitate this, the modulus of each individual resonance is plotted and evaluated, wherein the transition intensity and energy difference between resonances is compared. Thus, allowed transitions will be much stronger than partially allowed ones, and the (temperature induced) broadening of each PR resonance should be comparable. It is accepted that the broadening of PR resonances is higher for excited state, or partially allowed transitions.

3.4.2.2 Results

Figures 3.14 and 3.15 show typical PR spectra from an array of vertically oriented GaAs NW and GaAsN NW's respectively. In the GaAs NW's there is a sharp feature associated with the critical point transition of the energy gap of GaAs, E_0 , at 1.42 eV. In the GaAsN NW's, there are features associated with the energy gap of GaAs, E_0 , at 1.42 eV as well as from the transition from the valence band to E_c at lower energy 1.23 eV. There are also features associated with transitions from the split-off valence band to both the conduction band at approximately 1.55 eV, and to E_c at approximately 1.74 eV. The energies of the critical point transitions were determined by the fitting procedure. In this case a value of $m=3$ yielded the best fit to experimental data, which corresponds to a 3-dimensional critical point transition[102]. No features due to E_+ were observed. Overall, the energies of both the PL luminescence peak and the critical-point transitions determined by PR are in good agreement. However, the introduction of nitrogen also resulted in a decrease of structural quality in the nanowires, as evidenced by the SEM, TEM, and PL results. This could be improved in the future by addressing some of the considerations made when growing GaAsN, such as optimizing the growth temperature[80, 103], and adding an AlGaAs cladding layer to reduce surface recombination.

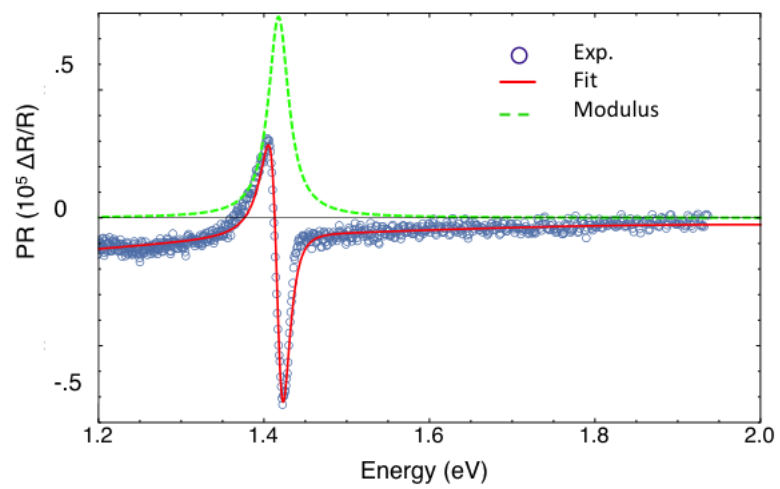


Figure 3.14: PR spectra of GaAs nanowires together with fitted curve (solid line) and decomposition of the individual modulus of PR resonance.

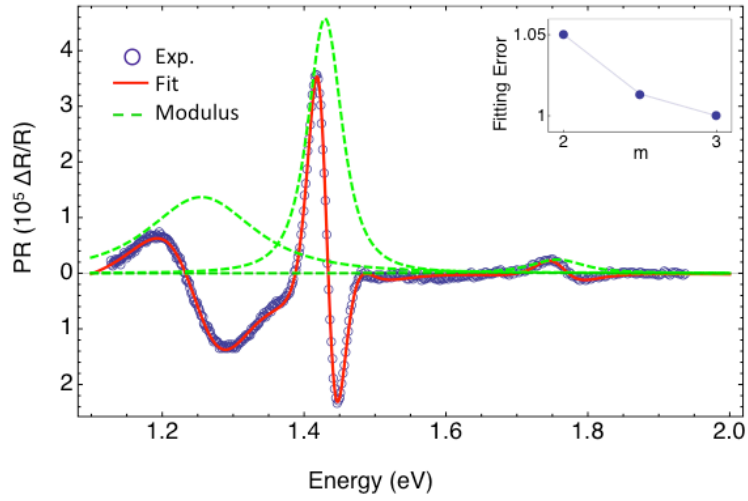


Figure 3.15: PR spectra of GaAsN nanowires together with fitted curve (solid line) and decomposition of the individual modulus of PR resonance. Inset: root-mean-squared curve-fitting error for different m relative to $m=3$.

3.5 Outlook

In summary, the growth of both GaAs and GaAsN nanowires using the self-catalyzed MBE technique was achieved. This approach is novel due to the use of a DC constricted plasma source as a source of nitrogen, which has yielded better film quality in thin-film GaAsN samples. The introduction of nitrogen into GaAs nanowires yielded changes in both the structural (lattice constant) and electrical (bandgap) properties of the nanowires. The electronic structure changes are well-described within the framework of the conduction band anticrossing model. In the future, this technique may provide a promising route for the integration of III-V nanoscale heterostructures on silicon.

Chapter 4

Electronic band structure of GaNPAs

4.1 Theory

Historically, two independent approaches have been used to explain the unusual behavior of dilute nitrides: one is based on detailed band structure calculations from first principles methods[104][105][50][106] while the other is a phenomenological approach based on the experimentally observed band anticrossing effect in the conduction band of dilute nitrides such as GaAsN[42, 107]. While both these approaches are complementary, the second approach, called the band anticrossing (BAC) model, is also supported by theoretical studies based on the tight-binding method [108][109][110]. This model is currently used in a wide variety of work to calculate conduction band dispersion relations in the dilute nitride class of materials.

4.1.1 Band anticrossing model

The BAC model assumes that N atoms, substituted into the group V elements, are randomly distributed in the crystal lattice and weakly coupled to extended states of the host semiconductor matrix [42, 107, 111]. The original BAC model developed for $\text{GaN}_x\text{As}_{1-x}$ alloys considered two sets of states: localized states of substitutional nitrogen atoms and extended states of the GaAs matrix conduction band. Subsequently the model has been modified to consider a larger set of bands with a standard $\mathbf{k} \cdot \mathbf{p}$ approach [112, 113]. In the case of $\text{GaN}_x\text{P}_y\text{As}_{1-x-y}$ alloys, the locations of the conduction band minima in the $\text{GaP}_y\text{As}_{1-y}$ matrix depend on the alloy composition, and in the current case of $\text{GaN}_x\text{P}_{0.4}\text{As}_{0.6-x}$, all the high-symmetry conduction band minima (X, Γ, L) interact with the close lying N level. Interaction of the N-related states with a single conduction band minimum is modeled by the BAC Hamiltonian using perturbation theory.

Figure 4.1 illustrates a 2-level system comprised of a superposition of quantum states $|a\rangle$ and $|b\rangle$. The wave function can be written as a linear combination of orthonormal basis states

$$\psi(x, t) = c_1(t) \phi_1(x) + c_2(t) \phi_2(x). \quad (4.1)$$

The time dependent coefficients c_1 and c_2 satisfy the Schrödinger equation $\hat{\mathcal{H}}|\Psi\rangle = E_\Psi|\Psi\rangle$ in matrix form

$$i\hbar \frac{d}{dt} \begin{pmatrix} c_1(t) \\ c_2(t) \end{pmatrix} = \begin{pmatrix} H_{11} & H_{12} \\ H_{21} & H_{22} \end{pmatrix} \begin{pmatrix} c_1(t) \\ c_2(t) \end{pmatrix} \quad (4.2)$$

with the matrix elements given by

$$H_{ij} = \langle \phi_i(x) | \hat{\mathcal{H}} | \phi_j(x) \rangle. \quad (4.3)$$

The energy eigenvalue problem for this 2-level system is thus given as

$$\begin{vmatrix} E_a & \Delta \\ \Delta & E_b \end{vmatrix} - \mathbf{E} \cdot \mathbf{I} = 0$$

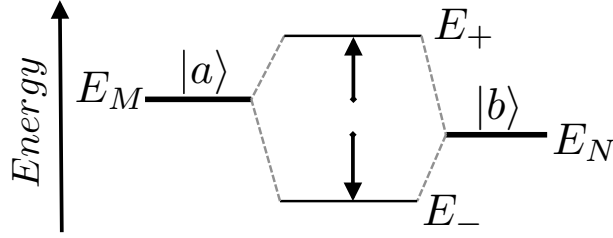


Figure 4.1: Illustration of simple 2 level system.

yielding

$$\begin{vmatrix} E_a - E & \Delta \\ \Delta & E_b - E \end{vmatrix} = 0$$

with Δ a measure of the hybridization strength. More specifically, $|a\rangle$ represents the extended host semiconductor states with energy E_M and $|b\rangle$ represents the localized nitrogen states with energy E_N . Thus, the BAC Hamiltonian can be written as

$$\begin{vmatrix} E_M(\mathbf{k}) & V_{MN}\sqrt{x} \\ V_{MN}\sqrt{x} & E_N \end{vmatrix} = 0 \quad (4.4)$$

where $V_{MN} = \langle k|V|N\rangle$ is the matrix element (coupling constant) describing the interaction between the two states, x is the mole fraction of substitutional N (defect) atoms, $E_M(k)$ is the energy dispersion of the lowest conduction band of the III-V host semiconductor matrix, and E_N is the energy of the N level, with all energies referenced relative to the top of the valence band of the III-V semiconductor host. $|k\rangle$ is the A_1 -symmetric conduction band at the of the III-V host with the energy , and $|N\rangle$ is the A_1 -symmetric level of an isolated nitrogen impurity in T_d symmetry with energy E_N .

Equation 4.4 may be re-written to include a broadening term Γ_d in the many-impurity Anderson model[114] such that

$$\Gamma_d = \pi\beta V^2 \rho_0(E^d) \quad (4.5)$$

where ρ_0 is the unperturbed density of states of the conduction band, with energy dispersion given by $E_{\mathbf{k}}^c$, and β is a prefactor which was experimentally determined to be 0.22 in the case of GaAsN[49].

Thus, the Hamiltonian becomes

$$\begin{vmatrix} E_{\mathbf{k}}^c - E_M(\mathbf{k}) & V_{MN}\sqrt{x} \\ V_{MN}\sqrt{x} & E_N + i\Gamma_d - E(\mathbf{k}) \end{vmatrix} = 0. \quad (4.6)$$

If broadening is neglected, we may take $\Gamma_d = 0$, and Equation 4.6 reduces to the standard BAC Hamiltonian given by Equation 4.4. Thus, the interaction of the dispersionless N-related states with the conduction band states results in a characteristic level anticrossing

interaction that results in a splitting of the conduction band into two highly non-parabolic sub-bands, E_- and E_+ , given by [42]

$$E_{\pm}(\mathbf{k}) = \frac{1}{2} \left\{ E_N + E_M(\mathbf{k}) \pm \sqrt{(E_N - E_M(\mathbf{k}))^2 + 4V_{MN}^2} \right\} \quad (4.7)$$

It has been shown previously that a similar approach can be applied to describe the BAC interaction with minima at the X and L points of the Brillouin zone. The only difference is that the coupling constant, V_{MN} , has to be modified since the conduction band states lose the s -like character with the A_1 symmetry. It was observed that the interaction between N-related states and conduction band states at the boundary of Brillouin zone still exists for dilute nitrides [113]. Some experimental evidence of this interaction has been provided by Mascarenhas *et al.* using resonant Raman scattering [115], and Perkins *et al.* using the electroreflectance technique [116]. Thus, a non-zero V_{MN} element is expected for electron states at the boundary of Brillouin zone. It has been found previously [44] that the V_{MN} element can be expressed as

$$V_{MN}(\mathbf{k}) = \frac{V_{N\Gamma}}{[1 + (a\mathbf{k})^2]^2} \quad (4.8)$$

where a is the parameter of the order of lattice constant describing the spatial extent of the N localization wave function and $V_{N\Gamma}$ is the V_{MN} element for $\mathbf{k}=0$, which should be determined from measurements of the band anti-crossing interaction in the conduction band at the Γ point. Experimentally, it has been observed that $V_{MN}(\mathbf{k})$ at the X point is 3-4 times smaller than $V_{N\Gamma}$ [44].

The BAC model considers only a single nitrogen level on a substitutional lattice site or narrow impurity band and thus ignores mixing with the L and X valleys. Additionally, it does not take into account the formation of N-N pairs or clusters that may form in diluted nitride semiconductors. Other approaches to describe the behavior of this system, such as empirical pseudopotential calculations, can be computationally demanding. However, what the BAC does provide is a solid foundation for describing the material properties of dilute nitride semiconductor alloys, such as the band gap, the temperature dependence of the bandgap, the electron effective mass, and the characteristics of E_- and E_+ close to the center of the Brillouin zone.

4.1.2 Density of states

Following the derivation presented in ref. [117] of the two-level BAC model¹, the density of states of the conduction band edge in a III-V semiconductor can be assumed to have the parabolic form from effective-mass theory

¹See also ref. [118] for a thorough treatment thorough treatment of valence band anticrossing in highly-mismatched alloys.

$$\rho_0(\varepsilon) = 4\pi \frac{\sqrt{\varepsilon - E_0^c}}{\varepsilon_B^{3/2}} \quad (4.9)$$

where ε_B is of the order of the conduction band width and is given by

$$\varepsilon_B = \frac{\hbar^2}{2m^*} (2\pi/b)^2 \quad (4.10)$$

where b is the lattice parameter of the unit cell, and m_e^* is the electron effective mass. The density of states can then be calculated from the imaginary part of the Green's function given by[49]:

$$\rho(E) = \frac{1}{\pi} \int \rho_0(E_{\mathbf{k}}^c) \Im [\mathbf{G}_{\mathbf{k}\mathbf{k}}(E)] dE_{\mathbf{k}}^c \quad (4.11)$$

where $\mathbf{G}_{\mathbf{k}\mathbf{k}}$ is the diagonal Green's function in momentum space according to the Coherent potential approximation (CPA) and written as[49]:

$$\mathbf{G}_{\mathbf{k}\mathbf{k}}(E) = \left[E - E_{\mathbf{k}}^c - \frac{V^2 x}{E - E^d - i\pi\beta V^2 \rho_0(\varepsilon)} \right]^{-1}. \quad (4.12)$$

Figure 4.2 shows the calculated density of states (DOS) of (a) $\text{GaN}_x\text{As}_{1-x}$ and (b) $\text{GaN}_x\text{P}_{0.4}\text{As}_{0.6-x}$ for different N content x under the coherent potential approximation (Equation 4.11)². The dashed vertical lines indicate the position of the N level in the matrix materials. In this calculation, the hybridization parameter $V = 2.84$ eV is taken to be an experimentally-determined constant[45]. This figure shows that the BAC induced splitting of the conduction band results in formation of a narrow intermediate band (IB) that is well separated from the upper conduction band (CB).

This is a band structure configuration envisioned for the intermediate band solar cell concept that utilizes low-energy photons in a two-step absorption process via the intermediate band. The three absorption edges resulting from the optical transitions from VB to CB ($E_{CV} \sim 2.4$ eV), from VB to IB ($E_{IV} \sim 1.5$ eV), and IB to CB ($E_{IC} \sim 0.9$ eV), are close to the band gap distribution for efficient solar power conversion under idealized conditions as described in Chapter 2. The BAC interaction between N states and the extended states of the close lying X and L minima is also calculated and shown in Figure 4.3. The coupling parameter V_{MN} for these minima is much smaller than for the Γ minimum. This results in the splittings at the X and L minima being at least one order of magnitude smaller than the splitting at the Γ minimum, and therefore these are safely ignored.

²The *Mathematica* code for this computation was modified from the work of ref. [117] and can be found in Appendix B.

Table 4.1: Materials parameters used in DOS calculations

	GaN _x As _{1-x}	GaN _x P _{0.4} As _{0.6-x}	GaN _x P _{1-x}
E_N (eV)	1.65	1.86	2.18
V_{MN}	2.7	2.84	3.05
$E_M(k=0)$ (eV)	1.42	1.96	2.72*
m_e^*/m_0	0.067	0.1	1.12*
m_{hh}/m_0	0.51	0.54	0.79*
m_{lh}/m_0	0.082	0.082	
m_{SO}/m_0	0.154	0.154	
Δ_{SO} (eV)	0.34	0.19	
b (Å)	5.65	5.55	5.45

*denotes direct gap

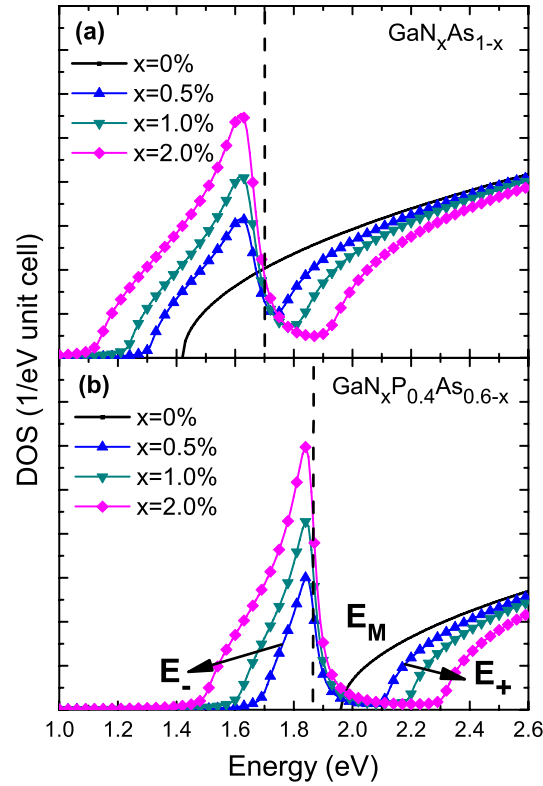


Figure 4.2: Calculated DOS of (a) GaN_xAs_{1-x} and (b) GaN_xP_{0.4}As_{0.6-x} for different N content x . The dashed vertical lines indicate the position of the N level in the matrix materials.

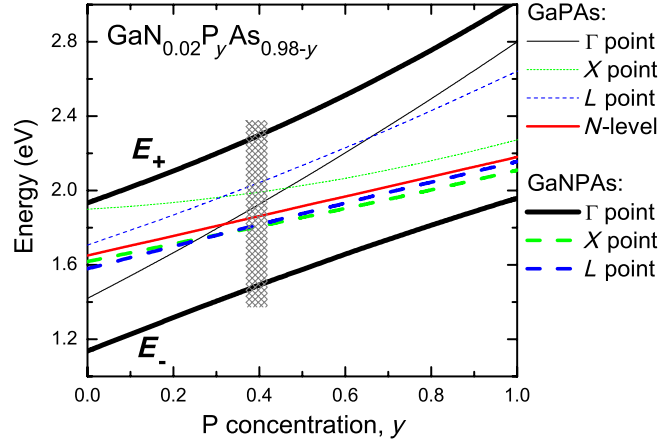


Figure 4.3: Energy gap between the top of valence band and the bottom of conduction band at the Γ (solid black line), X (dashed green line), and L (dashed blue line) points for GaPAs (thin lines) and $\text{GaN}_{0.02}\text{P}_y\text{As}_{0.98-y}$ (thick lines) alloys with various P concentrations. The solid red line shows the position of nitrogen level in GaPAs host.

4.1.3 Optimum GaNPAs alloy composition for IBSC application

In order to find the optimal composition of GaNPAs alloys for IB solar cells, it was determined that for $\text{GaAs}_y\text{P}_{1-y}$ with $y < 0.7$ the nitrogen level lies below the conduction band edge (CBE), as discussed in Chapter 2. Thus, according to the DOS calculations above, we see that the BAC interaction will result in a narrow IB separated from the upper conduction band, unlike the case of $\text{GaN}_x\text{As}_{1-x}$. Furthermore, the electronic structure of $\text{GaN}_x\text{P}_y\text{As}_{1-x-y}$, with x (1%–2%) and y ($0.5 < y < 0.7$), has band gaps which are optimized for IB solar cells with over 60% SQ theoretical efficiency³.

The BAC model was used to calculate energies of E_- and E_+ with various amounts of nitrogen. Results of these calculations are presented in Figure 4.3. Material parameters used for these calculations were taken from Reference[116]. BAC parameters (E_N and V_{MN}) for $\text{GaN}_x\text{P}_y\text{As}_{1-x-y}$ have been calculated as a linear interpolation of the BAC parameters for GaNAs ($E_N = 1.65\text{eV}$ and $V_{MN} = 2.8\text{eV}$ [107][119]) and GaNP ($E_N = 2.18\text{eV}$ and $V_{MN} = 3.05\text{eV}$ [119]). These are summarized in Table 4.1. Additionally, Figure 4.3 also shows the composition dependence of the conduction band minima energies at different symmetry points in the GaPAs host. Indicated by the grey bar in Figure 4.3 the nitrogen level falls below the conduction band minimum in $\text{GaP}_y\text{As}_{1-y}$ with y larger than ~ 0.4 . The calculations presented in Figure 4.3 show that the incorporation of 2% nitrogen into the III-V host material leads to a splitting of the conduction band into the E_+ and E_- sub-bands. The resulting band structure has three optical gaps with energy levels suitable for an ideal intermediate band solar cell.

³Additional information about the choice of alloy composition can be found in Appendix A.2

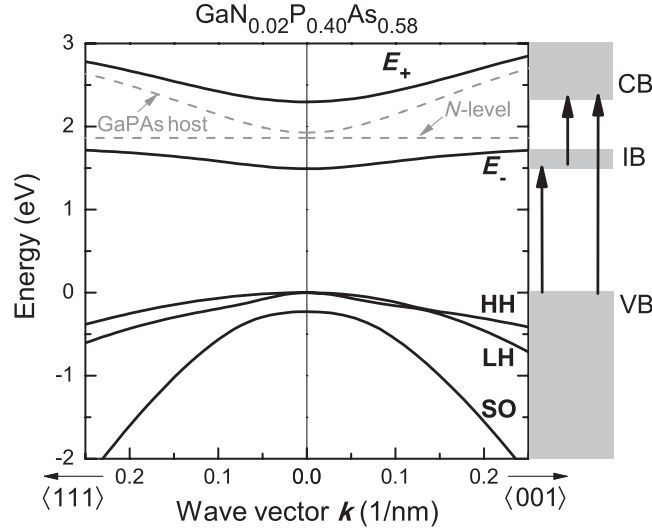


Figure 4.4: Band structure of $\text{GaP}_{0.4}\text{As}_{0.6}$ host (grey lines) obtained within the 8-band $\mathbf{k} \cdot \mathbf{p}$ model and $\text{GaN}_{0.02}\text{P}_{0.40}\text{As}_{0.58}$ (black lines) calculated within the BAC model with following parameters: $E_N=1.86\text{eV}$, $V_{NT}=2.84\text{eV}$, and $V_{NX} = C_{NL} = C_{NT}/4$.

4.1.4 $\mathbf{k} \cdot \mathbf{p}$ calculation

Figure 4.4 shows the calculated dispersion relations for the conduction and the valence bands close to the Γ point of the Brillouin zone. The band structure of the $\text{GaP}_{0.4}\text{As}_{0.6}$ host (shown with grey lines) was obtained using an 8-band $\mathbf{k} \cdot \mathbf{p}$ Hamiltonian⁴. The dispersion relations for the $\text{GaN}_{0.02}\text{P}_y\text{As}_{0.98-y}$ alloy (shown with black lines) were calculated using the BAC model.

4.2 Growth of GaNPAs thin films

The GaNPAs films and structures used in this work were grown by gas-source MBE at University of California, San Diego using a Varian Gen-II MBE system modified to thermally crack gas-phase PH_3 and AsH_3 to P_2 , As_2 and H_2 , respectively. Elemental Ga, solid Si, solid Be, and N radicals produced using radio-frequency plasma activation were used as a Group III source, n-type dopant, p-type dopant, and N source, respectively. The films were grown on GaP (100) substrates. Since $\text{GaN}_x\text{P}_y\text{As}_{1-y-x}$ in the target composition range of ($0.5 < y < 0.7$) has a significant lattice mismatch to the GaP substrate, a linearly graded GaAsP buffer layer was first grown to slowly expand the lattice constant and to control misfit dislocations. Following the buffer layer, a $0.5 \mu\text{m}$ GaAsP layer with constant As composition was grown to relieve the residual strain. The structure up to this point is referred to as the “template” throughout. Then the top $0.5\text{-}\mu\text{m}$ -thick $\text{GaN}_x\text{P}_y\text{As}_{1-x-y}$

⁴See Appendix for details on the $\mathbf{k} \cdot \mathbf{p}$ calculation and approach.

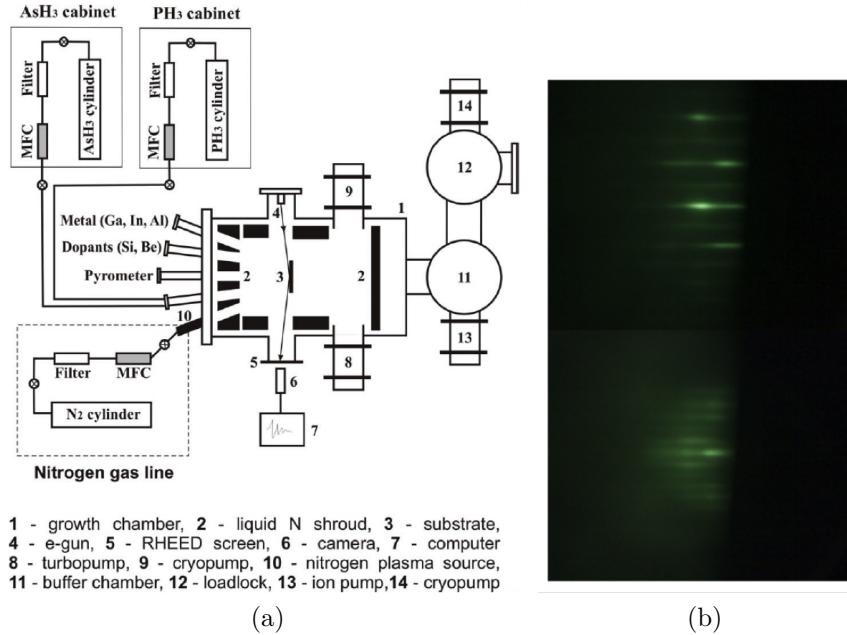


Figure 4.5: (a) Overview of gas source MBE used for growth of metamorphic GaNAsP samples, courtesy Y. Kuang, UCSD. (b) RHEED images from sample growth.

layer was grown at 520 °C atop the template. Samples with the top layer of GaAsP and without N were also grown as control groups. Finally, in order to improve optical properties of GaNPAs layers, certain samples were annealed at 900°C for 60 s in 95% N₂ and 5% H₂ forming gas ambient.

The composition profiles and depth profiles of the films were measured using channeling Rutherford backscattering spectrometry (c-RBS) together with nuclear reaction analysis (NRA). The $^{14}\text{N}(\alpha, p)^{17}\text{O}$ reaction with a 3.72 MeV $^4\text{He}^{2+}$ beam was used for the detection of nitrogen. A 150 mm² passivated implanted planar silicon (PIPS) detector with a 3 × 12 mm slit was used to detect the emitted protons at an angle of 135° with respect to the incident beam. A 25 μm thick mylar foil was placed in front of the detector to absorb the backscattered alpha particles. RBS spectra were also obtained simultaneously at 168° with another PIPS detector. Both RBS and NRA measurements were carried out in the random and <100>, <110>, and <111> axial channeling directions. The fraction of substitutional nitrogen atoms in the films was obtained by comparing the random and channeling yields of both the RBS and NRA measurements

Figure 4.6 illustrates a design schematic (left) of one of our samples along with the atomic profile (right) of the film structure as determined using RBS. The RBS results are fit using the SIMNRA[120] and SIMTarget[121] software packages. The channeling c-RBS shows that samples grown in this particular structure are of good crystalline quality with minimum channeling yield of ~5%. Furthermore, the increment in arsenic content can be seen in the linearly graded buffer layer, from 0% As at the GaP substrate to ~44% As in

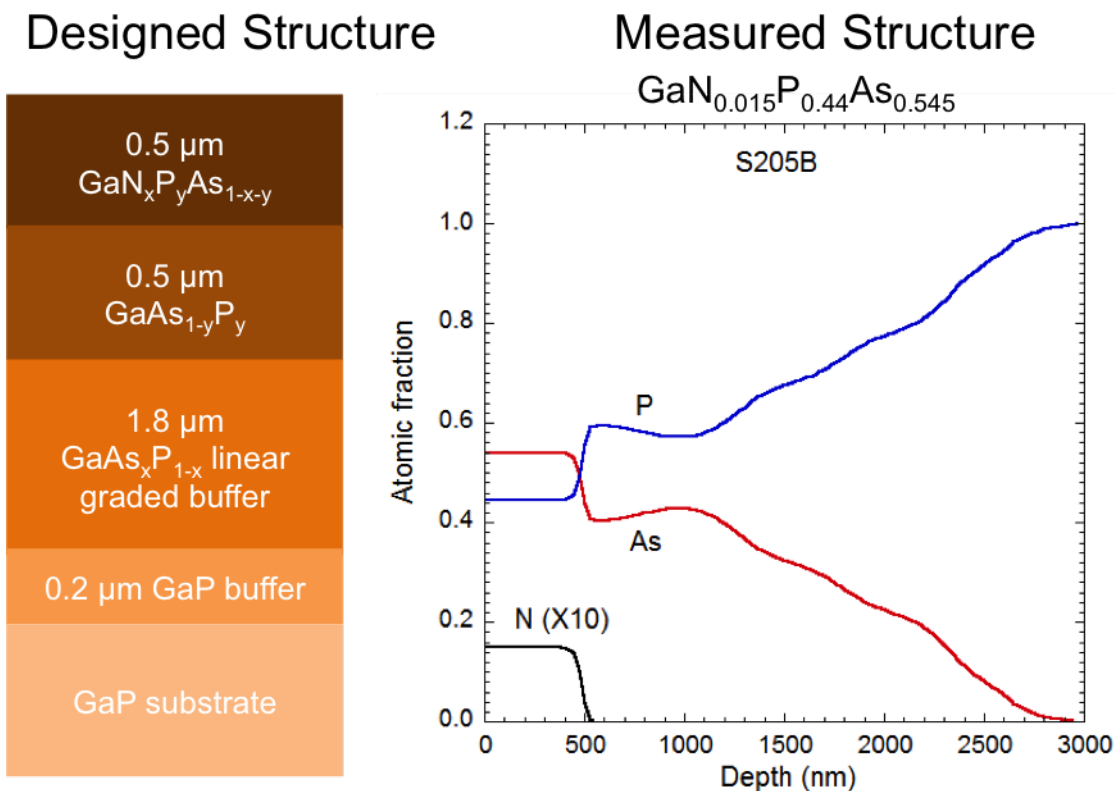


Figure 4.6: The designed structure (left) of GaNPAs and the measured composition profile by Rutherford back scatteringspectrometry and nuclear reaction analysis (right).

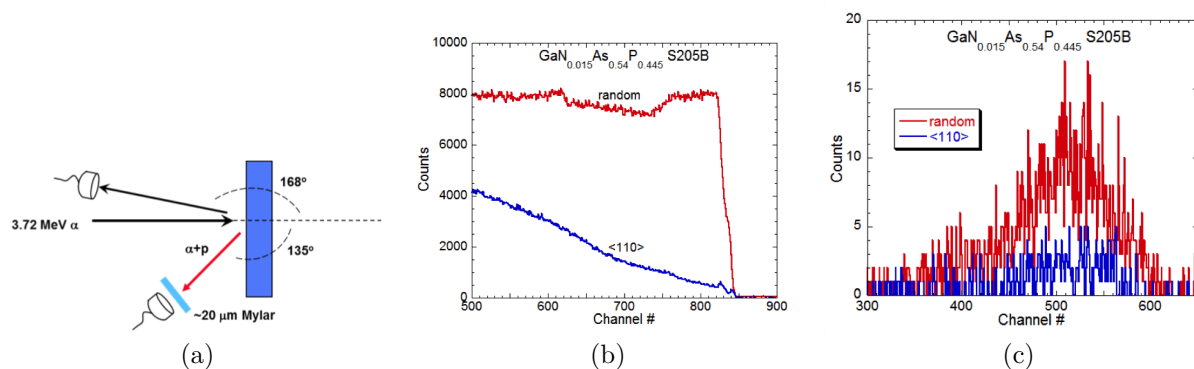


Figure 4.7: (a) RBS measurement geometry, image courtesy K.M. Yu. (b) Channeling RBS measurement of and (c) channeling NRA of $\text{GaN}_{0.015}\text{P}_{0.445}\text{As}_{0.54}$ sample.

the top GaNPAs layer. Both channeling RBS and NRA revealed that the substitutional N fraction is $\geq 80\%$ for all samples. Further details on the growth process have been previously reported elsewhere [122, 123]. Though the samples studied are grown on GaP substrates at present, both GaPN and GaAsPN have also been grown on silicon substrates and demonstrated to be of high optical quality [124, 125, 126], offering a possible avenue for the integration of these dilute nitride alloy materials on silicon.

4.3 Optical measurements

In order to verify the above predictions and identify experimentally features related to IB formation in GaNPAs alloys, PL, PR, and absorption techniques were used to study the GaNPAs samples with variable N (0.56-1.5%) and P (38-45%) concentrations.

4.3.1 Experimental setup

Photoluminescence (PL) measurements were performed at room temperature using a 325 nm HeCd 50 mW laser as an excitation source and a Hamamatsu R928 photomultiplier tube as a signal detector. For low temperature measurements, the samples were cooled to ~ 7 K inside of an evacuated cryostat by making contact to a cold finger connected to a closed-cycle helium refrigerator. For the PR measurements, samples were excited by the 442 nm line from a HeCd laser, and the signal was detected by a Si detector using the lock-in technique. Absorption coefficients of the films were obtained by transmission and reflection measurements using a Perkin Elmer Lambda 950 photospectrometer.

4.3.2 Photoluminescence

Figure 4.8 shows the room temperature PL of a representative $\text{GaN}_{0.015}\text{As}_{0.54}\text{P}_{0.445}$ sample (S205B) along with a reference $\text{GaAs}_{0.59}\text{P}_{0.41}$ sample (S205A). At this As composition in GaAsP sample, the minimum at the Γ point is located at about 2 eV above the valence band edge (VBE) and slightly below the minimum of the X band. The incorporation of N results in admixing of the Γ component with the lowest CB states, enhancing the oscillator strength for radiative recombination which significantly increases the PL intensity of the dilute nitride sample (S205B). N also redshifts the PL peak, broadens the line width, and heaves up a band tail on the low energy side, which is believed to be a thermal distribution of N-related states below the newly formed CBE (E_c).

The PL peak position coincides with the E_c signal from the PR measurement (Figure 4.9). Although the N level lies below the Γ valley in both GaP and GaAsP within the composition range of study, this relatively good agreement indicates that the major contribution to PL is due to band-to-band transitions. It is not attributed to the recombination of excitons trapped by N-related deep centers below the bandgap [127]. This is further evidenced by the synchronized blueshift of the PL peak position and the E_c position on

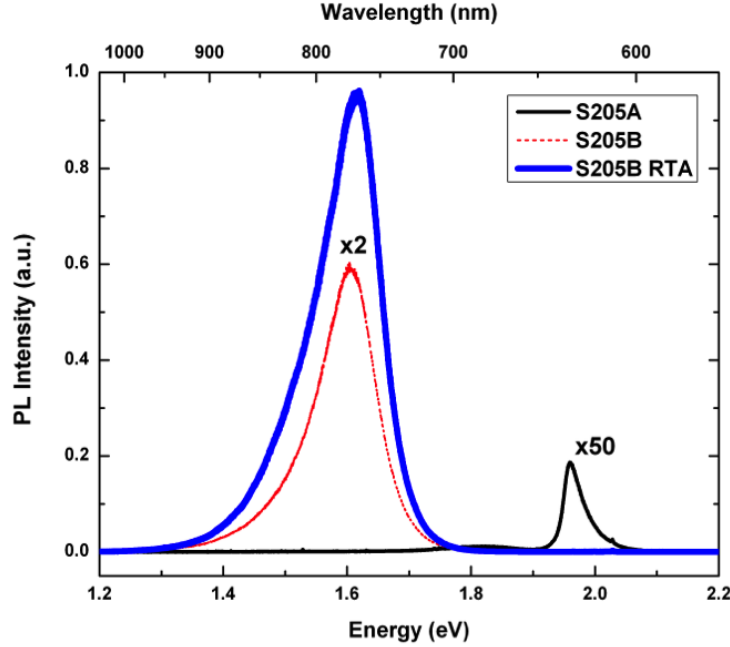


Figure 4.8: Room-temperature photoluminescence of GaAsP (S205A), GaNAsP (S205B) and GaNAsP after rapid thermal annealing (S205B RTA).

the sample subjected to rapid thermal annealing (at 900 °C for 60s in 95% N₂ and 5% H₂ forming gas ambient). The 3-fold increase in PL intensity suggests that N-related centers do exist in the as-grown sample serve and as non-radiative recombination centers. An RTA step, however, effectively removes them and suppresses the non-radiative channels.

4.3.3 Photoreflectance

Figure 4.9 shows PR measurements of a series of GaNPA samples containing the GaAsP reference sample, and both the as-grown and annealed GaNPA samples. In the GaAsP sample, only two transitions are seen, from VB to CB and from the split-off (SO) valence band to CB. In the GaNPA samples, however, the inter-band transitions VB→E⁻ and VB→E⁺ as well as their SO counterparts are clearly resolved in the PR spectrum. The theoretical values of E₋ and E₊ for S205B are plotted as grey bars in the figure. By using the linear interpolated values for E_N, E_M, and V_{MN} shown in Table 4.1, the energy of the conduction sub-bands, E₋ and E₊, from the BAC model agree with the experimental results. This has an important technical implication since the IB solar cell efficiency changes drastically as the energy gaps change, as discussed in Chapter 2. From a material growth perspective, the well predicted splitting of the conduction band by the BAC model greatly decreases the difficulty in IB position tuning, hence makes it easier

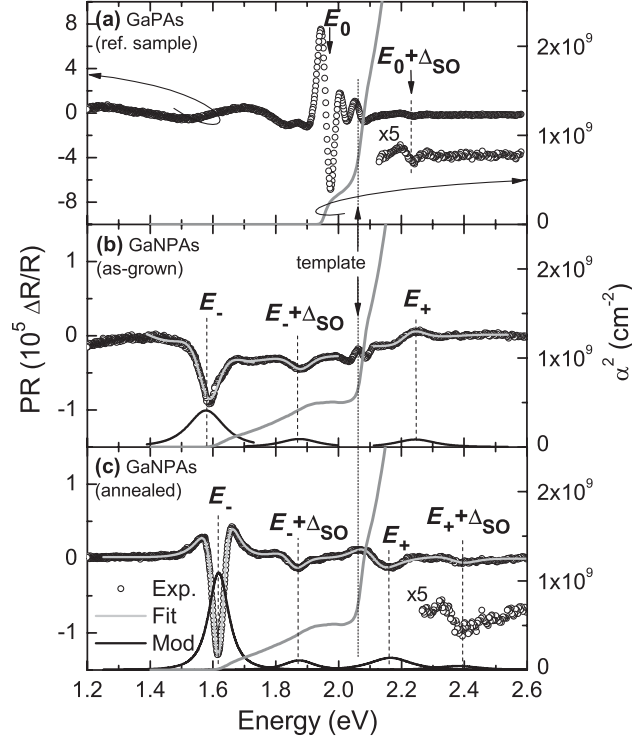


Figure 4.9: Room-temperature photoreflectance and absorption spectra for GaP0.46As0.54 (a), as-grown GaN0.015P0.445As0.54 (b), and annealed GaN0.015P0.445As0.54 (c) samples.

to grow the material in the optimal compositions.

Figure 4.9 shows PR and absorption spectra measured at room temperature for GaPAs (reference sample) and GaNAsP samples (both as-grown and annealed). PR resonances related to the energy gap (E_0) and the spin-orbit split ($E_0 + \Delta_{SO}$) transitions are observed for the reference sample. For GaNAsP samples the E_- and E_+ transitions are visible instead of the E_0 transition. Additionally, the $E_- + \Delta_{SO}$ and $E_+ + \Delta_{SO}$ transitions are visible in these samples. The spin-orbit splitting in N-free and N-containing alloys is the same within experimental error and equals 283, 282, and 270 meV for GaPAs, as-grown GaNPAs and annealed GaNPAs samples, respectively. This observation confirms that the incorporation of nitrogen into the GaPAs host changes the CB without any significant effect on the VB. Very similar PR spectra were observed for other GaNPAs samples studied. However, as shown in Figure 4.10, in some samples a strong PR signal from the GaPAs template interfered with optical transitions from the GaNPAs layer as it is quite close in energy. The E_0 transition in the GaPAs template is easy to recognize, however, as it coincides with the absorption edge marked by the dashed vertical line in Figures 4.9 and 4.10.

In order to extract energies of optical transitions in GaNPAs layers from PR spectra,

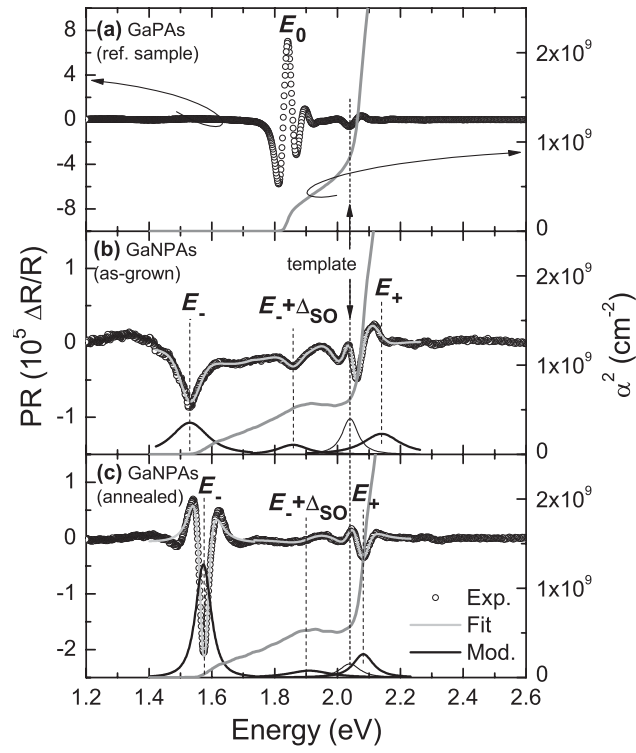


Figure 4.10: Room-temperature photoreflectance and absorption spectra for $\text{GaP}_{0.38}\text{As}_{0.62}$ (a), as-grown $\text{GaN}_{0.012}\text{P}_{0.38}\text{As}_{0.608}$ (b), and annealed $\text{GaN}_{0.012}\text{P}_{0.38}\text{As}_{0.608}$ (c) samples.

these transitions have been fitted by the Aspnes formula (equation 3.4)

$$\frac{\Delta R}{R}(E) = \text{Re}[Ce^{i\theta}(E - E_j + i\Gamma)^{-m}]. \quad (4.13)$$

The fitted curves are shown as thick grey lines in Figures 4.9 and 4.10 together with the moduli of PR resonances, which are shown as solid black lines. The modulus of the PR resonances (ρ) was obtained according to Equation 3.5 with parameters taken from the fitting procedure.

4.3.3.1 Influence of thermal annealing

A post-growth annealing step was performed on some of the GaNPAs samples and found to influence the spectral position and strength of the optical transitions. By analysis of the moduli of the PR transitions for the as-grown and annealed samples, it is visible that the E_- transition is blue-shifted while the E_+ transition becomes redshifted after annealing. Such behavior of the E_- and E_+ transitions is consistent with the reduction and/or passivation of substitutional N in GaNAsP during annealing. A blueshift of E_- transition was also observed for GaInNAs layers, but in this material the blueshift phenomenon is mostly attributed to the change in the nitrogen nearest-neighbor environment from Ga-rich to In-rich [39-41]. For GaInNAs it has also been reported that substitutional nitrogen atoms with different nearest-neighbor environment influences the coupling element V_{MN} in BAC model and thus also affects the energy gap [42]. It is also possible that energies of the E_- and E_+ transitions can vary with the same nitrogen concentration due to a different nitrogen nearest-neighbor environment. This would also influence the coupling element in the GaNPAs alloys. Thermal annealing is a frequently-used technique to improve the optical quality of dilute nitrides. As is shown in the Figs. 3 and 4 a significant reduction of the linewidth is observed in the PR spectra of the annealed GaNPAs layers. Narrowing of the optical transitions in modulated reflectance spectra was also observed for other dilute nitrides [43] and has been attributed to an improvement of the alloy homogeneity and/or a reduction of point defects in these layers.

Figure 4.11 shows theoretical predictions of the transition energies from the valence band to E_- and E_+ sub-bands in $\text{GaN}_x\text{P}_y\text{As}_{1-x-y}$ alloys with various nitrogen concentrations. The calculations are compared with experimental data for the as-grown (solid points) and annealed (open points) GaNPAs samples. The theoretical predictions are compared to samples with three different P concentrations ($y=0.38, 0.4$ and 0.44) as determined by RBS. Although there is good agreement between the BAC calculations and the experiment, it is clear that the agreement is better for the E_- rather than for the E_+ transition. This is not surprising as the E_+ transitions in some of the samples interfere with the optical transitions from the template and become more difficult to measure accurately. Furthermore, the accuracy of the substitutional N fraction measured by c-RBS and c-NRA is $\sim 15\%$, and this is within the changes observed between as-grown and annealed samples.

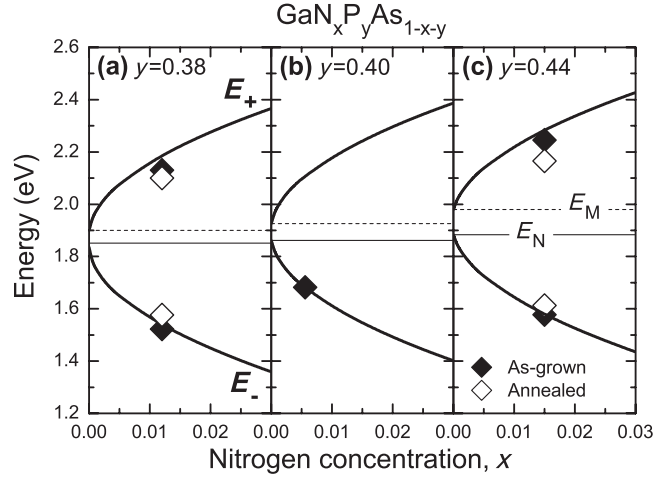


Figure 4.11: Energies of the E_- and E_+ transitions for as-grown (solid points) and annealed (open points) GaNPAs layers, along with theoretical predictions obtained within the BAC model.

The results in Figure 4.11 confirm experimentally that $\text{GaN}_x\text{P}_{0.4}\text{As}_{0.6-x}$ alloys with $\sim 1-2\%$ of N have a band structure suitable for IB solar cells. This agrees with the calculated DOS for GaNAsP and GaNAs shown in Figure 4.2, which shows that the IB in GaNAsP is more isolated from E_+ .

4.3.4 Absorption

Figure 4.12 shows the absorption coefficients of the same sample group, both of which show multiple absorption edges corresponding to different layer in the samples. In the GaAsP sample (S205A), absorption takes off at $\sim 1.95\text{eV}$, from the $\Gamma_V-\Gamma_C$ transition, in good agreement with the PL data. The small amount of N incorporation clearly redshifts the absorption edge from $\sim 1.95\text{eV}$ to $\sim 1.6\text{eV}$ in S205B. The position of the absorption edge also is in good agreement with the PL and PR data, suggesting its origin from the $\text{VB}\rightarrow\text{E}$ transition. Note that for all of our GaNAsP samples the intermediate band (E_- band) exhibits strong absorption with $\alpha > 2 \times 10^4 \text{ cm}^{-1}$. This suggests that using GaNAsP layers as the absorber in an IB solar cell requires only a layer thickness $\sim 1 \mu\text{m}$. The PR spectra along with PA spectra clearly demonstrate the intermediate band behavior of GaNAsP sample.

However, an important requirement for an efficient IBSC is a strong enough absorption for the optical transitions from the VB to IB and from the IB to CB. In the case of GaNPAs with the nitrogen level located below the GaPAs conduction band, the character of the IB is mostly determined by the highly localized N states and the question arises as to whether there is strong enough optical coupling between the extended band states and the IB. The absorption spectra measured on different samples are shown in Figure 4.13.

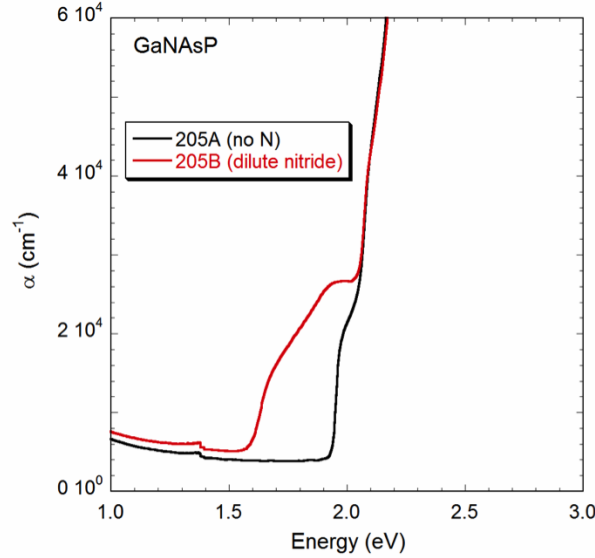
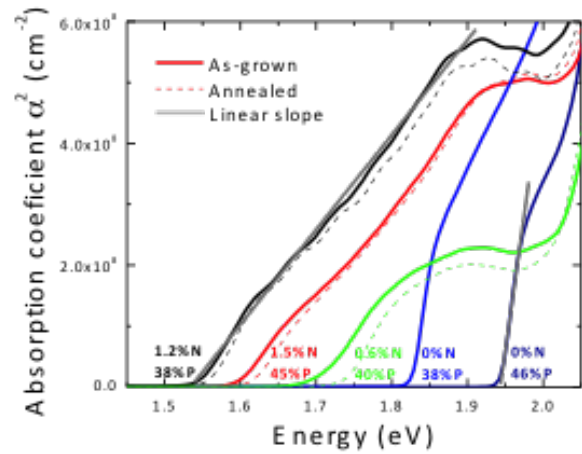


Figure 4.12: Absorption coefficients of GaAsP (S205A) and GaNAsP (S205B) samples.

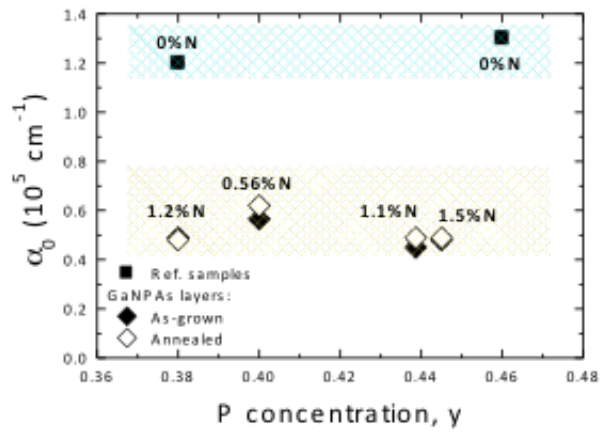
As expected, changing P concentration from 38% to 46% in N-free alloys changes the absorption edge E_0 to higher energy without affecting the shape of the edge. In the case of GaNPAs films we observe a large downward shift of the absorption edge, indicating an onset of the transitions from the VB to IB (E_{\perp}). The low energy optical absorption has a tendency to saturate at higher energies of about 1.8 to 2 eV with the saturation level dependent on the N content. This behavior reflects the fact that the nature of the IB states and thus also that the dipole matrix element for the transitions from the VB to IB depends on the \mathbf{k} vector. At small \mathbf{k} 's the IB states have a large admixture of the s -like CB states that strongly couple to the p -like VB states. As shown in Figure 4.4, at large \mathbf{k} values the IB states approach E_N and become more localized with weaker optical coupling to the extended VB states. This effect results in the saturation of the optical absorption for the VB to IB transitions. In order to evaluate the absorption edge energy and the relative strength of the optical absorption from the spectra in Figure 4.13, a standard formula is used to describe absorption coefficient as a function of photon energy, $E = h\nu$

$$\alpha(E) = \alpha_0 \sqrt{\frac{E - E_g}{E_g}} \quad (4.14)$$

where E_g is the energy gap and α_0 is a constant that represents the strength of the optical absorption. The straight lines in Figure 4.13 represent the fits and are used to determine E_g and α_0 . The values of α_0 for different samples are plotted in Figure 4.13. It is evident that the incorporation of nitrogen into the GaPAs host leads to the formation of an IB with an absorption coefficient of about $0.5 \times 10^5 \text{ cm}^{-1}$ for the VB \rightarrow IB transition, which is about 50-60% smaller than the absorption coefficient for the VB \rightarrow CB transition in the GaPAs host. This indicates that the GaNPAs thin films have an optical absorption for



(a)



(b)

Figure 4.13: (a) Room-temperature absorption spectra of GaNPAs samples of various contents. (b) Absorption coefficient α_0 determined for GaNPAs alloys of various contents.

the VB to IB transitions strong enough to be used in thin film IB solar cells. For example, >90% of the incident light with photon energy larger than E_i will be absorbed by only 0.5 μm thick layer of GaNAsP.

4.4 Conclusion

In conclusion, the structural, and optical properties of high-quality $\text{GaN}_x\text{As}_y\text{P}_{1-x-y}$ layers grown by gas source MBE were investigated. Channeling NRA-RBS measurements confirm the composition profile of $\text{GaN}_x\text{P}_{1-x-y}\text{As}_y$ grown on GaP(100) substrate through a GaAsP linearly graded metamorphic buffer layer with $\geq 80\%$ substitutional N in the layer. PL, PR and PA results clearly demonstrate the good optical quality of the MBE grown GaNAsP samples and their intermediate band characteristics. The high absorption coefficient of the IB suggests that this material is suitable as an absorber for IB solar cell application.

Additionally, the optical properties of $\text{GaN}_x\text{P}_y\text{As}_{1-x-y}$ alloys in the whole P composition range were studied. Calculations of the electronic band structure based on the BAC model indicate that dilute nitride GaNPAs with $\sim 40\%$ P has a band structure and optical properties suitable for application in intermediate band solar cells. The predictions have been experimentally tested on GaNPAs alloys with P content ranging from 38 to 45%. The energies of the optical transitions are in excellent agreement with the BAC calculations. Measurements of the optical absorption show a strong optical coupling between the valence band and the intermediate band, which is a key requirement for the application of GaNPAs alloys in thin-film intermediate band solar cells.

Chapter 5

Towards GaNPAs based IBSC devices

5.1 Introduction

Ultimately, to assess the suitability of GaNPAs for application as an IBSC material, the doping properties need to be investigated. P- and n-type layers would allow for the formation of a pn junction, a critical component of a working IBSC solar cell. Thus, the optical and electrical properties of intentionally doped GaNPAs alloys need to be studied. Another crucial measurement is to evaluate the strength of the complementary IB to CB transitions, as this transition allows the IB to act as a stepping stone, as discussed in Chapter 2. Also of critical importance is the charge transport in the conduction band. These measurements are essential to evaluate the suitability of GaNPAs alloys for application in intermediate band solar cells.

5.2 Growth of doped GaNPAs layers

5.2.1 Growth of doped GaNPAs layers

To grow the n- and p-type doped GaNPAs layers, various Si and Be fluxes were used to achieve different doping levels. It is worth noting that to achieve active silicon dopants in the dilute nitrides, the growth temperature has to be lower than the critical temperature, T_c , so that the diffusion length of the N atoms becomes very small. Thus the N atoms will not encounter a Si adatom on the surface during growth. Otherwise, the N and Si adatoms will form a bond and become a Si-N split interstitial defect complex. Furthermore, if the growth temperature is lower than T_c , a N atom still has some probability to hit a Si atom on the surface during deposition. The active silicon dopants will then decrease exponentially as the N composition increases. For example, ~60% silicon atoms act as active dopants for GaAsN with [N]=0.5% but only ~20% active for [N]=2%.

5.3 Characterization of doped GaNPAs layers

5.3.1 Electrical properties

Electrical measurements were made using Hall effect measurements in the van der Pauw geometry using an Ecopia HMS3000 system with a 0.6 Tesla magnet. To make contacts, a soldering iron was used to melt small indium droplets on all four corners of the square samples. A RTA ($T < 450^\circ\text{C}$) was found to help reduce contact resistance.

Figure 5.1 summarizes the electrical properties of n-type doped samples. Room-temperature Hall effect and resistivity measurements reveal that electron concentration in the samples ranged from 5.0×10^{17} up to $3.0 \times 10^{18} \text{cm}^{-3}$. It was not possible to achieve an electron concentration higher than $N \sim 3 \times 10^{18} \text{cm}^{-3}$. In fact, the beam flux during Si doping for the $3 \times 10^{18} \text{cm}^{-3}$ sample was actually calibrated for 1.0×10^{19} electrons. The sample was grown at very low temperature ($\sim 400^\circ\text{C}$) in an effort to prevent the formation of Si-N

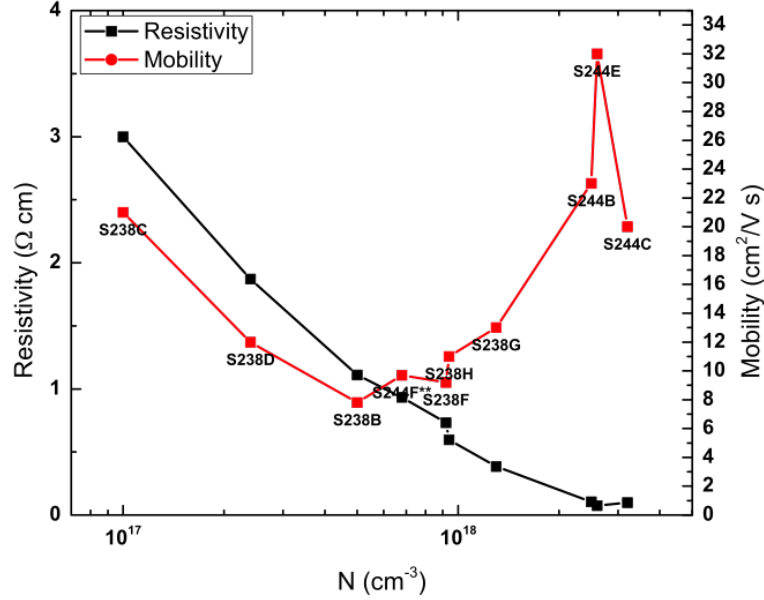


Figure 5.1: Resistivity and mobility of n-type doped GaAsPN:Si.

defect complexes, however, it is likely that Si-N defect complexes may still contribute to the lower than expected dopant activation in the n-type doped samples. Furthermore, the p-type doping was not affected by the presence of nitrogen¹.

The apparent “U”-like shape in the mobility vs electron concentration plot is likely due to ionized impurity scattering from dopants. The sample points in the bottom of the “U” were doped with a very high silicon flux during the growth (high Si cell temperature). The electron concentration may not be necessarily higher than other samples (like samples S244B and S244C) due to auto-compensation. But the mobility is indeed lower.

Furthermore, sufficient n-type doping is important because a high enough electron concentration is needed so that the Fermi level will be close to (or within) the intermediate band. This would result in the intermediate band being partially occupied with carrier, and having sufficient carriers such that the IB→CB transition probability would not depend on photo-filling of the intermediate band from high levels of solar flux. In order for photo-filling to make a notable impact on the carrier population in the intermediate band, very high photon fluxes are required, and would practically be achieved only by very high levels of solar concentration (1000x and above) [129, 5].

¹Yanjin Kuang, personal communication, April, 2013. For further treatment discussion on the MBE growth of doped GaNPs, we refer the interested reader to Ref. [128].

5.3.2 Optical properties

There is also evidence for the formation of Si-N defect complexes. At very high silicon flux during growth the mobility is reduced. Furthermore, after a post-growth rapid-thermal anneal (RTA) step, the samples exhibit a lower energy luminescence peak that is characteristic of mutual passivation[130].

Figure 5.2 shows the photoreflectance of n-type GaNPs with increasing electron concentration, along with an undoped GaNPs for reference. Several features are readily apparent. First, both the E_- and E_+ are visible, as well as features due to the split-off valence band (SO). This has been reported in previous work in the case of undoped GaNPs[123], and it is significant that these features are also present in the doped samples.

In fact, for samples with lower electron concentration (such as 10^{17} range) the optical transitions between the valence band and both the E_- and E_+ sub-bands are much stronger than in the undoped samples. The reason for this is that the surface band bending is much stronger in the GaNPs:Si n-type doped samples, which is illustrated in Figure 5.4. Furthermore, as the electron concentration is increased due to higher doping, we observe that the intensity of the PR signal is drastically reduced, and by the time the electron concentration has reached the 10^{18} range, the spectral features associated with either $VB \rightarrow E_-$ or $VB \rightarrow E_+$ energy transitions diminish and become hardly visible. Though not shown, the same behavior is also observed in the p-type doped samples. This observation can be explained by the fact that at higher electron (hole) concentration the surface depletion (accumulation) layer decreases in width, as illustrated in Figure 5.5. Due to the higher concentration of electrons (holes) and the resulting high surface band-bending from the dopants, the photo-generated carriers from the PR laser have much less effect on the modulation band bending of the sample, and the resulting PR spectral features are diminished.

5.3.3 Time-resolved PL

For the time-resolved PL characterization, the samples were contained in a closed-cycle helium refrigerator, allowing for measurements at variable temperature. Samples were excited by the second harmonic from a (415 nm) mode-locked Ti:Sapphire laser with pulse duration of 150 fs. The laser beam was focused on the sample to a spot diameter of ~ 0.2 mm. The average power of the pulsed laser beam used in the experiment was 3 mW. The PL signal was dispersed by a 0.3m-focal length monochromator and detected by a Hamamatsu streak camera equipped with an S-20 photocathode.

5.4 Design of GaNAsP IBSC device

As introduced in Chapter 2, one of the key requirements of an IBSC is electrical isolation of the IB, as it remains solely as a “stepping-stone”. This is essential in allowing

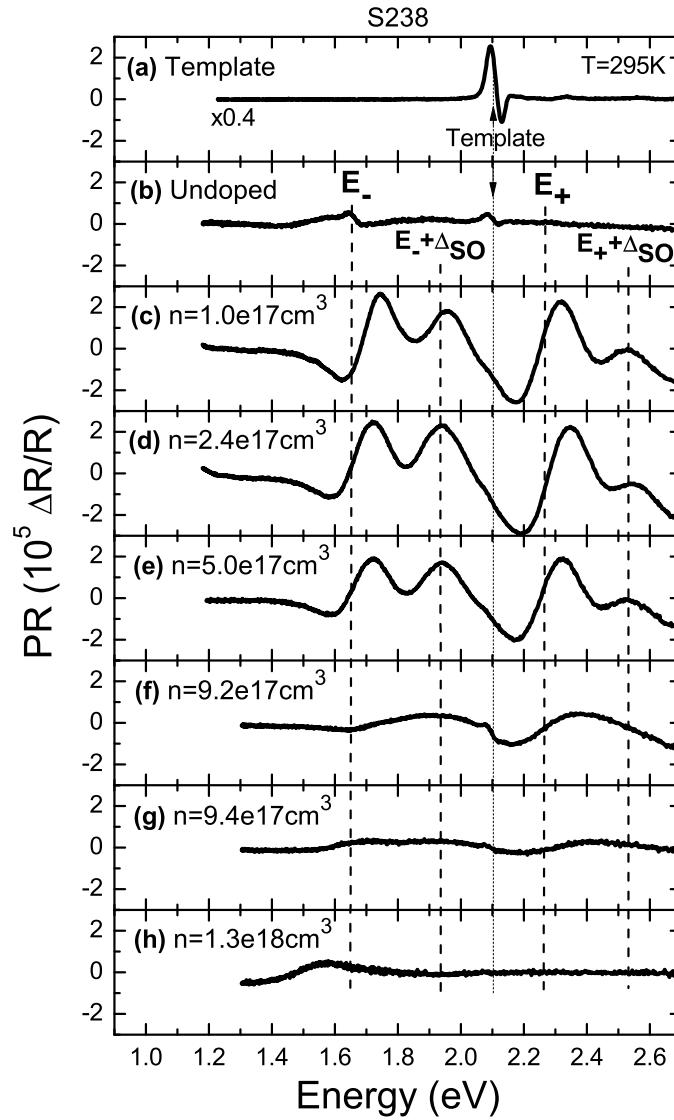


Figure 5.2: Photoreflectance of n-type doped GaNPAs, showing evidence of both the VB E_- and VB to E_+ transitions. At higher electron concentrations, the modulation band-bending is drastically decreased.

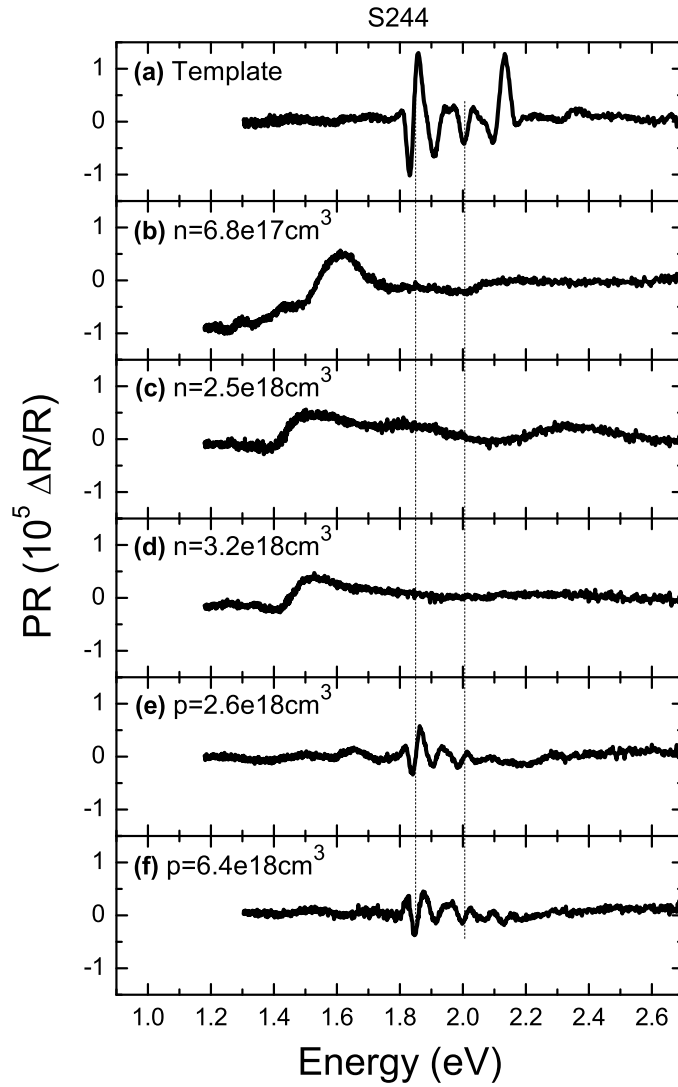


Figure 5.3: Photoreflectance of n-type (b,c,d), and p-type (e,f) doped GaNPAs samples. At higher electron concentrations, the modulation band-bending is drastically decreased and the spectral features associated with transitions from VB to either E_- or E_+ are absent.

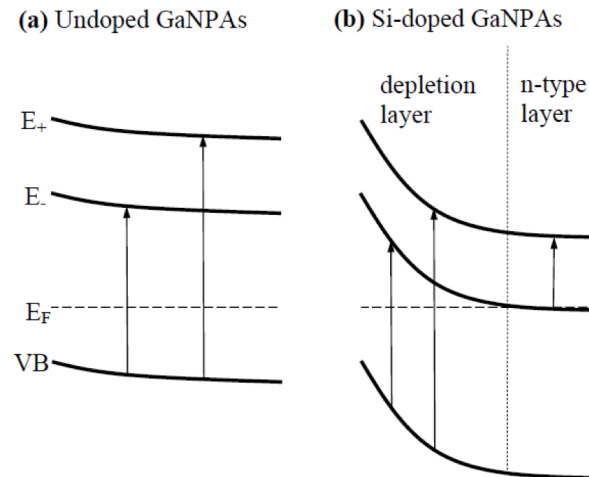


Figure 5.4: Illustrative band diagram of (a) undoped GaNPAs sample and (b) n-type GaNPAs:Si, which much higher band bending at the surface as a result of the formation of a surface depletion layer.

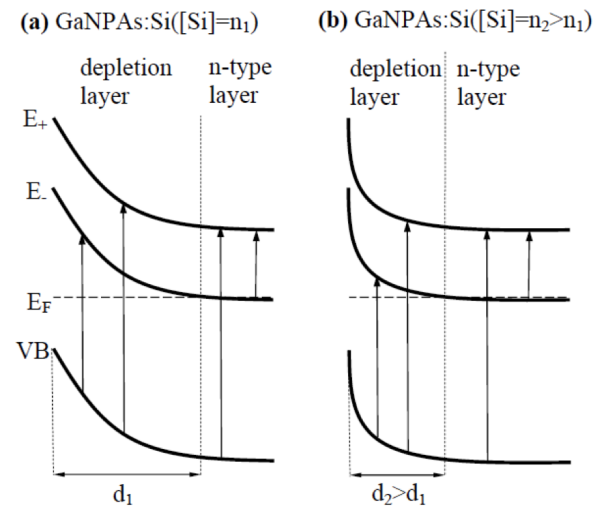


Figure 5.5: Band diagram depicting the change in band bending in (a) Si doped GaNPAs with a dopant concentration of n_1 and a depletion layer width of d_1 , and (b) band-bending for the case of higher dopant concentration n_2 , where $n_2 > n_1$, and the resulting depletion layer width $d_2 < d_1$.

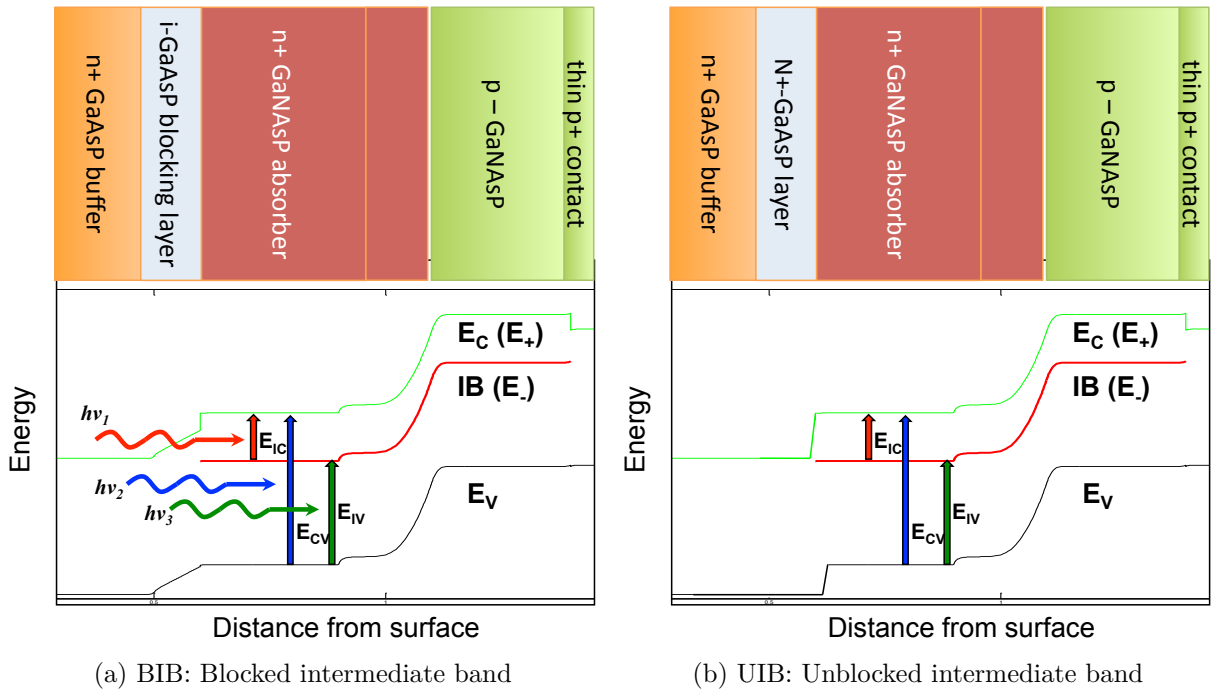


Figure 5.6: Block diagram of IBSC structures with (left) and without (right) an electron blocking layer to electrically isolate the IB.

selective collection of photo-generated carriers from the CB, but not from the IB. Thus, the IB will be coupled to the VB and CB bands through only optical transitions. In practice, this can be done by adding an electron blocking layer (EBL), forming a structure with a blocked intermediate band (BIB). The EBL is simply an energy barrier layer for the IB electrons, located between the IB absorber layer and the n-type contact layer. This can be done by adding a material with a smaller electron affinity χ such that the conduction band edge is closer to the vacuum level (such as the case of AlGaAs in GaAs), and a barrier to electron transport is formed. The structure without the EBL is referred to as the unblocked intermediate band (UIB), and typically serves as a reference structure when attempting to isolate the effect of the IB on PV device performance. In practice, the effect of the IB can be quite small, and thus comparing measurements with and without the EBL allows small changes induced by the IB to be resolved.

One advantage of using n-type substrates for the IBSC devices is that the blocking layer does not need to be optically transparent, as was the case of the ZnTeO IBSC's in ref. [41], where ZnTeO was grown atop p-type ZnTe substrates.

Figure 5.6 shows block diagrams of the designed IBSC both with (left, BIB) and without (right, UIB) a nominally undoped i-GaAsP electron blocking layer.

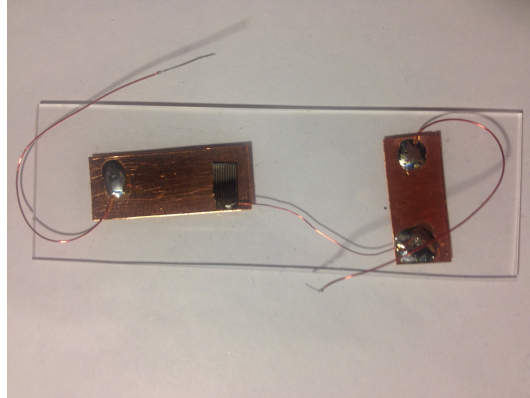


Figure 5.7: The completed GaNAsP IBSC device mounted on a glass slide. The device measures

5.5 Construction of GaNAsP IBSC device

Sample growth was similar to the procedure used during the growth of doped GaNPAs layers described above. Due to lack of a functioning aluminum source on the MBE growth equipment, AlGaAs could not be used as the blocking layer material, and nominally undoped i-GaAsP was used instead. All devices were grown on n-type GaP Substrates ($N=5 \times 10^{17} - 2 \times 10^{18} \text{ cm}^{-3}$). Band diagrams were calculated using the SCAPS computer program[131].

Electrical contacts were fabricated by using e-beam evaporation to deposit 200 \AA of titanium followed by 7000 \AA of gold. A shadow mask was used to pattern the electrical grid. Figure 5.7 shows one of the completed devices. The back contact is soldered with indium to copper tape, and is mounted on a glass slide for stability and support.

5.6 Characterization of IBSC devices

5.6.1 EQE

The external quantum efficiency (EQE) was measured using a 150W xenon lamp modulated with a chopper and a grating monochromator. A 150 W xenon lamp served as the excitation source; the lamp spectrum was removed from the final spectra with a silicon reference diode. The current of the reference diode was measured in the setup while the EQE of the reference diode was provided by the manufacturer for calibration. The light passed through a monochromator with a 600 g/mm grating and 2 mm slit width ($\sim 4 \text{ nm}$ wavelength resolution). Light exiting the monochromator was chopped at 155 Hz and passed through a 578 nm long pass filter at wavelengths greater than 600 nm to eliminate second harmonics from high energy white light. No applied bias was needed since the band bending necessary for charge carrier extraction was provided by the pn junction of

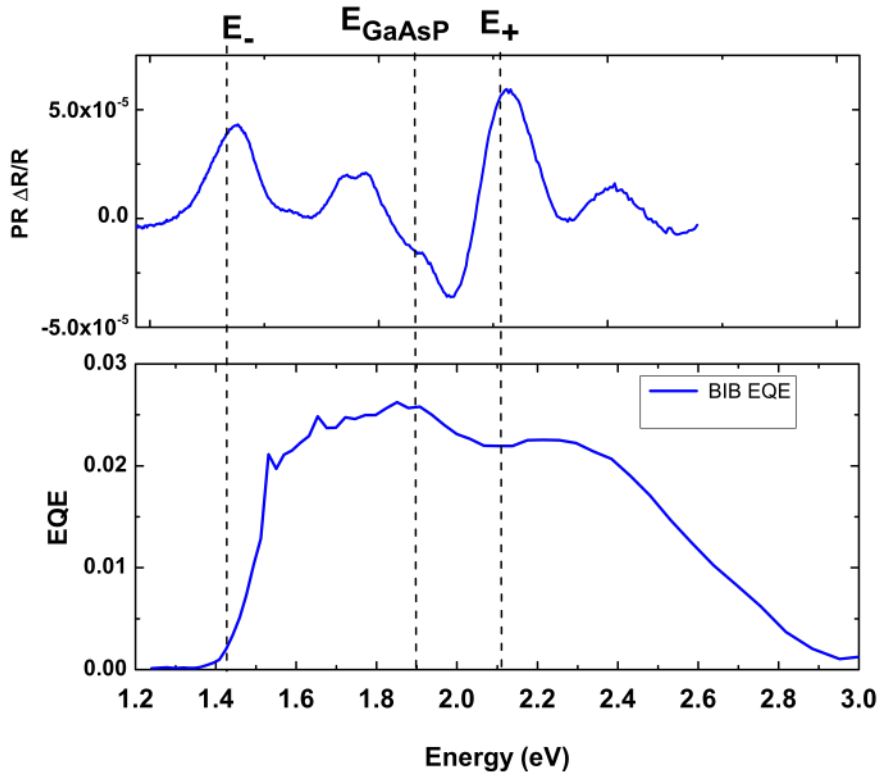


Figure 5.8: Photoreflectance (top) and EQE of Blocked Intermediate Band (BIB) GaNAsP based IBSC.

the devices.

Figure 5.8 shows the measured EQE curve for the GaNPAs BIB solar cell. In the BIB device the photocurrent exhibits two thresholds: the first at about 1.5 eV corresponding to the transitions from $VB \rightarrow E_-$ (IB), and the second at ~ 2.2 eV, corresponding to the transitions from the $VB \rightarrow E_+$ (CB). As seen in the top portion of Figure 5.8, there is an excellent agreement of the EQE onset thresholds with the $VB \rightarrow E_-$ and the $VB \rightarrow E_+$ transitions measured by PR. Furthermore, similar to the case of the GaNAs based IBSC in [28], transitions from the IB to E_+ cannot be resolved.

The observed EQE is consistent with the expected transport behavior of photo-generated charge carriers. In the BIB, the EBL prevents electrons from traveling from the IB layer to the back contact of the solar cell. Thus, under broadband illumination, electrons in the IB can absorb a low energy photon to be excited to the CB, then to be collected at the back contact.

Furthermore, we can explain deviations from an ideal QE response. Below the E_- transition, no light will be absorbed below the so the QE is zero at low energies. At energies greater than E_- and below E_+ , there will be QE losses due to surface recombination, reduced ab-

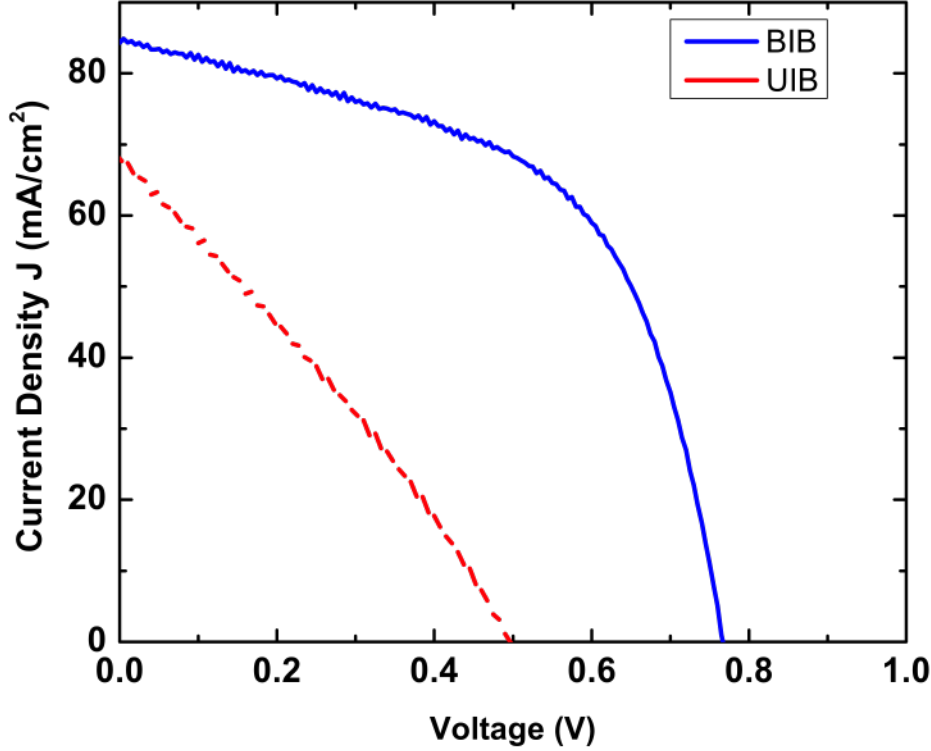


Figure 5.9: J-V curve of Blocked Intermediate Band (BIB) and Unblocked Intermediate Band (UIB) GaNAsP structures.

sorption at long wavelengths (energies just above E_c). Between E_c and E_+ , a reduction of the overall QE occurs, some of which is due to reflection (there is no anti-reflection layer present) and a low diffusion length of minority carriers. Finally, at higher energies above E_+ , the short wavelength response is reduced due to front surface recombination.

5.6.2 JV characteristics

Current voltage (I-V) measurements are used to assess the performance of the solar cell, and can also provide further evidence for the intermediate band activity. Figure 5.9 shows J-V curves for the two types of structures obtained under 20 suns concentration of AM 1.5 illumination. The results are summarized in Table 5.1. The UIB structure shows an open circuit voltage (V_{OC}) of about 0.498 V, whereas the BIB structure has a significantly higher V_{oc} of 0.765 V. In general, the V_{OC} of a PV device depends on the band gap, E_g , and is given by $V_{oc} = (E_g - \Delta)/e$ [28]. The offset depends on the junction and material quality as well as the sunlight concentration factor and has been

Table 5.1: measured IBSC J-V characteristics

	BIB	UIB
V_{OC} (V)	0.765	0.498
J_{SC} (mA/cm ²)	84	69
FF	55.8	29.1

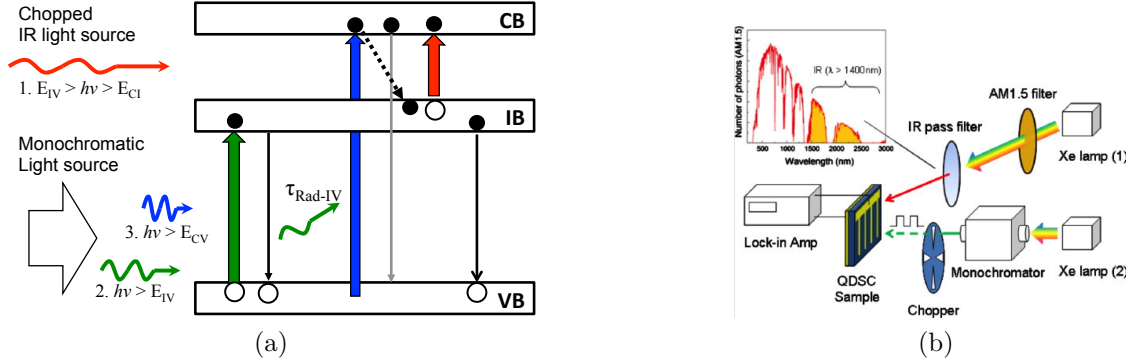


Figure 5.10: 2-photon excitation (TPE) for intermediate band solar cell. (a) Schematic band diagram of 2-photon excitation experiment. (b) Overview of the 2-photon excitation experiment design.

shown to be larger than 0.4 eV under 1 sun illumination [132]. The small V_{OC} and large value of Δ in the UIB structure is consistent with a poor quality junction in this semiconductor. However, there is large increase of V_{OC} in the BIB structure, indicative of voltage enhancement due to IB activity. The large value of the offset found in both cases is most likely related to a short minority carrier lifetime as has been previously found in GaInNAs alloys [133].

5.6.3 Two photon excitation

Photocurrent generation due to 2-photon excitation (TPE) using the IB as stepping stone is an essential step for the realization of viable IBSCs. As covered in Chapter 2, since the ideal IB is electrically isolated, carriers that are excited from VB to IB, could be further excited to the CB with light of energy $h\nu \sim E_{IC}$. Thus, since E_{IC} for this system is approximately 0.6-0.8 eV, illumination with infrared light between 900 and 1700nm would promote carriers from the IB to CB.

Figure 5.10a shows a schematic diagram of the 2-photon experiment, which is similar in concept to the work first reported by ref. [38].

A 940nm LED light source used for the source of IR illumination. The change in quantum efficiency is given by

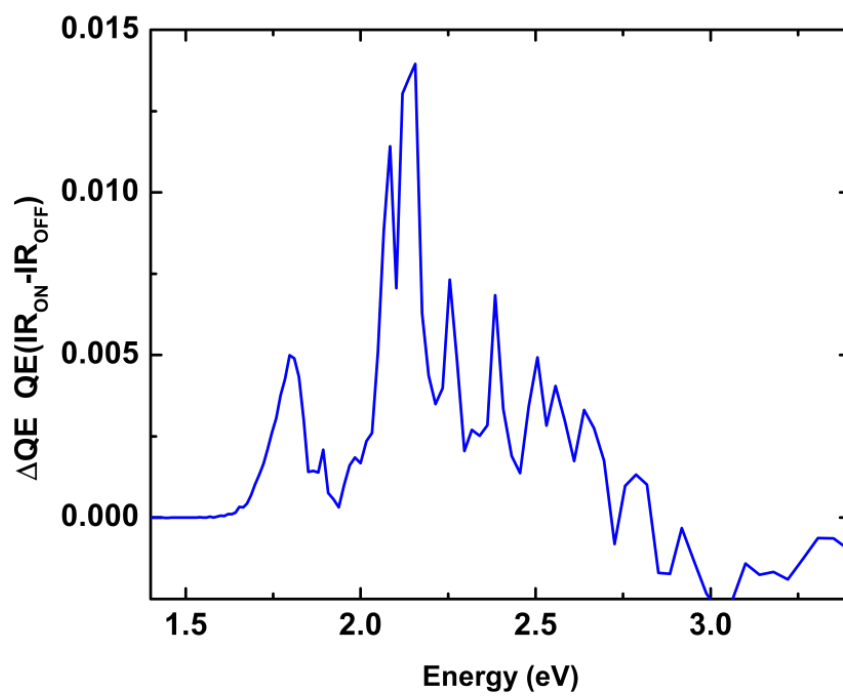


Figure 5.11: Change in quantum efficiency (QE) as result of illumination with IR light source

$$\Delta\text{QE} = \text{QE}_{IR-on} - \text{QE}_{IR-off}. \quad (5.1)$$

Figure 5.11 shows the change in quantum efficiency during the two-photon excitation experiment. As seen from the experiment, enhancement of the quantum efficiency due to IR illumination, which is a key working principle of the IBSC, is observed. However, the effect is small (on the order 1%) and strategies to improve both the material quality and optimize the device architecture are likely to result in further increases to the TPE.

On the experimental side, since the noise level is still high. Strategies to reduce the noise floor include and improve the signal to noise ratio should be explored further. Among these, the temporal stability of the monochromatic light source (halogen lamp) used is quite crucial.

5.7 Conclusion

In order to fabricate a functioning IBSC device, first p-type, and n-type GaNPAs were grown and their optical and electrical properties were characterized. Efficient p and n-type doping of GaNPAs can be achieved with Be and Si, respectively. Next, GaNPAs-based IBSC devices were grown by gas-source molecular beam epitaxy (MBE) on GaP substrates with a thick ($\sim 1.5\mu\text{m}$) compositionally graded GaAsP buffer layers. Both a blocked intermediate band structure, where the intermediate band is electrically isolated from the valence and conduction bands, and an unblocked intermediate band structure (as a reference structure) were grown. The design of the structure was optimized to achieve efficient charge-carrier extraction, yet still demonstrate absorption from the three possible band-to-band transitions. The external quantum efficiency, both with and without a white-light bias, was used to evaluate the spectral response of the devices and the optical activity of the intermediate band. I-V measurements using both AM 1.5 and under 30 suns concentration were used to evaluate the PV device performance.

Chapter 6

Conclusions and future directions

The intermediate band solar cell is an attractive concept to increase photovoltaic conversion efficiency. Compared to a standard single-junction PV, the IBSC is able harness the absorption of sub-bandgap light.

Thus far, an increase in cell efficiency, over the current single-junction case, due to the presence of an intermediate band has not been experimentally demonstrated. This research has extended the current understanding of III-V dilute-nitride alloys, and serves to assess whether these alloys may serve as suitable material systems for intermediate band solar cell applications. Though preliminary, the results are promising enough to suggest that the dilute-nitride alloy GaNPAs could be suitable materials systems. This alloy has strong optical absorption in the desired wavelength range, and its electronic structure is better suited to IBSC application compared to the GaAsN alloy system. 2-photon absorption measurements were used to show absorption between the E_- and E_+ bands. Finally, the GaNPAs alloy can be synthesized using scalable epitaxial techniques and can be doped both n-type and p-type.

The applicability of GaAsPN as an intermediate band solar cell absorber material depends on whether detrimental non-radiative recombination can be kept to a minimum, and whether the absorption of sub-bandgap photons will result in a measurable increase in photocurrent via a 2-step photon absorption process. To test this, a working GaNPAs IBSC device was designed and measured with a solar simulator and the blocked intermediate band cell (the test case) was found to outperform the unblocked intermediate band cell (the reference case). Furthermore, the quantum efficiency was enhanced due to IB activity under illumination with infra-red light .

Following the results of this study, there are several directions in which this research would proceed. The first is to continue the study of p-n junction solar cells with GaAsPN as the absorber material. Continued work is needed to optimize the doping of the GaAsPN absorber layer. Also, a key requirement for a functioning device is to have an effective electrical blocking layer, and both the layer composition and thickness of this layer need to be optimized.

Bibliography

- [1] Matthias Loster. Total Primary Energy Supply - From Sunlight, 2006.
- [2] Martin A Green. Third generation photovoltaics: Ultra-high conversion efficiency at low cost. *Progress in Photovoltaics: Research and Applications*, 9(2):123–135, 2001.
- [3] Steve Byrnes. The Shockley-Queisser limit.
- [4] Antonio Luque and Antonio Martí. Increasing the efficiency of ideal solar cells by photon induced transitions at intermediate levels. *Physical Review Letters*, 78(26):5014, 1997.
- [5] Katsuhisa Yoshida, Yoshitaka Okada, and Nobuyuki Sano. Device simulation of intermediate band solar cells: Effects of doping and concentration. *Journal of applied physics*, 112(8):084510, 2012.
- [6] Stephen P Bremner, Michael Y Levy, and Christiana B Honsberg. Limiting efficiency of an intermediate band solar cell under a terrestrial spectrum. *Applied Physics Letters*, 92(17):171110, 2008.
- [7] P. Bhattacharya, R. Fornari, and H. Kamimura. *Comprehensive Semiconductor Science and Technology, Six-Volume Set: Online version*. Comprehensive semiconductor science and technology. Elsevier Science, 2011.
- [8] W Walukiewicz, J W Ager, III, and Kin Man Yu. Ultrahigh Efficiency Multiband Solar Cells. Technical report, March 2006.
- [9] *World Energy Outlook 2012*. International Energy Agency, November 2012.
- [10] SunShot Vision Study. Technical report, US Department of Energy, February 2012.
- [11] Martin A. Green. *Solar cells: Operating principles, Technology, and System Applications*. Prentice-Hall series in solid state physical electronics. Prentice-Hall, 1982.
- [12] Jenny Nelson. *The physics of solar cells*, volume 57. World Scientific, 2003.

- [13] Uli Würfel Peter Würfel. *Physics of Solar Cells: From Basic Principles to Advanced Concepts*. John Wiley and Sons, 2009.
- [14] William Shockley and Hans J Queisser. Detailed balance limit of efficiency of pn junction solar cells. *Journal of applied physics*, 32(3):510–519, 1961.
- [15] Antonio Luque, Antonio Martí, and Colin Stanley. Understanding intermediate-band solar cells. *Nature Photonics*, 6(3):146–152, February 2012.
- [16] Geoffrey S Kinsey, Peter Hebert, Kent E Barbour, et al. Concentrator multijunction solar cell characteristics under variable intensity and temperature. *Progress in Photovoltaics: Research and Applications*, 16(6):503–508, September 2008.
- [17] Stephen P Bremner and Christiana B Honsberg. Intermediate band solar cell with non-ideal band structure under AM1. 5 spectrum. pages 000021–000024, 2012.
- [18] S P Bremner, M Y Levy, and C B Honsberg. Analysis of tandem solar cell efficiencies under AM1.5G spectrum using a rapid flux calculation method. *Progress in Photovoltaics: Research and Applications*, 16(3):225–233, May 2008.
- [19] Levent Gütay, Alex Redinger, Rabie Djemour, and Susanne Siebentritt. Lone conduction band in $\text{Cu}_2\text{ZnSnSe}_4$. *Applied Physics Letters*, 100(10):102113, 2012.
- [20] K M Yu, W Walukiewicz, J W Ager, et al. Multiband GaNAsP quaternary alloys. *Applied Physics Letters*, 88(9):092110, 2006.
- [21] A Martí, E Antolín, E Cánovas, N López, and P G Linares. Elements of the design and analysis of quantum-dot intermediate band solar cells. *Thin Solid Films*, 2008.
- [22] S A Blokhin, A V Sakharov, A M Nadtochy, et al. AlGaAs/GaAs photovoltaic cells with an array of InGaAs QDs. *Semiconductors*, 43(4):514–518, April 2009.
- [23] Antonio Martí and Antonio Luque. Fundamentals of Intermediate Band Solar Cells. pages 209–228, 2012.
- [24] M Wolf. Limitations and possibilities for improvement of photovoltaic solar energy converters: part I: considerations for earth’s surface operation. *Proceedings of the IRE*, 48(7):1246–1263, 1960.
- [25] N F Mott. Metal-insulator transition. *Reviews of Modern Physics*, 40:677–683, 1968.
- [26] Antonio Luque, Antonio Martí, Elisa Antolín, and César Tablero. Intermediate bands versus levels in non-radiative recombination. *Physica B: Condensed Matter*, 382(1-2):320–327, June 2006.

- [27] Antonio Luque and Antonio Martí. Photovoltaics: Towards the intermediate band. *Nature Photonics*, 5(3):137–138, 2011.
- [28] N López, L A Reichertz, K M Yu, K Campman, and W Walukiewicz. Engineering the electronic band structure for multiband solar cells. *Physical Review Letters*, 106(2):028701, 2011.
- [29] Antonio Martí, E Antolín, P G Linares, and A Luque. Understanding experimental characterization of intermediate band solar cells. *Journal of Materials Chemistry*, 22(43):22832, 2012.
- [30] Inigo Ramiro, Antonio Martí, Elisa Antolín, and Antonio Luque. Review of Experimental Results Related to the Operation of Intermediate Band Solar Cells. *IEEE Journal of Photovoltaics*, 4(2):736–748, March 2014.
- [31] A Luque, P G Linares, E Antolín, et al. Understanding the operation of quantum dot intermediate band solar cells. *Journal of applied physics*, 111(4):044502, 2012.
- [32] Yoshitaka Okada, Takayuki Morioka, Katsuhisa Yoshida, et al. Increase in photocurrent by optical transitions via intermediate quantum states in direct-doped InAs/GaNAs strain-compensated quantum dot solar cell. *Journal of applied physics*, 109(2):024301, 2011.
- [33] C Tablero. Analysis of the electronic properties of intermediate band materials as a function of impurity concentration. *Physical Review B*, 72(3):035213, July 2005.
- [34] Pablo Palacios, Perla Wahnón, Sara Pizzinato, and José C Conesa. Energetics of formation of TiGa_3As_4 and TiGa_3P_4 intermediate band materials. *The Journal of Chemical Physics*, 124(1):014711, 2006.
- [35] C Tablero and D Fuertes Marrón. Analysis of the Electronic Structure of Modified CuGaS_2 with Selected Substitutional Impurities: Prospects for Intermediate-Band Thin-Film Solar Cells Based on Cu-Containing Chalcopyrites. *The Journal of Physical Chemistry C*, 114(6):2756–2763, February 2010.
- [36] Miaomiao Han, Xiaoli Zhang, and Z Zeng. RSC Advances. *RSC Advances*, 4:62380–62386, November 2014.
- [37] Yohanna Seminovski, Pablo Palacios, and Perla Wahnón. Analysis of SnS_2 hyperdoped with V proposed as efficient absorber material. *Journal of Physics: Condensed Matter*, 26(39):395501, September 2014.
- [38] Nazmul Ahsan, Naoya Miyashita, Muhammad Monirul Islam, et al. Two-photon excitation in an intermediate band solar cell structure. *Applied Physics Letters*, 100(17):172111, 2012.

- [39] K Yu, W Walukiewicz, J Wu, et al. Diluted II-VI Oxide Semiconductors with Multiple Band Gaps. *Physical Review Letters*, 91(24):246403, December 2003.
- [40] Generation and recombination rates at ZnTe:O intermediate band states. *Applied Physics Letters*, 95(26):261107, December 2009.
- [41] Tooru Tanaka, Masaki Miyabara, Yasuhiro Nagao, et al. Photocurrent induced by two-photon excitation in ZnTeO intermediate band solar cells. *Applied Physics Letters*, 102(5):052111, February 2013.
- [42] W Shan, W Walukiewicz, J W Ager, III, et al. Band anticrossing in GaInNAs alloys. *Physical Review Letters*, 82(6):1221, 1999.
- [43] W Shan, W Walukiewicz, K M Yu, et al. Effect of nitrogen on the electronic band structure of group III-NV alloys. *Physical Review B*, 62(7):4211, 2000.
- [44] J Wu, W Walukiewicz, K Yu, et al. Band anticrossing in GaP_{1-x}N_x alloys. *Physical Review B*, 65(24):241303, May 2002.
- [45] W Walukiewicz, W Shan, K M Yu, et al. Interaction of localized electronic states with the conduction band: Band anticrossing in II-VI semiconductor ternaries. *Physical Review Letters*, 85(7):1552, 2000.
- [46] W Shan, K M Yu, W Walukiewicz, et al. Band anticrossing in dilute nitrides. *Journal of Physics: Condensed Matter*, 16(31):S3355, 2004.
- [47] Tooru Tanaka, Kin M Yu, Alejandro X Levander, et al. Demonstration of ZnTeO Intermediate Band Solar Cell. *Japanese Journal of Applied Physics*, 50(8):082304, August 2011.
- [48] J C Harmand, G Ungaro, L Largeau, and G Le Roux. Comparison of nitrogen incorporation in molecular-beam epitaxy of GaAsN, GaInAsN, and GaAsSbN. *Applied Physics Letters*, 77(16):2482–2484, 2000.
- [49] J Wu, W Walukiewicz, and E Haller. Band structure of highly mismatched semiconductor alloys: Coherent potential approximation. *Physical Review B*, 65(23):233210, June 2002.
- [50] P R C Kent and Alex Zunger. Theory of electronic structure evolution in GaAsN and GaPN alloys. *Physical Review B*, 64(11):115208, August 2001.
- [51] F Koch, R Mitdank, G Oelgart, and C Chlupsa. Excess carrier recombination in indirect gap GaAsP: N. *physica status solidi (a)*, 110(1):197–204, 1988.
- [52] R Mickevicius and A Reklaitis. Electron intervalley scattering in gallium arsenide. *Semiconductor Science and Technology*, 5(8):805, 1990.

- [53] J A Kash. Exciton tunneling inhibited by disorder in GaAsP: N. *Physical Review B*, 29(12):7069, 1984.
- [54] Shuit-Tong Lee Kui-Qing Peng. Silicon Nanowires for Photovoltaic Solar Energy Conversion. *Advanced Materials*, XX:1–18, 2010.
- [55] H. Park Y. Cui, Q. Wei and C. Lieber. Nanowire nanosensors for highly sensitive and selective detection of biological and... *Science*, January 2001.
- [56] Y. Cui W. Wang G. Zheng, F. Patolsky and C. Lieber. Multiplexed electrical detection of cancer markers with nanowire sensor arrays. *Nature Biotechnology*, 23:1294–1301, January 2005.
- [57] G. Cheng A. Kolmakov, Y. Zhang and M. Moskovits. Detection of co and o-2 using tin oxide nanowire sensors. *Advanced Materials*, 15:997, January 2003.
- [58] Cesare Soci Yong Ding Zhong-Lin Wang Wei Wei, Xin-Yu Bao and Deli Wang. Direct Heteroepitaxy of Vertical InAs Nanowires on Si Substrates for Broad Band Photovoltaics and Photodetection. *Nano Letters*, 9(8):2926–2934, 2009.
- [59] E. M. Arakcheeva E. M. Tanklevskaya P. Werner Yu. B. Samsonenko, V. G. Dubrovskii. Photovoltaic Properties of p-Doped GaAs Nanowire Arrays Grown on n-Type GaAs(111)B Substrate. *Nanoscale Research Letters*, 5:360–363, 2010.
- [60] Yi Cui Erik C. Garnett, Mark L. Brongersma and Michael D. McGehee. Nanowire Solar Cells. *Annu. Rev. Mater. Res.*, 41:269–95, 2011.
- [61] Z. Mi and Y.-L. Chang. III-V compound semiconductor nanostructures on silicon: Epitaxial growth, properties, and applications in light emitting diodes and lasers. *Journal of Nanophotonics*, 3(031602), January 2009.
- [62] Devesh Khanal. *Advanced Electrical Characterization of Semiconductor Nanowires*. PhD thesis, University of California, Berkeley, 2010.
- [63] J. A. Petykiewicz D. B. Turner-Evans M. C. Putnam E. L. Warren J. M. Spurgeon R. M. Briggs N. S. Lewis H. A. Atwater M. D. Kelzenberg, S. W. Boettcher. *Nature Materials*, 9(239), 2010.
- [64] Ruoxue Yan Peidong Yang and Melissa Fardy. Semiconductor Nanowire: What's Next? *Nano Letters*, 10:529–1536, 2010.
- [65] C. P. T.; Wacaser B. A.; Larsson M. W.; Seifert W.; Deppert K.; Gustafsson A.; Wallenberg L. R.; Samuelson L Martensson, T.; Svensson. *Nano Letters*, 4:1987, 2004.

- [66] M. T.; Verheijen M. A. Bakkers, E. P. A. M.; Borgstrom. *MRS Bulletin*, 32:117, 2007.
- [67] Ujjal K. Gautam Tianyou Zhai Silvija Gradecak Xiaosheng Fang, Yoshio Bando and Dmitri Golberg. Heterostructures and superlattices in one-dimensional nanoscale semiconductors. *Journal of Materials Chemistry*, 19:5683–5689, 2009.
- [68] Yiyang Wu and Peidong Yang. Direct Observation of Vapor Liquid Solid Nanowire Growth. *Journal of the American Chemical Society*, 123(13):3165–3166, April 2001.
- [69] Joan M Redwing, Xin Miao, and Xiuling Li. *Vapor-Liquid-Solid Growth of Semiconductor Nanowires*. Elsevier B.V., second edition edition, October 2014.
- [70] D Spirkoska, G Abstreiter, and A Morral. GaAs nanowires and related prismatic heterostructures. *Semiconductor Science and Technology*, 24:113001, 2009.
- [71] J H Paek, T Nishiwaki, M Yamaguchi, and N Sawaki. Catalyst free MBE-VLS growth of GaAs nanowires on (111) Si substrate. *physica status solidi (c)*, 6(6):1436–1440, June 2009.
- [72] JH Paek, T Nishiwaki, M Yamaguchi, and N Sawaki. Structural and optical properties of a catalyst-free GaAs/AlGaAs core-shell nano/microwire grown on (1 1 1) Si substrate. *Physica E: Low-dimensional Systems and Nanostructures*, 2010.
- [73] Joanne W L Yim, Costas P Grigoropoulos, and Junqiao Wu. Mismatched alloy nanowires for electronic structure tuning. *Applied Physics Letters*, 99(23):233111, 2011.
- [74] Supanee Sukrittanon, YanJin Kuang, and Charles W Tu. Growth and characterization of GaP/GaNP core/shell nanowires. *Journal of Vacuum Science & Technology B: Microelectronics and Nanometer Structures*, 31(3):03C110, 2013.
- [75] Y J Kuang, S Sukrittanon, H Li, and C W Tu. Growth and photoluminescence of self-catalyzed GaP/GaNP core/shell nanowires on Si (111) by gas source molecular beam epitaxy. *Applied Physics Letters*, 100(5):053108, 2012.
- [76] Yoshiaki Araki, Masahito Yamaguchi, and Fumitaro Ishikawa. Growth of dilute nitride GaAsN/GaAs heterostructure nanowires on Si substrates. *Nanotechnology*, 24(6):065601, January 2013.
- [77] I Ho and G B Stringfellow. Solubility of nitrogen in binary III–V systems. *Journal of Crystal Growth*, 1997.
- [78] André Anders and Michael Kühn. Characterization of a low-energy constricted-plasma source. *Review of Scientific Instruments*, 69(3):1340, 1998.

- [79] A Zhukov, R Zhao, P Specht, et al. MBE growth of (In) GaAsN on GaAs using a constricted DC plasma source. *Semiconductor Science and Technology*, 2001.
- [80] A R Kovsh, J S Wang, L Wei, et al. Molecular beam epitaxy growth of GaAsN layers with high luminescence efficiency. *Journal of Vacuum Science & Technology B: Microelectronics and Nanometer Structures*, 20(3):1158, 2002.
- [81] A E Zhukov, E S Semenova, V M Ustinov, and E R Weber. GaAsN-on-GaAs MBE using a DC plasma source. *Technical Physics*, 46(10):1265–1269, 2001.
- [82] V Dubrovskii, G Cirlin, I Soshnikov, et al. Diffusion-induced growth of GaAs nanowhiskers during molecular beam epitaxy: Theory and experiment. *Physical Review B*, 71(20):205325, May 2005.
- [83] Soo-Ghang Ihn, Jong-In Song, Tae-Wook Kim, et al. Morphology- and Orientation-Controlled Gallium Arsenide Nanowires on Silicon Substrates. *Nano Letters*, 7(1):39–44, January 2007.
- [84] Jason Grebenkemper. Powder X-ray Diffraction.
- [85] Wei Li, Markus Pessa, and Jari Likonen. Lattice parameter in GaNAs epilayers on GaAs: Deviation from Vegard’s law. *Applied Physics Letters*, 78(19):2864, 2001.
- [86] T Schmidt, K Lischka, and W ZULEHNER. Excitation-Power Dependence of the Near-Band-Edge Photoluminescence of Semiconductors. *Physical Review B*, 45(16):8989–8994, 1992.
- [87] Robert Kudrawiec, Grzegorz Sęk, Jan Misiewicz, et al. Localized and delocalized states in GaNAs studied by microphotoluminescence and photoreflectance. *Applied Physics Letters*, 94(1):011907, 2009.
- [88] L V Titova, Thang B Hoang, H E Jackson, et al. Temperature dependence of photoluminescence from single core-shell GaAs–AlGaAs nanowires. *Applied Physics Letters*, 89(17):173126–173126–3, 2006.
- [89] S B Nam, D C Reynolds, C W Litton, et al. Free-exciton energy spectrum in GaAs. *Physical Review B*, 13(2):761, 1976.
- [90] B V Novikov, S Yu Serov, N G Filosofov, et al. Photoluminescence properties of GaAs nanowire ensembles with zincblende and wurtzite crystal structure. *physica status solidi (RRL) - Rapid Research Letters*, 4(7):175–177, June 2010.
- [91] D. Spirkoska, J. Arbiol, A. Gustafsson, et al. Structural and optical properties of high quality zinc-blende/wurtzite GaAs nanowire heterostructures. *Phys. Rev. B*, 80:245325, Dec 2009.

- [92] U Jahn, J Lähnemann, C Pfüller, O Brandt, and S Breuer. Phys. Rev. B 85, 045323 (2012) - Luminescence of GaAs nanowires consisting of wurtzite and zinc-blende segments. *Physical Review B*, 2012.
- [93] Philippe Caroff, Jessica Bolinsson, and J Johansson. Crystal Phases in III–V Nanowires: From Random Toward Engineered Polytypism. *Selected Topics in Quantum Electronics, IEEE Journal of*, 17(4):829–846, 2011.
- [94] J S Wang, A R Kovsh, L Wei, et al. MBE growth of high-quality GaAsN bulk layers. *Nanotechnology*, 12(4):430, 2001.
- [95] Anders Mikkelsen, Niklas Sköld, Lassana Ouattara, et al. Direct imaging of the atomic structure inside a nanowire by scanning tunnelling microscopy. *Nature Materials*, 3(8):519–523, July 2004.
- [96] Brent A Wacaser, Knut Deppert, Lisa S Karlsson, Lars Samuelson, and Werner Seifert. Growth and characterization of defect free GaAs nanowires. *Journal of Crystal Growth*, 287(2):504–508, January 2006.
- [97] CaroffP., DickK. A., JohanssonJ., et al. Controlled polytypic and twin-plane superlattices in iii-v nanowires. *Nat Nano*, 4(1):50–55, 01 2009.
- [98] D E Aspnes. Third-Derivative Modulation Spectroscopy with Low-Field Electroreflectance. *Surface Science*, 37(1):418–442, 1973.
- [99] J Misiewicz, P Sitarek, and G Sek. Photorefectance spectroscopy of low-dimensional semiconductor structures. *Opto-Electronics Review*, 8(1):1–24, March 2000.
- [100] Y S Tang. Photorefectance line shapes of semiconductor microstructures. *Journal of applied physics*, 69(12):8298, 1991.
- [101] J Misiewicz, Piotr Sitarek, G Sek, and Robert Kudrawiec. Semiconductor heterostructures and device structures investigated by photorefectance spectroscopy. *Materials Science*, 21(3):263–318, 2003.
- [102] Sandip Ghosh and H T Grahn. Photorefectance line shape of excitonic transitions analyzed with a redefined set of fitting parameters. *Journal of applied physics*, 90(1):500–502, 2001.
- [103] M A Pinault and E Tournié. Influence of alloy stability on the photoluminescence properties of GaAsN/GaAs quantum wells grown by molecular beam epitaxy. *Applied Physics Letters*, 79(21):3404, 2001.
- [104] A Lindsay and E P O’Reilly. Phys. Rev. Lett. 93, 196402 (2004) - Unification of the Band Anticrossing and Cluster-State Models of Dilute Nitride Semiconductor Alloys. *Physical Review Letters*, 2004.

- [105] T Mattila, Su-Huai Wei, and Alex Zunger. Localization and anticrossing of electron levels in GaAs $1-x$ N x alloys. *Physical Review B*, 60(16):R11245, 1999.
- [106] P R C Kent, L Bellaiche, and Alex Zunger. Pseudopotential theory of dilute III V nitrides. *Semiconductor Science and Technology*, 17(8):851–859, July 2002.
- [107] J Wu, W Shan, and W Walukiewicz. Band anticrossing in highly mismatched III V semiconductor alloys. *Semiconductor Science and Technology*, 17(8):860–869, July 2002.
- [108] A Lindsay and E P O’Reilly. Theory of enhanced bandgap non-parabolicity in GaNAs and related alloys. *Solid State Communications*, 1999.
- [109] C Skierbiszewski, P Perlin, P Wisniewski, et al. Large, nitrogen-induced increase of the electron effective mass in InGaNaNs. *Applied Physics Letters*, 76(17):2409–2411, 2000.
- [110] M Güngerich, P J Klar, W Heimbrod, et al. Comparison of the Electronic Band Formation and Band Structure of GaNaNs and GaNP. In *Dilute III-V Nitride . . .*, pages 343–367. Springer Berlin Heidelberg, Berlin, Heidelberg, 2008.
- [111] W Shan, W Walukiewicz, K M Yu, et al. Band Anticrossing in III-N-V Alloys. *physica status solidi (b)*, 223(1):75–85, January 2001.
- [112] Stanko Tomic, Eoin P O’Reilly, Robin Fehse, et al. Theoretical and experimental analysis of 1.3- μ m InGaAsN/GaAs lasers. *Selected Topics in Quantum Electronics, IEEE Journal of*, 9(5):1228–1238, 2003.
- [113] M Gladysiewicz, R Kudrawiec, J M Miloszewski, et al. Band structure and the optical gain of GaInNaNs/GaAs quantum wells modeled within 10-band and 8-band kp model. *Journal of applied physics*, 113(6):063514, 2013.
- [114] Philip W Anderson. Absence of diffusion in certain random lattices. *Physical review*, 109(5):1492, 1958.
- [115] A Mascarenhas, M J Seong, S Yoon, and J C Verley. Phys. Rev. B 68, 233201 (2003) - Evolution of electronic states in GaAsN probed by resonant Raman spectroscopy. *Physical Review B*, 2003.
- [116] J Perkins, A Mascarenhas, J Geisz, and D Friedman. Conduction-band-resonant nitrogen-induced levels in GaAs $1-x$ N x with $x < 0.03$. *Physical Review B*, 64(12):121301, September 2001.
- [117] Junqiao Wu. *Band Anticrossing Effects in Highly Mismatched Semiconductor Alloys*. PhD thesis, University of California, Berkeley, Applied Science and Technology, 2002.

- [118] K.M.L. Alberi and Berkeley University of California. *Valence Band Anticrossing in Highly Mismatched Alloys*. University of California, Berkeley, 2008.
- [119] I Vurgaftman, J R Meyer, and L R Ram-Mohan. Band parameters for III–V compound semiconductors and their alloys. *Journal of applied physics*, 89(11):5815, 2001.
- [120] M. Mayer. SIMNRA, a simulation program for the analysis of NRA, RBS and ERDA. In *American Institute of Physics Conference Series*, volume 475 of *American Institute of Physics Conference Series*, pages 541–544, June 1999.
- [121] G. Terwagne J.L. Colaux, I. Derycke. SIMTarget.
- [122] Yan-Jin Kuang, San-Wen Chen, Hua Li, Sunil K Sinha, and Charles Wuching Tu. Growth of GaNAsP alloys on GaP(100) by gas-source molecular beam epitaxy. *Journal of Vacuum Science & Technology B: Microelectronics and Nanometer Structures*, 30(2):02B121, 2012.
- [123] Y J Kuang, K M Yu, R Kudrawiec, et al. GaNAsP: An intermediate band semiconductor grown by gas-source molecular beam epitaxy. *Applied Physics Letters*, 102(11):112105–112105, 2013.
- [124] M Izadifard, J P Bergman, I Vorona, et al. Evaluation of optical quality and defect properties of GaNP alloys lattice matched to Si. *Applied Physics Letters*, 85(26):6347, 2004.
- [125] S Almosni, C Robert, T Nguyen Thanh, et al. Evaluation of InGaPN and GaAsPN materials lattice matched to Si for multijunction solar cells. *Journal of applied physics*, 113(12):123509, 2013.
- [126] T Nguyen Thanh, C Robert, W Guo, et al. Structural and optical analyses of GaP/Si and (GaAsPN/GaPN)/GaP/Si nanolayers for integrated photonics on silicon. *Journal of applied physics*, 112(5):053521, September 2012.
- [127] I A Buyanova, G Yu Rudko, W M Chen, H P Xin, and C W Tu. Radiative recombination mechanism in GaNP alloys. *Applied Physics Letters*, 80(10):1740, 2002.
- [128] Yanjin Kuang. *Molecular Beam Epitaxy of Dilute Nitride GaNAsP as Intermediate Band Solar Cell Materials*. PhD thesis, University of California, San Diego, 2014.
- [129] Rune Strandberg and Turid Worren Reenaas. Photofilling of intermediate bands. *Journal of applied physics*, 105(12):124512, 2009.
- [130] K M Yu, W Walukiewicz, J Wu, et al. Mutual passivation of electrically active and isovalent impurities. *Nature Materials*, 1(3):185–189, October 2002.

- [131] M Burgelman, P Nollet, and S Degrave. Modelling polycrystalline semiconductor solar cells. *Thin Solid Films*, 2000.
- [132] R R King, D C Law, K M Edmondson, et al. 40cells. *Applied Physics Letters*, 90(18):183516, 2007.
- [133] D J Friedman, J F Geisz, S R Kurtz, and J M Olson. 1-eV solar cells with GaInNAs active layer. *Journal of Crystal Growth*, 1998.
- [134] Sang-Gil Ryu, Eunpa Kim, Jae-hyuck Yoo, et al. On Demand Shape-Selective Integration of Individual Vertical Germanium Nanowires on a Si(111) Substrate via Laser-Localized Heating. *ACS Nano*, 7(3):2090–2098, March 2013.
- [135] Sang-Gil Ryu, Ivan Gruber, Costas P Grigoropoulos, Dimos Poulikakos, and Seung-Jae Moon. Thin Solid Films. *Thin Solid Films*, 520(22):6724–6729, September 2012.
- [136] Hannah J Joyce, Qiang Gao, H Hoe Tan, et al. High Purity GaAs Nanowires Free of Planar Defects: Growth and Characterization. *Advanced Functional Materials*, 18(23):3794–3800, December 2008.
- [137] Xiangfeng Duan, Jianfang Wang, and Charles M Lieber. Synthesis and optical properties of gallium arsenide nanowires. *Applied Physics Letters*, 76(9):1116–1118, 2000.
- [138] G E Cirlin, V G Dubrovskii, Yu B Samsonenko, et al. Self-catalyzed, pure zincblende GaAs nanowires grown on Si (111) by molecular beam epitaxy. *Physical Review B*, 82(3):035302, 2010.
- [139] Emanuele Uccelli, Jordi Arbiol, Cesar Magen, et al. Three-dimensional multiple-order twinning of self-catalyzed GaAs nanowires on Si substrates. *Nano Letters*, 11(9):3827–3832, 2011.
- [140] Akio Suzuki, Atsuhiko Fukuyama, Hidetoshi Suzuki, et al. Optical properties of Be-doped GaAs nanowires on Si substrate grown by a catalyst-free molecular beam epitaxy vapor-liquid-solid method. *Japanese Journal of Applied Physics*, 53(5S1):05FV03, April 2014.

Appendix A

Additional data and figures

A.1 Selected Properties of III-V Semiconductors

Property / Material	GaAs	Cubic (Beta) GaN	Hexagonal (Alpha) GaN	GaP	Si
Structure	zinc blende	zinc blende	wurtzite	zinc blende	Diamond cubic
Lattice Parameter at 300K (Å)	5.65	4.50	$a_0 = 3.819$; $c_0 = 5.185$	5.45	5.43
High-Frequency Dielectric Constant		2.9 (at 3eV)	2.67 (at 3.38eV)	9.11	
Static Dielectric Constant				11.1	
Nature of Energy Gap E_g	direct	direct	direct	indirect	indirect
Energy Gap E_g at 300K (eV)		3.23*	3.45	2.72	1.12
Effective mass of electrons m_e^* / m_0			0.22		
Effective mass of electrons m_t^* / m_0				1.12	
Effective mass of electrons m_t^* / m_0				0.22	
Effective mass of holes m_h^* / m_0	0.50			0.79	
Effective mass of holes m_{tp}^* / m_0				0.14	
Electron mobility at 300K ($\text{cm}^2\text{V}^{-1}\text{s}^{-1}$)	8500		500*	250	1400
Hole mobility ($\text{cm}^2\text{V}^{-1}\text{s}^{-1}$)	400			150	

Sources: <http://www.ioffe.ru/SVA/NSM/Semicond/>
<http://www.semiconductors.co.uk/propiiv5653.htm>
<http://www.iue.tuwien.ac.at/phd/palankovski/node40.html>

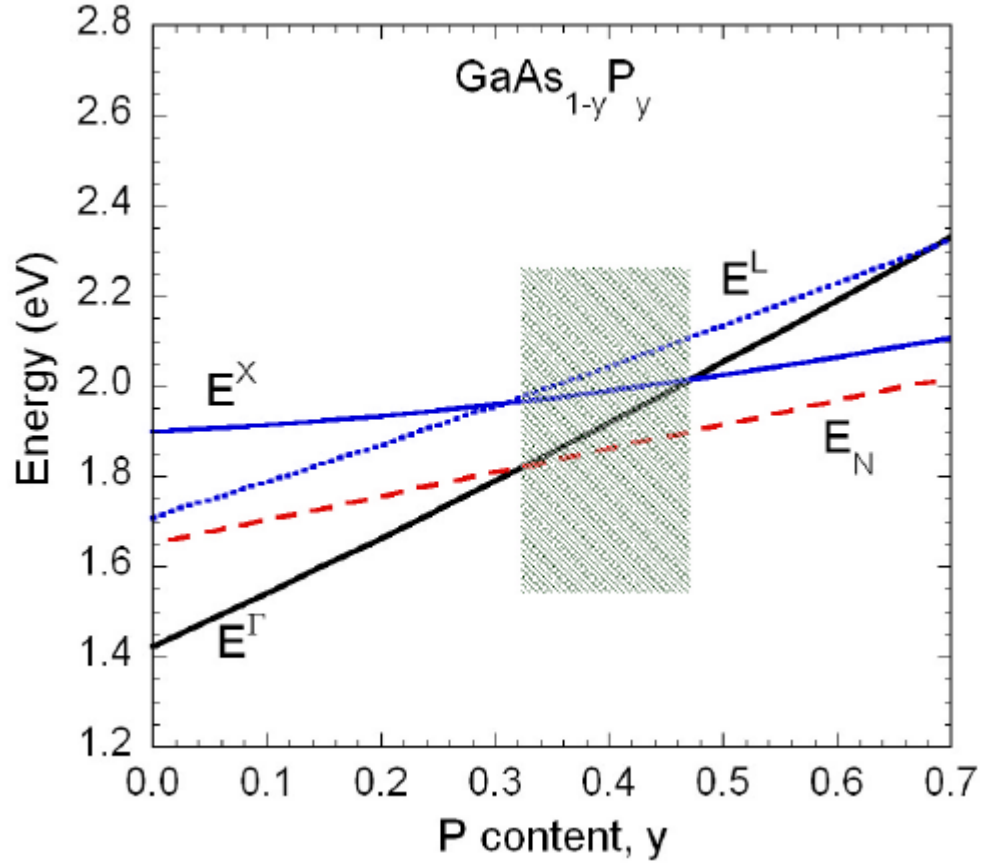
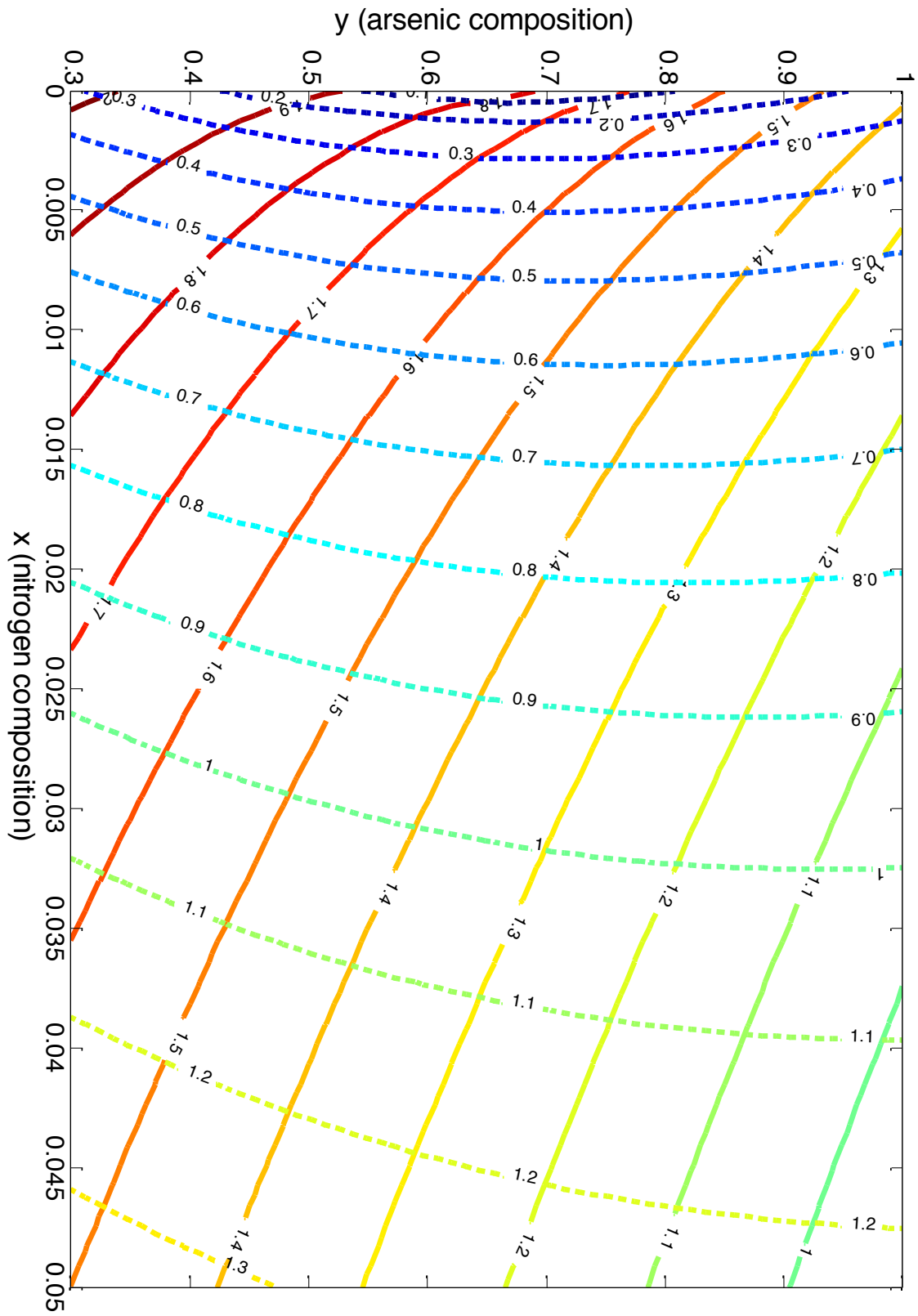


Figure A.1: Calculated energy positions of the N level and the Γ , X, and L conduction bands of the GaAs_{1-y}P_y alloy system. At a P content y of > 0.3 the local N level E_N drops below the conduction band E^Γ , creating the conditions required to make a multiband semiconductor. An upper limit to the P content is set by the appearance of an indirect band gap ($E^X < E^\Gamma$) at $y > 0.5$. Figure from [8].

A.2 GaN_xP_{1-x-y}As_y



A.3 k.p calculation of GaNPAs bandstructure

We start with the solution of schrodinger equation for periodic lattice:

$$\psi(\mathbf{k}, \mathbf{r}) = \exp(i\mathbf{k} \cdot \mathbf{r})u(\mathbf{k}, \mathbf{r})$$

If $V=0$, solutions are of the form:

$$\psi(k, r) = 1/\sqrt{\Omega} \exp(iK \cdot r), \psi(k, r) = \exp(ik \cdot r) \sqrt{\Omega} \exp(iG \cdot r),$$

and $G \cdot R = 2\pi m$

In addition to the band anticrossing model, the band structure of III-V-N alloys can be calculated within 10-band kp approximation. The 10-band kp Hamiltonian for unstrained GaNPAs is given by [112, 113]

$$\hat{\mathcal{H}} = \begin{pmatrix} E_N & V_{NC} & 0 & 0 & 0 & 0 & 0 & 0 & 0 & 0 \\ & E_{CB} & -\sqrt{3}T_+ & \sqrt{2}U & -U & 0 & 0 & 0 & -T_- & -\sqrt{2}T_- \\ & & E_{HH} & \sqrt{2}S & -S & 0 & 0 & 0 & -R & -\sqrt{2}R \\ & & & E_{LH} & Q & 0 & T_+^* & R & 0 & -\sqrt{3}S \\ & & & & E_{SO} & 0 & \sqrt{2}T_+^* & \sqrt{2}R & -\sqrt{3}S & 0 \\ & & & & & E_N & V_{NC} & 0 & 0 & 0 \\ & & & & & & E_{CB} & -\sqrt{3}T_- & -\sqrt{2}U & -U \\ & & & & & & & E_{HH} & \sqrt{2}S^* & -S^* \\ & & & & & & & & E_{LH} & Q \\ & & & & & & & & & E_{SO} \end{pmatrix}$$

The matrix elements are the same as in the conventional 8-band kp Hamiltonian, where the subscripts CB, HH, LH, and SO mean the conduction, heavy-hole, light-hole, and spin-off bands, respectively. The energy scale is assumed such that at the Γ point $E_{HH}(k=0) = E_{LH}(k=0) = 0$, $E_{SO}(k=0) = \Delta_{SO}$, and $E_{CB}(k=0) = E_g = E_g^{GaPAs}$, where Δ_{SO} and E_g^{GaPAs} is, respectively, the spin-orbit splitting and the energy gap for GaPAs. m_0 is the electron mass, \hbar is the plank constant divided by 2π , and $k_{\parallel}^2 = k_x^2 + k_y^2$. P is the Kane matrix element defined as $P = -i\hbar/m_0 s' |p_v\rangle |v\rangle$, where $|s'\rangle$ indicates a CB Bloch state of s-like symmetry and $|v\rangle$ is a valence band p state with character $|v\rangle = |x\rangle$, $|y\rangle$, or $|z\rangle$. Since the conduction band is treated exactly in this Hamiltonian, the Luttinger parameters are modified, i.e. the parameters $\gamma_{1,2,3}$ in the matrix elements are replaced by $\gamma_1 \rightarrow \gamma_1 - E_P/(3E_g)$ and $\gamma_{2,3} \rightarrow \gamma_{2,3} - E_P/(6E_g)$, where $E_P = 2m_0P/\hbar^2$ is the Kane matrix element expressed in energy units and E_g is the bandgap of the host material. The term $s_C = 1/(m_c^*) - (E_P/3)[2/E_g + 1/(E_g + \Delta_{SO})]$ replaces $1/m_c^*$ and is associated with the conduction band nonparabolicity of the host material. According to the BAC model it is assumed that the matrix elements describing interaction between the nitrogen level and the valence band (heavy-hole, light-hole and spin-orbit band) are zero. Material parameters for these calculations were taken from Ref. [28].

Appendix B

Growth of GaAs nanowires on patterned silicon substrates

B.1 Background

The application of reduced temperature, laser-based processing of semiconductor materials may eliminate the need for lithographic processes and opens the way to the fabrication of high-resolution, all-printed electronic devices on a range of substrates. This laser processing technique could be used for selective-area growth and deposition of III-V materials and nanostructures on silicon, which is of considerable interest within both the research and industry communities. Related works have even demonstrated the suitability of this technique to integrate single vertical Ge nanowires on silicon, with on-demand shape selectivity[134]. The goal of the ensuing research is to study the growth of III-V nanostructures, namely GaAs self-catalyzed nanowires, on a laser-patterned silicon (111) substrate.

B.2 Femto-second laser patterning of silicon (111)

Details of the experimental setup can be found in Ref. [135]. For this work, a lower bound on dot size of 273nm at 1.5nJ of pulse energy was selected. In total, a parameter space encompassing 40 different conditions through a combination of dot pitch (5 cases) and laser pulse energy (8 cases) was studied, requiring a total of 6 hours of patterning time. Initially, dot pitch and size was verified by AFM, though for smaller dot pitches, on the order of 0.5 μ m or less, SEM images were used to confirm the dot pitch. Figure B.1 shows an overview of the patterning conditions and dot-pitch used. During the MBE growth, the standard GaAs nanowire deposition recipe was followed, as detailed in Chapter 4. A gallium BEP of 3.3×10^{-7} and an arsenic BEP of 1.0×10^{-5} were used, along with a substrate temperature of 580°C and a growth time of 10 minutes.

B.3 Results

Figure B.3 shows an SEM image of a region with dot diameter of approximately 1.1 μ m both before and after the GaAs deposition. GaAs nanowires can be seen protruding from the dots. Based on the SEM images, the nanowires are approximately 5-6 μ m in length, and 50-80 nm diameter, on the same order as the wires grown during the self-catalyzed GaAs NW growth on clean pristine Si (111) substrates, detailed in Chapter 3.

Figure B.6 shows an EDX linescan of the region after growth, confirming the deposited material is gallium arsenide. Though not shown, an EDX mapping procedure was used to perform an area scan and verify that GaAs was deposited nearly exclusively over the laser-etched dots.

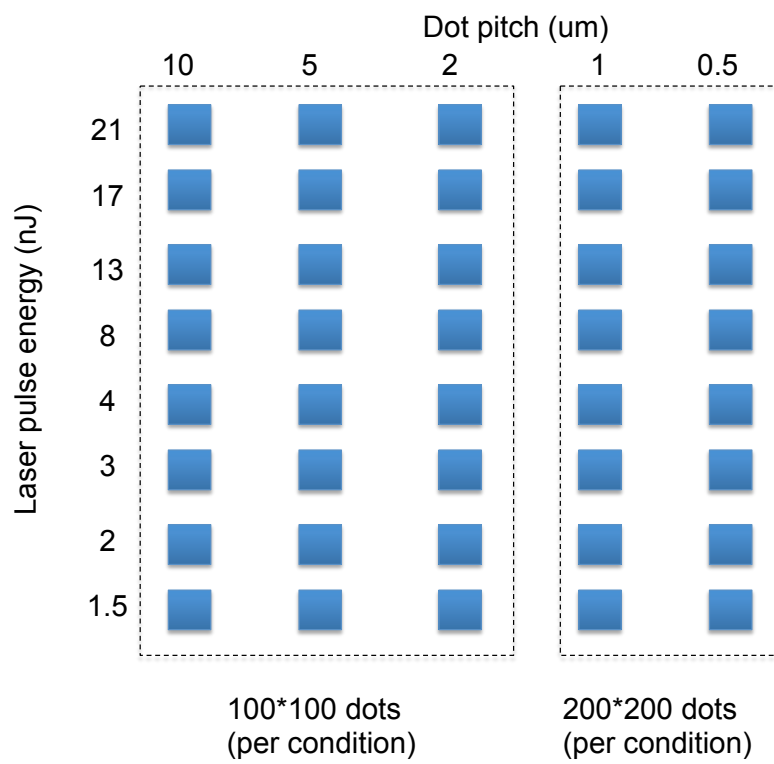


Figure B.1: Patterning conditions used on silicon (111) substrate.

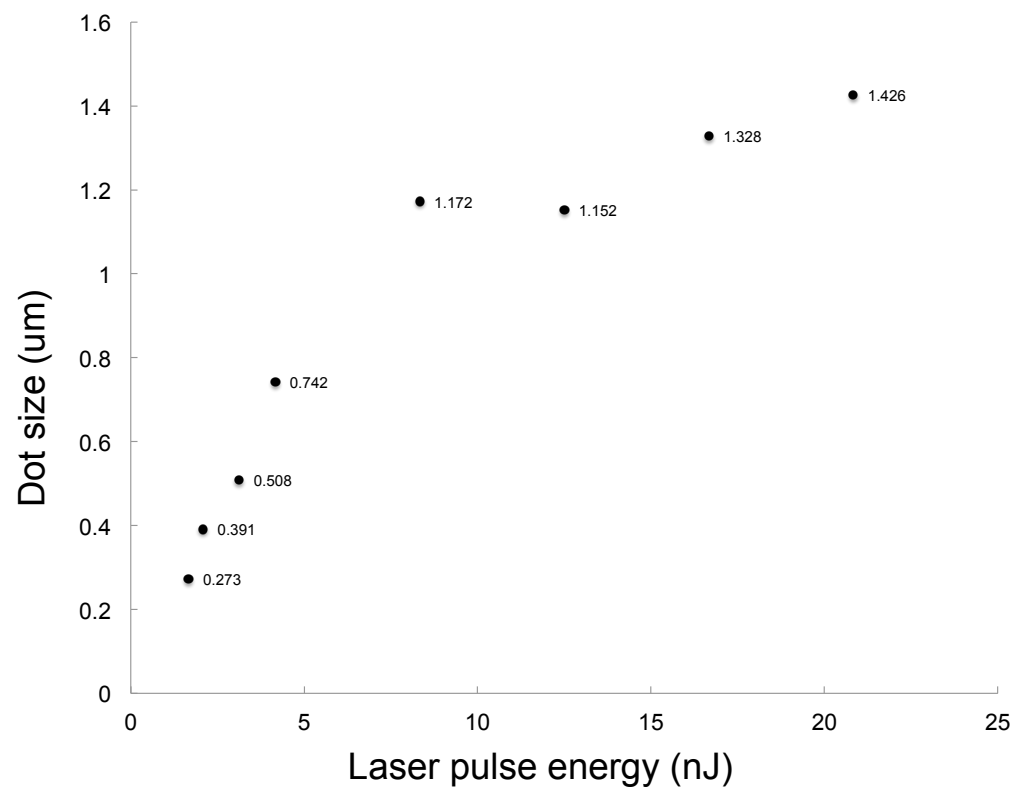
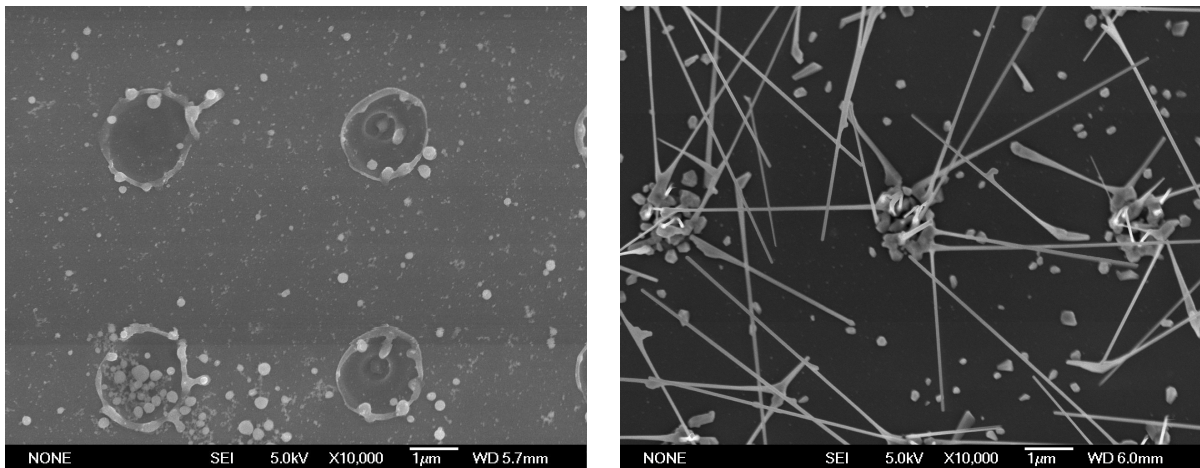


Figure B.2: Resulting dot size with respect to laser pulse energy used.



(a) Before GaAs deposition

(b) After GaAs deposition.

Figure B.3: Detail of dot with 1.1 μm diameter.

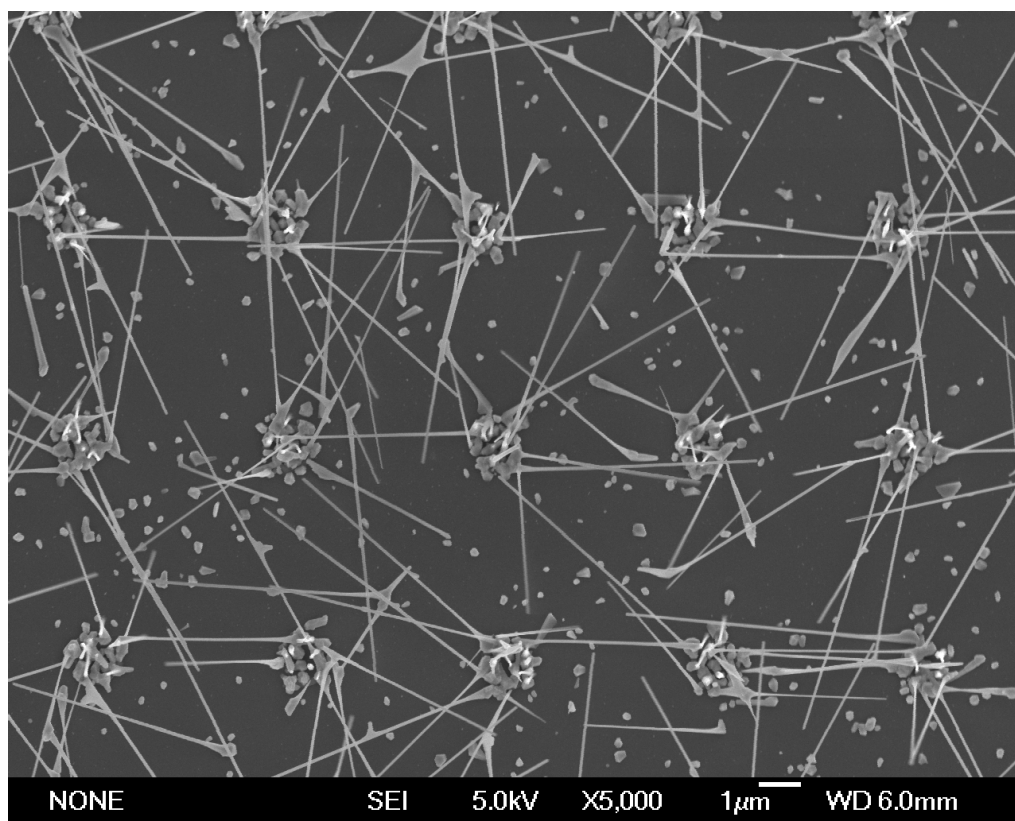
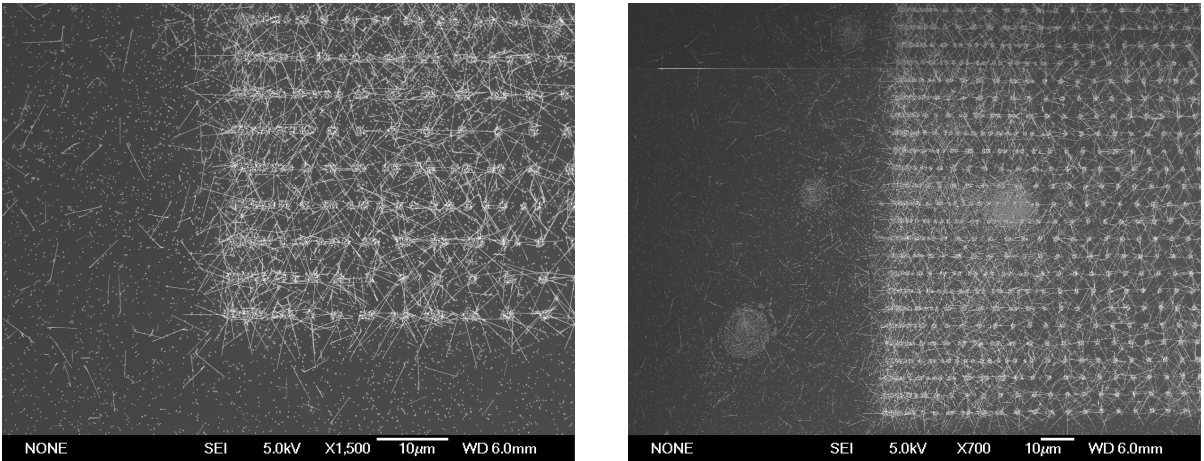


Figure B.4: Detail view of the region with $1\mu\text{m}$ diameter dots. Nanowires can be seen protruding from the laser-patterned dots.



(a)

(b)

Figure B.5: Detail of both a corner (left) and edge (right) showing the GaAs growth is primarily over the patterned region. The spots that form on the outside could be due to dust deposits on the surface.

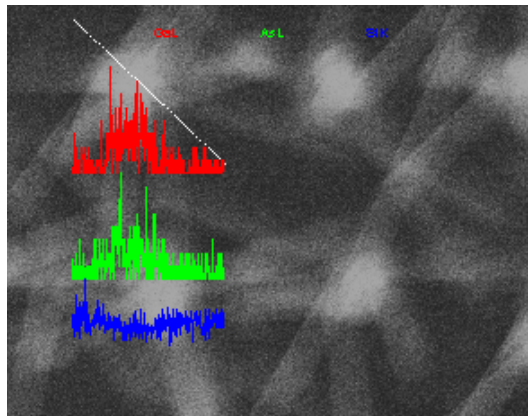


Figure B.6: EDX linescan of the post-growth sample confirming the gallium arsenide content is selectively deposited. Red, green, and blue denote the concentration of Ga, As, and Si along the line, respectively.

Appendix C

Transmission Electron Microscopy of GaAs Nanowires

Figure C.1 shows a representative low magnification plan-view transmission electron microscopy (TEM) image of a self-catalyzed MBE grown GaAs NW with a diameter of 53 nm. Energy dispersive X-ray spectroscopy (EDS) measurements show a 1:1 Ga:As composition ratio within the experimental error of the measurement, consistent with stoichiometric GaAs composition reported in other works on self-catalyzed MBE grown nanowires. Due to the appearance of stripes and inclusions in the image, the contrast is not uniform within the nanowire, and the wire is unlikely to be either single-crystal, or without defects, such as planar defects [136, 137]. This image also exhibits a very thin amorphous coating on the outer layer of the nanowire. The amorphous coating is likely due to an oxide layer which forms when the nanowire is exposed to air[137].

In semiconductor nanowires, twins, stacking faults, and polytypes arising from the zinc blende - wurtzite phase instability are well known the II-VI alloys, but have also been reported in the III-V alloys, and specifically in GaAs[138]. The dark lines perpendicular to the growth directions are stacking faults, as previously reported for GaAs NW growth[96, 83]. In fact, twins, which are stacking faults that produce changes over many atomic spacings, are common GaAs crystal defects[139], and can degrade the optical properties of the resulting semiconductor[136]. As indicated in the figure, the central and tip regions of the NW show a striped pattern. This striped pattern is typical, as III-V compound semiconductor NWs such as GaAs and InAs usually include both the hexagonal wurtzite (WZ) and cubic zinc- blende (ZB) structures within the wire. However, similar striped patterns observed in TEM can be due to presence of twin boundaries and stacking faults within the wire [140]. The region closest to the tip appears to have the highest concentration of stacking faults, possibly due to an abrupt change in growth conditions, namely a decrease in gallium flux[138].

The TEM studies also reveal that most of the GaAs nanowires terminate with a nanoparticle at one end as shown in Figure C.2. Figure C.3 shows the corresponding selective area diffraction pattern (SADP) of the wire. The electron diffraction is recorded perpendicular to the axis of the wire, showing that the growth occurs along the [111] direction.

Figure C.4 shows a high-resolution dark-field TEM image of the GaAs NW. There is *a-b-c* stacking in the crystal structure and the wire grows in the direction of the *c* axis.. Stacking faults can clearly be seen, and the distance between domains is approximately 6.4 nm. The d_{111} spacing for the (111) lattice planes was measured to be 0.32 ± 0.01 nm and thus confirms the [111] growth direction of the nanowires[137].

Figure C.5 shows the corresponding overview bright field (BF) TEM image of the GaAs NW. Figure C.6 shows the FFT of the previous BF and DF images, indicating both ZB and WZ symmetry.

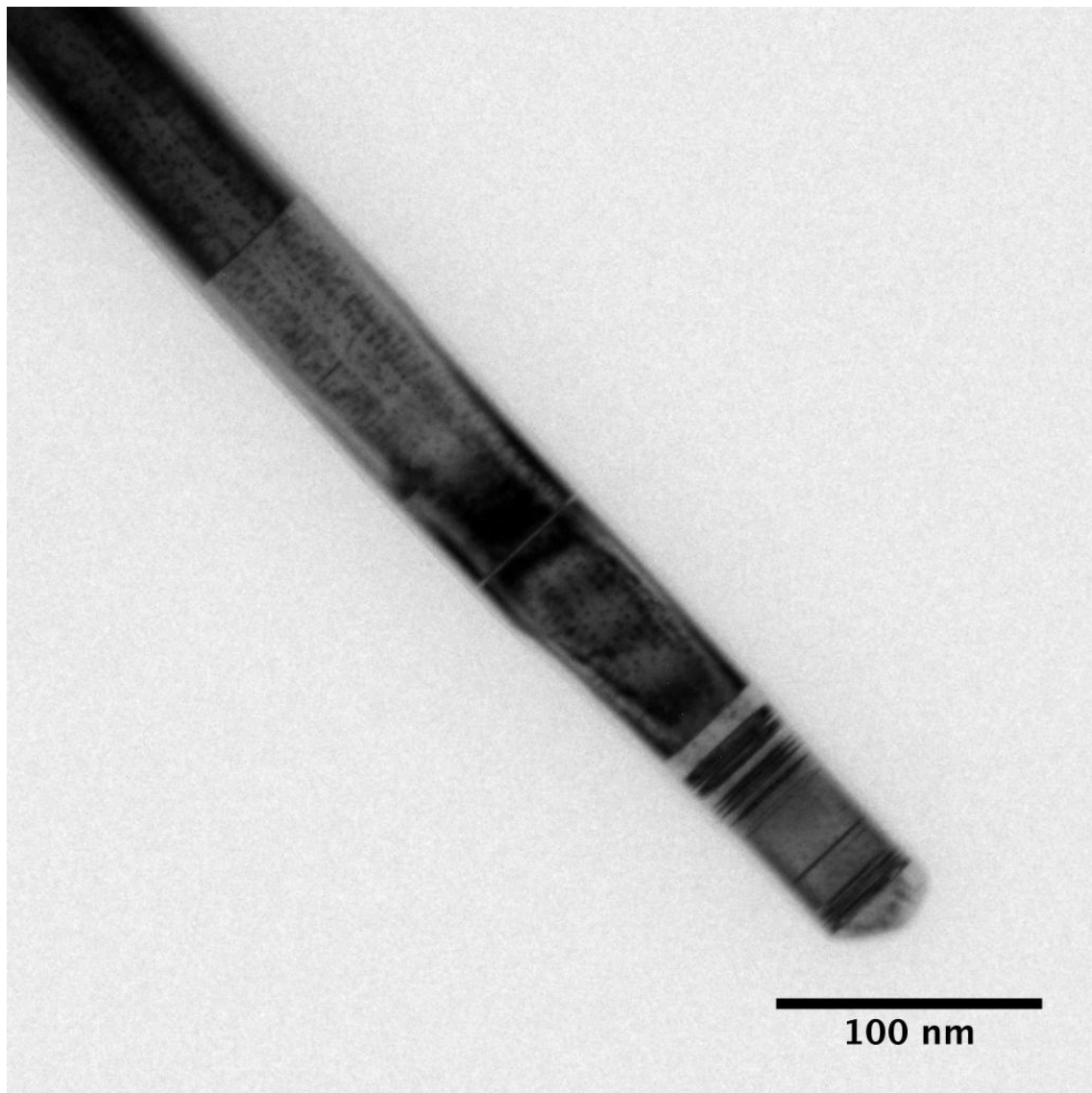


Figure C.1: Low magnification TEM image of a ~ 53 nm diameter GaAs NW.

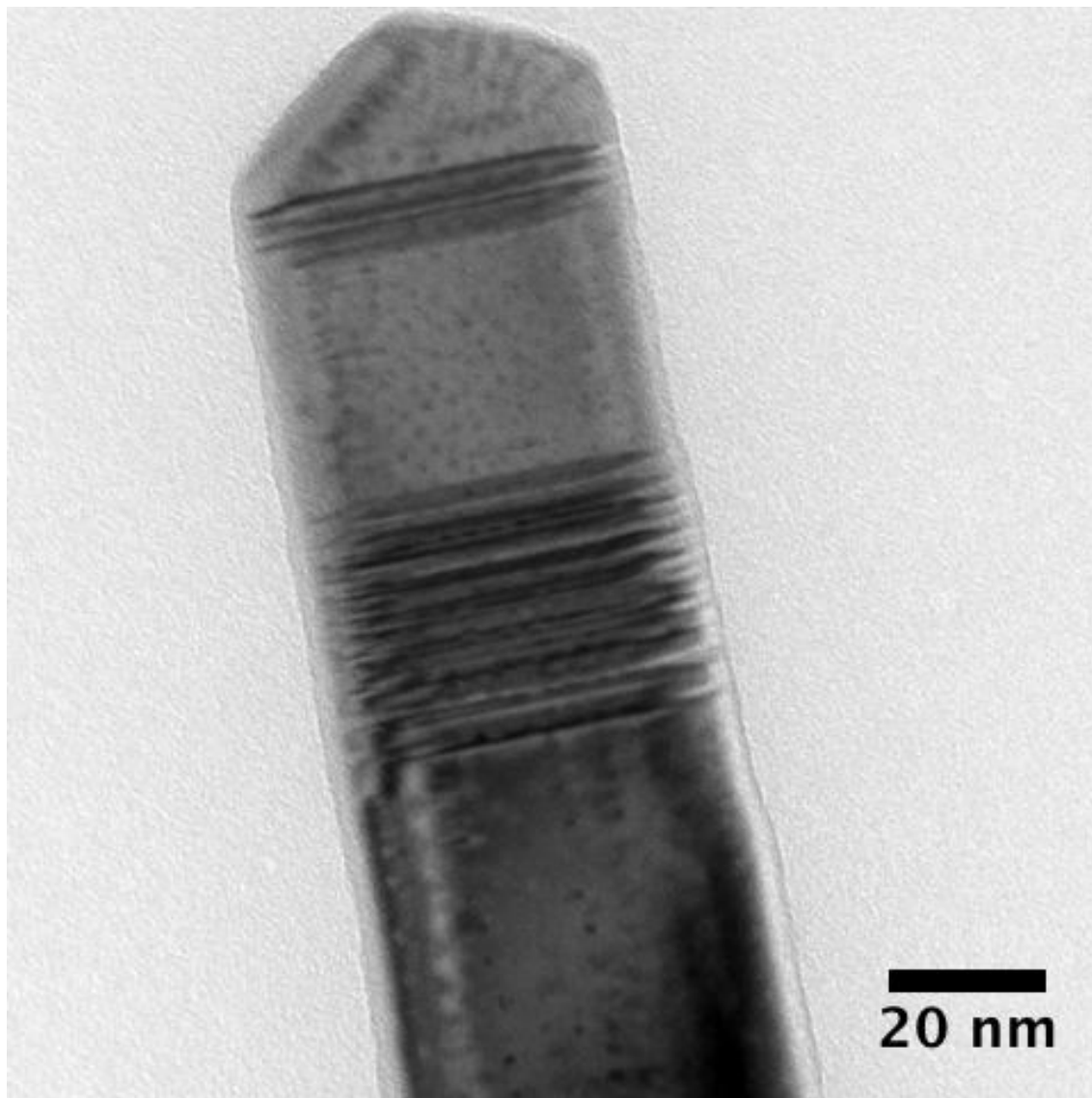


Figure C.2: TEM image of GaAs nanowire showing detail of tip and stacking faults near the tip.

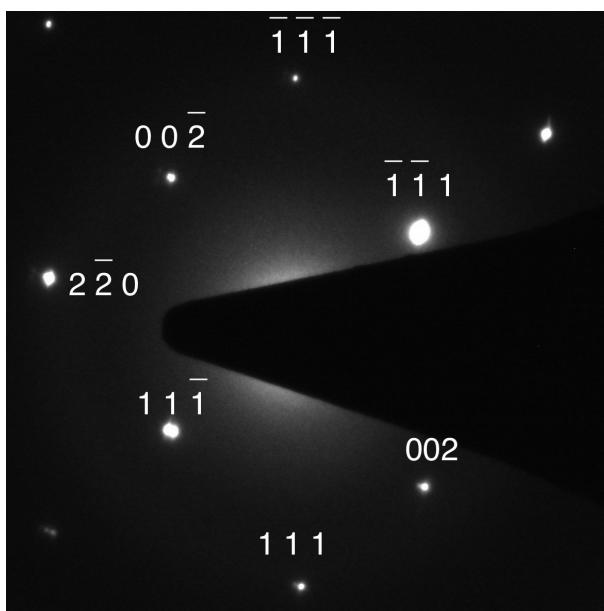


Figure C.3: Selective area diffraction pattern (SADP) of GaAs NW showing ZB type diffraction pattern.

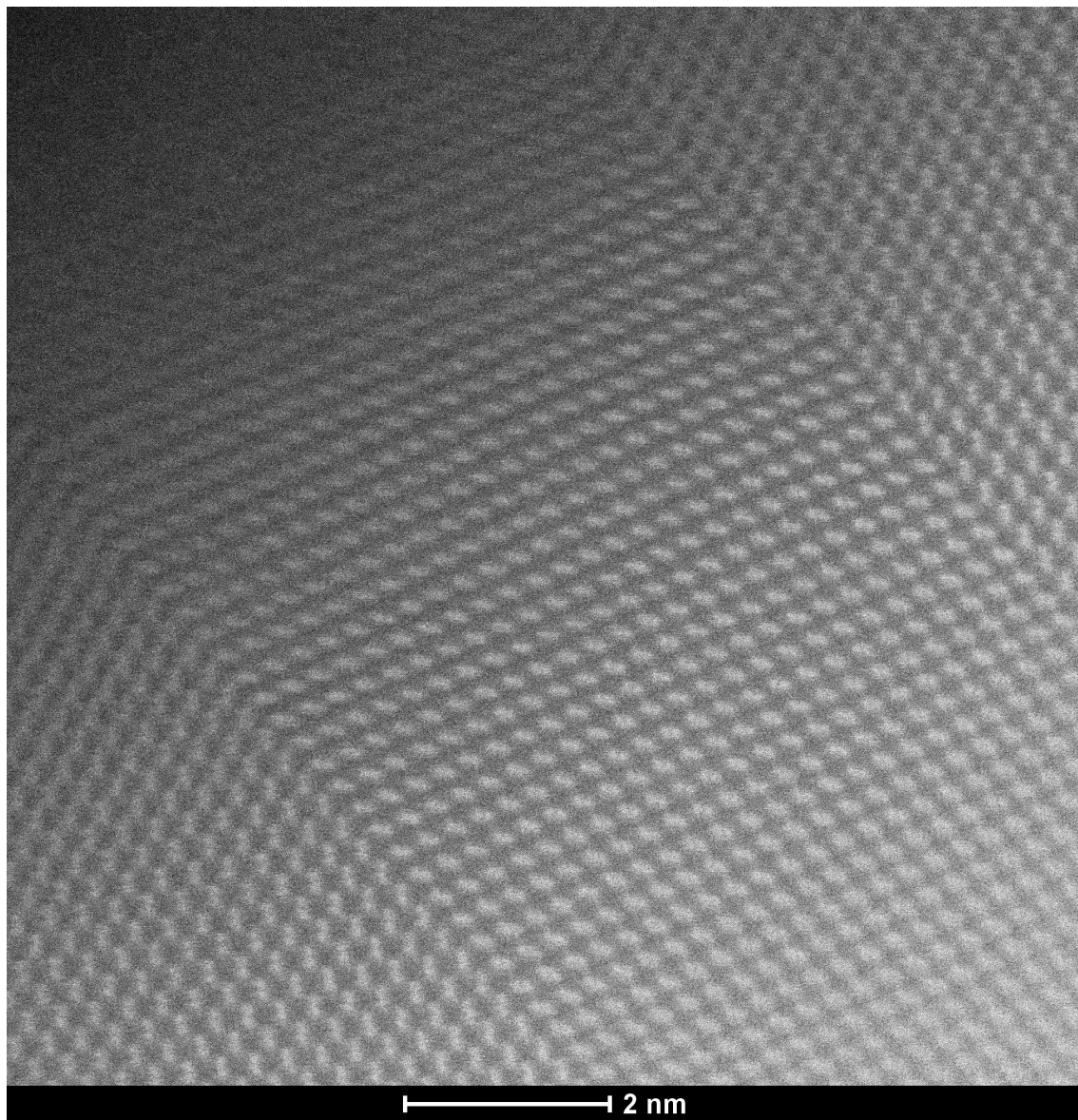


Figure C.4: High-magnification TEM image of GaAs nanowire showing stacking faults.

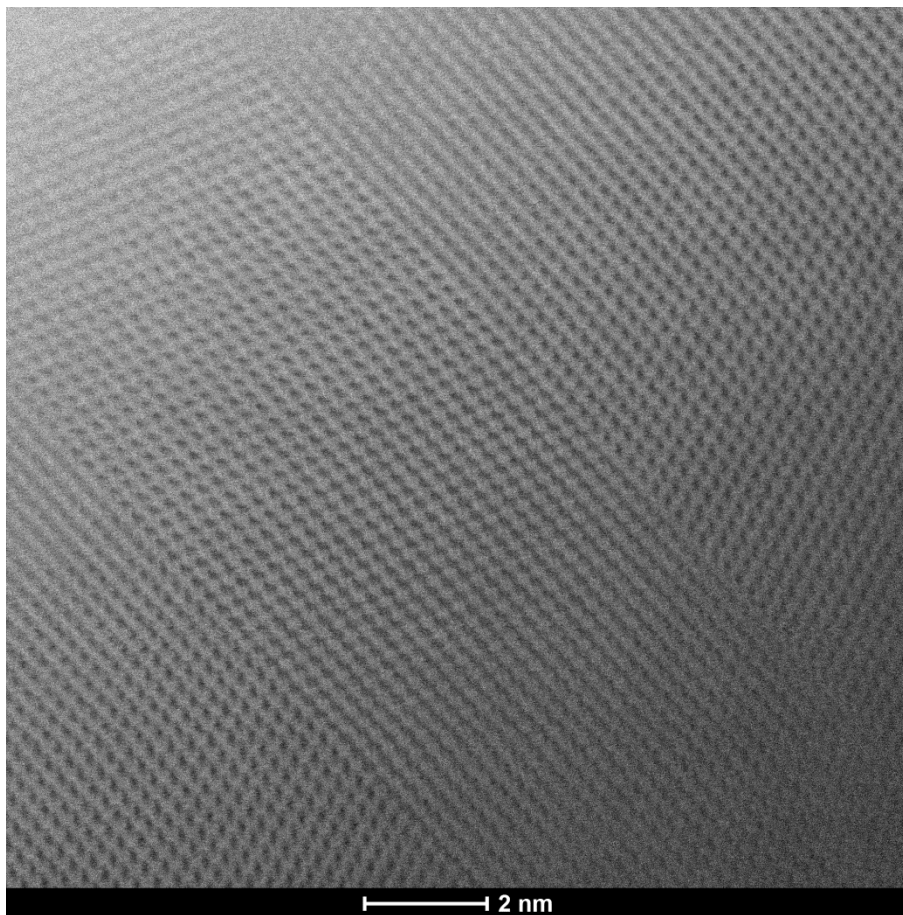


Figure C.5: Bright field (BF) TEM image of GaAs NW.

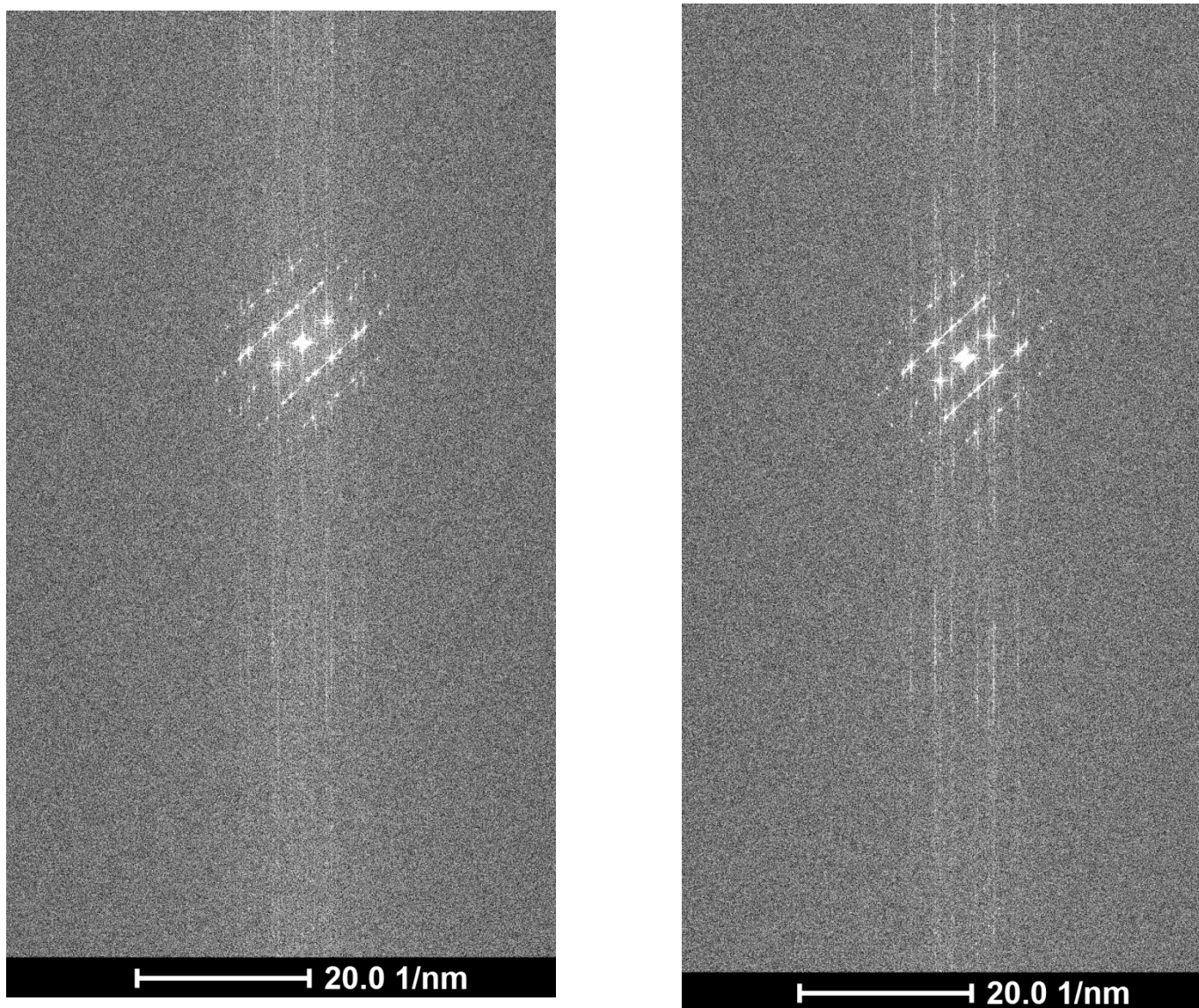


Figure C.6: FFT images of BF and DF TEM images.

Appendix D

Mathematica code

The following sections include the code for *Mathematica* calculations used in this dissertation.

IB Efficiency S-Q Analysis Code
Alex Luce - avluce@berkeley.edu

Version 2.2 - Nov'14

Due to the length of time required when generating the data points for the contour plot, this code is optimized for a parallel computing architecture.

Can be used to calculate the efficiency, and generate IV curves, for any arbitrary 3 bandgap IB system, tandem system, or single junction cell using the SQ Detailed Balance method. Reference paper is the 1997 PRL from Luque and Marti.

The efficiency of an ideal solar cell with an intermediate energy level (IB) is analyzed.

The model is based on the following 7 ideal conditions:

1. No non-radiative recombination
2. Infinite carrier mobility
3. Perfect ohmic contacts for electrons and holes, IB is electrically isolated.
4. Solar cell is a perfect absorber.
5. Back of cell is a perfect mirror, photons only escape from the front.
6. Absorption coefficient is a step function, single BE function describes population of photons escaping from cell in every mode.
7. Cell illumination is isotropic, ie. as ideal concentrator with no optical loss and concentration ratio of 46,000X

■ Initial declarations and equations

Declaration of fundamental constants

```
ClearAll["Global`*"]
ClearAll[Nt, em, eM, T, μ];
kB = 8.617 * 10^-5; (*Boltzmann constant eV/K *)
q = 1.6 * 10^-19; (*" electric charge C"*)
h = 6.63 * 10^-34; (*"Planck constant Js"*)
c = 3 * 10^8; "m/s";
```

The

The photon flux leaving the semiconductor as required by detailed balance. Note that there is a factor of π in the numerator (which is erroneously absent from the PRL paper). This is equation 5 from the 1997 PRL paper.

```

Nt[em_, eM_, T_, mu_] =  $\frac{2 * q^4 * 10^{-7} * \pi}{h^3 * c^2}$  NIntegrate[ $\frac{e^2}{\text{Exp}[\frac{e-\mu}{k_B * T}] - 1}$ , {e, em, eM}];
"photon flux in (6.25*1018*107)*m-2s-1";

```

```
NIntegrate::nlm : e = em is not a valid limit of integration . >>
```

```
NIntegrate::nlm : e = em is not a valid limit of integration . >>
```

```
ClearAll[ec, ei, eg, Ts, Ta, qV, muCi, muiv, x, y, muiv2];
```

The temperature of the two blackbodies.

```
Ta = 300; "cell temperature";
```

```
Ts = 6000; "sun temperature";
```

```
Inf = 10^4;
```

```
(*
ei=Ei;"smaller bandgap";
eg=Eg;"total bandgap";
ec=eg-ei;"larger bandgap";
*)
{ei, ec, eg}
```

Setting the NUMsteps as the number of steps, bounded by the lower bound and upper bound so as to avoid a discontinuity in the integral.

```
NUMsteps = 15;
LowerBound[ei_, eg_] := ei + 5 (eg - ei) / 6 + .01;
UpperBound[ei_, eg_] := eg - .01;
StepSize[ei_, eg_] := (eg - (ei + 7 (eg - ei) / 8)) / NUMsteps;
{ei, ec, eg}
```

muiv is the chemical potential, determined by solving the system of equations given by eq. (7) and (8) in the PRL paper

```
muiv2[qV_] := muiv /. FindRoot[Nt[ei, ec, Ts, 0] - Nt[ei, ec, Ta, muiv] ==
  Nt[ec, eg, Ts, 0] - Nt[ec, eg, Ta, qV - muiv], {muiv, (2 * ei + (qV - ec)) / 3,
  (ei + 2 * (qV - ec)) / 3, qV - ec, ei}, MaxIterations -> 1000];
```

```
muiv5[qV_, ei_, ec_, eg_] := muiv /. FindRoot[Nt[ei, ec, Ts, 0] - Nt[ei, ec, Ta, muiv] ==
  Nt[ec, eg, Ts, 0] - Nt[ec, eg, Ta, qV - muiv], {muiv, (99 * (qV - ec) + ei) / 100,
  ((qV - ec) + 99 * ei) / 100, Min[qV - ec, ei], Max[qV - ec, ei]};
```

```
ClearAll[qV, II, Pa, Ps, eta];
```

```
II[qV_] := (Nt[ec, Inf, Ts, 0] - Nt[ec, Inf, Ta, qV - muiv5[qV]]) * (6.25 * 1018 * 107) * q;
```

```
Ps := (5.67 * 10-8) * Ts4; "solar radiation power concentrated in W/m2";
```

Below, II is the current for both the IB and tandem cells, respectively. It is found by the balance of

electrons delivered to an external load, equations 6 and 9 from the 1997 PRL paper.

Ilib is the current of a intermediate band cell as a function of voltage (qV), and bandgap values.

```

IIib[qV_, ei_, ec_, eg_] :=
  ((Nt[eg, 10^4, Ts, 0] - Nt[eg, 10^4, Ta, qV]) + (Nt[ec, eg, Ts, 0] -
    Nt[ec, eg, Ta, qV - μiv5[qV, ei, ec, eg]])) * (6.25 * 1018 * 107) * q;
IItandem[qV_, ei_, ec_, eg_] := (Nt[ec, Inf, Ts, 0] -
  Nt[ec, Inf, Ta, qV - μiv5[qV, ei, ec, eg]]) * (6.25 * 1018 * 107) * q;

```

This calculates the efficiency by effectively by making of a table of the current times the voltage, and determining the maximum power point.

```

(*Voltage=Table[qV, {qV, LowerBound[Ei, Eg], UpperBound[Ei, Eg], StepSize[Ei, Eg]}] *)
Efficiencyib[Ei_, Eg_] :=
  Max[Table[qV, {qV, LowerBound[Ei, Eg], UpperBound[Ei, Eg], StepSize[Ei, Eg]}] *
    Table[IIib[qV, Ei, Eg - Ei, Eg],
      {qV, LowerBound[Ei, Eg], UpperBound[Ei, Eg], StepSize[Ei, Eg]}] / Ps]
Efficiencytandem[Ei_, Eg_] := Max[Table[qV, {qV, LowerBound[Ei, Eg],
  UpperBound[Ei, Eg], StepSize[Ei, Eg]}] * Table[IItandem[qV, Ei, Eg - Ei, Eg],
    {qV, LowerBound[Ei, Eg], UpperBound[Ei, Eg], StepSize[Ei, Eg]}] / Ps]

```

■ Calculation of efficiency based on bandgap values

Below is where you can plug in any arbitrary bandgap values to calculate the IB and tandem efficiencies.

Arguments *Efficiency[Ei, Eg]*, where Ei is the smaller gap, and Eg is the total gap.

Using a value of 0 for the lower gap will give the single junction case.

```

IBEfficiency = Efficiencyib[0.7, 1.93]
TandemEfficiency = Efficiencytandem[0, 1.4]

```

```
0.625893
```

This will calculate the efficiency by varying one parameter and keeping the other constant for a series of data points

```

Data = Table[Efficiencyib[gap, 2.4], {gap, 0, 1.2, 0.1}] // Timing
{320.563503, {0.20885, 0.235656, 0.267379, 0.302654, 0.341778, 0.385199,
  0.432841, 0.484804, 0.541528, 0.600715, 0.508897, 0.359069, 0.20885}}

DataTandem = Table[Efficiencytandem[gap, 2.4], {gap, .1, 2.3, 0.1}]
{0.0975444, 0.246091, 0.342453, 0.392103, 0.403448, 0.3858,
  0.349813, 0.304101, 0.255558, 0.20885, 0.166725, 0.130466, 0.100353,
  0.0760458, 0.0568759, 0.042049, 0.0307691, 0.0223088, 0.0160414,
  0.0114488, 0.00811573, 0.00571749, 0.00400687, 0.00279363}

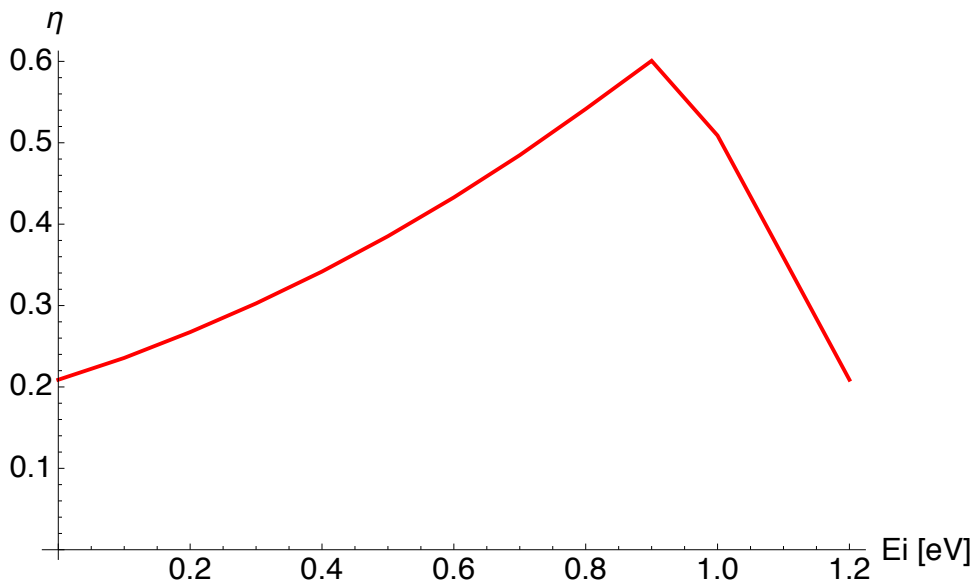
```

```
ListLinePlot[Data, DataRange → {0, 2.4}]
ListLinePlot[{308.721,
  {0.235656, 0.267379, 0.302654, 0.341778, 0.385199, 0.432841, 0.484804, 0.541528,
    0.600715, 0.508897, 0.359069, 0.20885, 1.75477, 1.35536, 4.48772, 6.17557,
    5.23383, 4.34794, 3.05306, 6.32723, 1.43363, 1.74855, -∞}}, DataRange → {0, 2.4}]
```

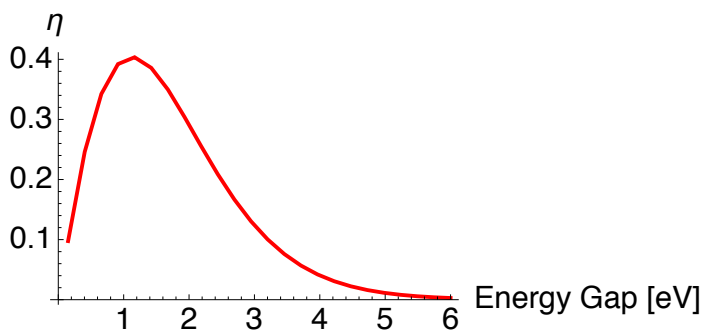
```
Data2 = Table[Efficiencyib[0, gap], {gap, .15, 3.5, 0.25}]
{0.0975444, 0.246091, 0.342453, 0.392103, 0.403448, 0.3858, 0.349813,
  0.304101, 0.255558, 0.20885, 0.166725, 0.130466, 0.100353, 0.0760458}
```

```
myplot[data_, min_, max_] := ListLinePlot[data,
  DataRange → {min, max}, AxesOrigin → {0, 0}, AxesLabel → {"Ei [eV]", "η"},
  BaseStyle → {FontFamily → "Helvetica", FontSize → 16}, PlotStyle → {Red, Thick}]
```

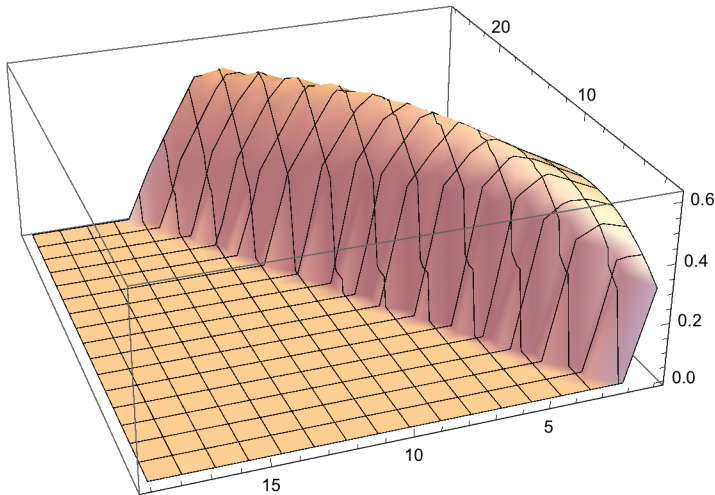
```
myplot[Data, 0, 1.2]
```



```
myplot[Data, .15, 6]
```




```
ListPlot3D[Data3[[2]]]
```



■ Contour Plot Part

calculates a matrix of efficiencies for E_i (lower gap) on one axis, and E_g (upper gap) on the other. 0 is returned if $E_i > 1/2 E_g$

```
EiLowerLimit = .5;
EiUpperLimit = .6;
EiStepSize = .1;
```

```
EgLowerLimit = 1.5;
EgUpperLimit = 1.6;
EgStepSize = .1;
```

```
Table[Ei, {Ei, EiLowerLimit, EiUpperLimit, EiStepSize}]
Table[Eg, {Eg, EgLowerLimit, EgUpperLimit, EgStepSize}]
```

```
{0.5, 0.6}
```

```
{1.5, 1.6}
```

```
Table[Which[Ei < 1 / 2 Eg, {Ei, Eg}, Ei ≥ 1 / 2 Eg, 0],
  {Ei, EiLowerLimit, EiUpperLimit, EiStepSize},
  {Eg, EgLowerLimit, EgUpperLimit, EgStepSize}] // MatrixForm
```

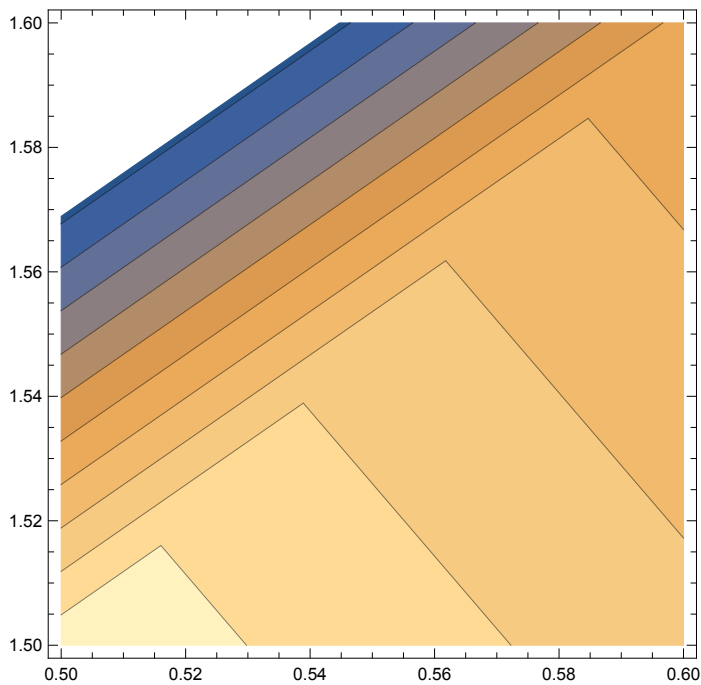
```
( ( 0.5 ) ( 0.5 ) )
( 1.5 ) ( 1.6 ) )
( 0.6 ) ( 0.6 ) )
( 1.5 ) ( 1.6 ) )
```

```
Monitor[ContourData = Table[Which[Ei < 1 / 2 Eg, Efficiencyib[Ei, Eg], Ei ≥ 1 / 2 Eg, 0],
  {Ei, EiLowerLimit, EiUpperLimit, EiStepSize},
  {Eg, EgLowerLimit, EgUpperLimit, EgStepSize}], Eg] // Timing // AbsoluteTiming
{33.042273, {30.648395, {{0.598502, 0.586738}, {0.526889, 0.576651}}}}
```

```
ContourData // MatrixForm;
```

```
MatrixPlot[ContourData];
ListDensityPlot[ContourData];
```

```
ListContourPlot[ContourData,
  DataRange → {{EiLowerLimit, EiUpperLimit}, {EgLowerLimit, EgUpperLimit}}]
```



```
data = Table[{x = RandomReal[{-2, 2}], y = RandomReal[{-2, 2}], Sin[x y]}, {1000}] //
  TableForm;
```

Build table using parallel computation

This is probably the quickest way to generate the data, you can set the values and step size below

```
EiLowerLimit = .5;  
EiUpperLimit = .6;  
EiStepSize = .1;
```

```
EgLowerLimit = 1.5;  
EgUpperLimit = 1.6;  
EgStepSize = .1;
```

```
Monitor[ContourData = ParallelTable[Which[Ei < 1 / 2 Eg, Efficiencyib[Ei, Eg],  
    Ei ≥ 1 / 2 Eg, 0], {Ei, EiLowerLimit, EiUpperLimit, EiStepSize},  
    {Eg, EgLowerLimit, EgUpperLimit, EgStepSize}], Eg] // Timing // AbsoluteTiming  
{24.189849, {2.007156, {{0.598502, 0.586738}, {0.526889, 0.576651}}}}
```

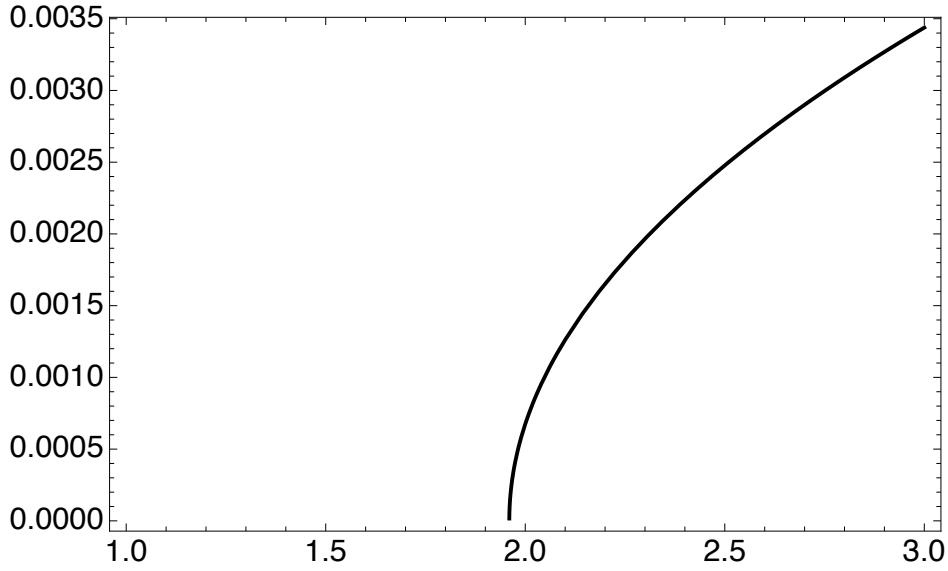
```
ListContourPlot[ContourData,  
    DataRange → {{EiLowerLimit, EiUpperLimit}, {EgLowerLimit, EgUpperLimit}}]
```

Updated 4/1/2014

```
ClearAll[R0, V, x, Gm, ImG, G, EE, Ek, k, R, P1,  
P2, P3, P4, P5, P6, Rhh, Rlh, Rso, Rtotal, Eplus, Eminus];
```

GaAsPN

```
ħ = 1.05 * 10^-34;  
b = 5.55 * 10^-10;  
Me1 = .067 * 9.11 * 10^-31;  
Eb1 = ħ^2 (2 π / b)^2 / (2 Me1) / (1.6 * 10^-19)  
72.3451  
  
Ed = 186 / 100;  
Eb := 240.4; (*conduction band width calculated above*)  
V = 284 / 100;  
Eg0 = 196 / 100; (*CBE WRT to VBE at x=54% As content*)  
  
Me = 0.1; Mhh = 0.54;  
  
Mlh = 0.082; Mso = 0.154; Delta = 0.19;  
x = 0.02;  
Eplus[xx_] := 0.5 (Eg0 + Ed + Sqrt[(Eg0 - Ed)^2 + 4 V^2 xx]);  
Eminus[xx_] := 0.5 (Eg0 + Ed - Sqrt[(Eg0 - Ed)^2 + 4 V^2 xx]);  
  
R0[EE_] := 4 Pi Sqrt[EE - Eg0] / Eb^(3/2);  
  
RV[EE_] := 4 Pi Sqrt[0 - EE] / Eb^(3/2);  
  
Gm = -I Pi V^2 R0[Ed];  
(*There should be a pre-factor BETA here,  
which is determined experimentally as BETA=0.22*)  
G[EE_, Ek_] := (EE - (Ed + I Gm)) / ((EE - Ek + I 10^(-6)) (EE - (Ed + I Gm)) - V^2 x);  
  
R[EE_] :=  
(1 / Pi) Abs[NIntegrate[R0[Ek] Im[G[EE, Ek]], {Ek, Eg0, Eb}, Method -> Automatic,  
MinRecursion -> 0, MaxRecursion -> 15, WorkingPrecision -> 24]];  
  
Rhh[EE_] := (1 / Pi) Abs[NIntegrate[R0[Ek] Im[G[EE - (Me / Mhh) Ek, Ek]], {Ek, Eg0, Eb},  
MinRecursion -> 0, MaxRecursion -> 15, WorkingPrecision -> 24]];  
  
P0 = Plot[R0[Ek], {Ek, 1, 3}, AxesLabel -> {"Energy (eV)", "DOS (1/eV unit-cell)"},  
PlotStyle -> {Directive[Thick, Black]},  
LabelStyle -> Directive[FontFamily -> "Helvetica", 16], Frame -> True]  
  
PVB = Plot[2 * RV[Ek], {Ek, -.5, 3}, PlotRange,  
AxesLabel -> {"Energy (eV)", "DOS (1/eV unit-cell)"},  
PlotStyle -> {Directive[Thick, Black]},  
LabelStyle -> Directive[FontFamily -> "Helvetica", 16], Frame -> True,  
Filling -> Axis, FrameStyle -> Thick, FillingStyle -> Directive[Opacity[0.2], Blue]]
```



```
Plot[2 RV[Ek], {Ek, -0.5, 3}, PlotRange,
 AxesLabel -> {Energy (eV), DOS (1/eV unit-cell)},
 PlotStyle -> {Directive[Thick, Black]},
 LabelStyle -> Directive[FontFamily -> Helvetica, 16], Frame -> True, Filling -> Axis,
 FrameStyle -> Thick, FillingStyle -> Directive[Opacity[0.2], Blue]]
```

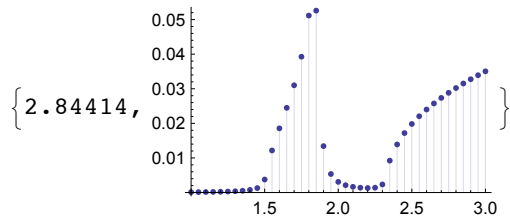
Gm // N

0.0270144 + 0. i

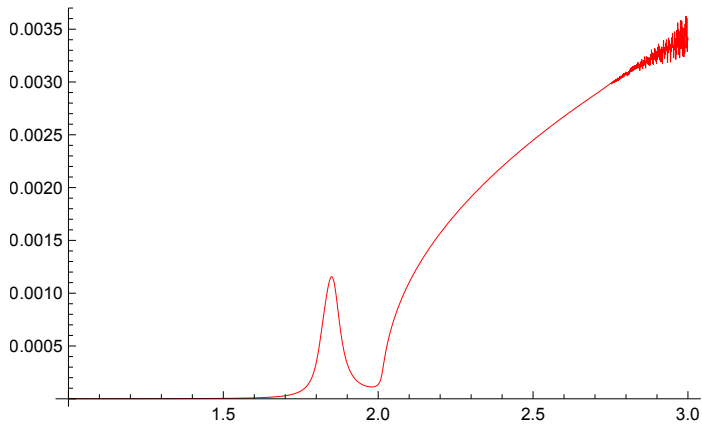
R[EE_] :=

```
(1 / Pi) Abs[NIntegrate[RO[Ek] Im[G[EE, Ek]], {Ek, Eg0, Eb}, Method -> Automatic,
 MinRecursion -> 0, MaxRecursion -> 15, WorkingPrecision -> 24]];
```

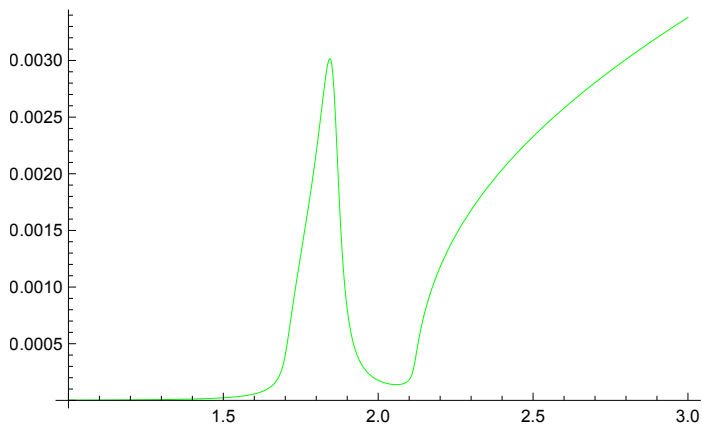
DiscretePlot[R[y], {y, 1, 3, .05}] // Timing



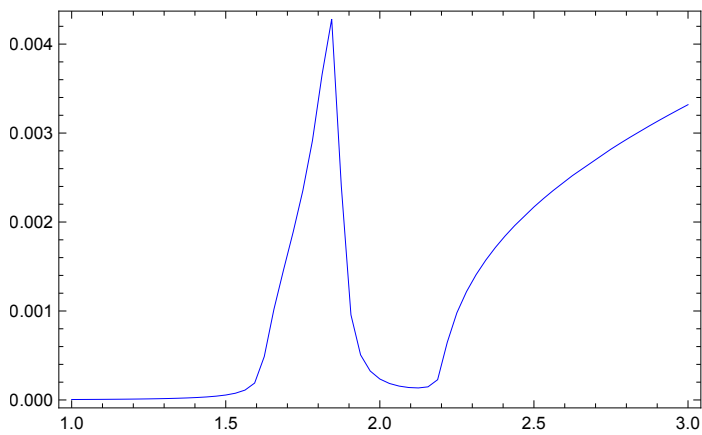
```
x = .001;  
P001 = Plot[R[EE], {EE, 1, 3}, Filling -> None, PlotStyle -> {Directive[Red]}]
```



```
x = .005;  
P005 = Plot[R[EE], {EE, 1, 3}, Filling -> None, PlotStyle -> {Directive[Green]}]
```



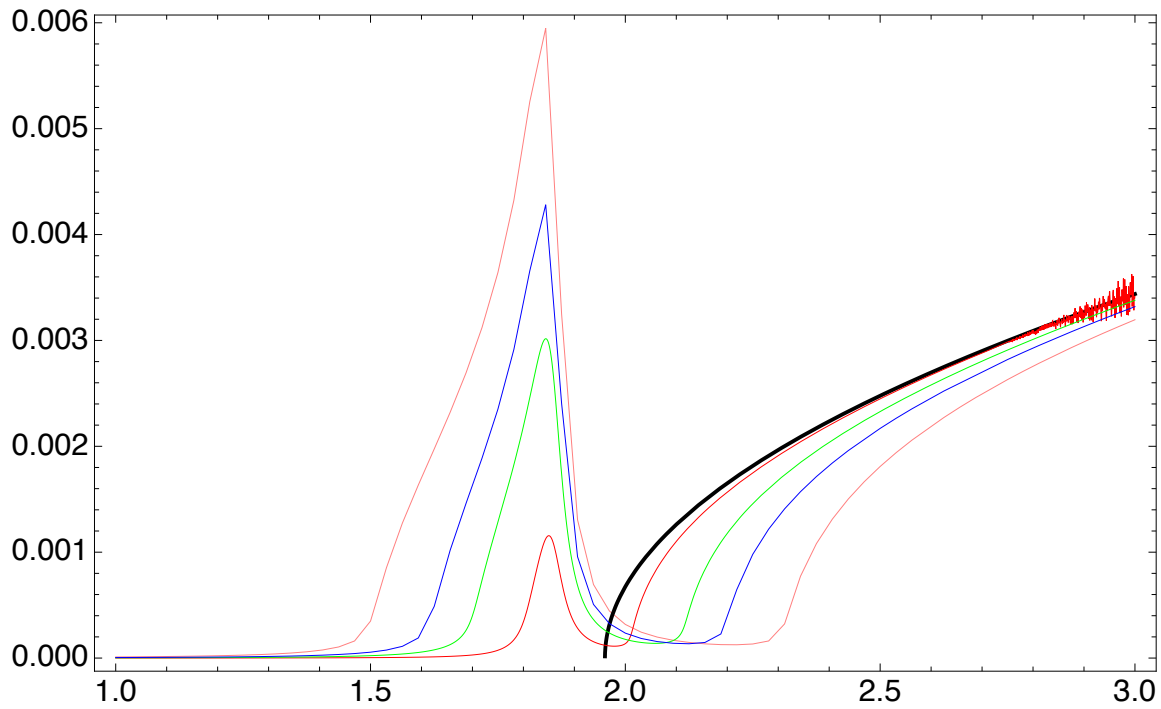
```
x = .01;  
P01 = Plot[R[EE], {EE, 1, 3}, PlotPoints -> NUMpts,  
Frame -> True, Filling -> None, PlotStyle -> {Directive[Blue]}]
```



```

x = .02;
P02 = Plot[R[EE], {EE, 1, 3}, PlotPoints -> NUMpts,
  AxesLabel -> {"Energy (eV)", "DOS (1/eV unit cell)"},
  PlotStyle -> {Directive[Pink]}, LabelStyle ->
  Directive[FontFamily -> "Helvetica", 16], Frame -> True, Filling -> None];
Show[P02, P0, P001, P005, P01]

```



GaAsN

```

ħ = 1.05 * 10^-34;
b = 5.55 * 10^-10;
Me1 = .1 * 9.11 * 10^-31;
Eb1 = ħ^2 (2 π / b)^2 / (2 Me1) / (1.6 * 10^-19)
48.4712

```

```

Ed = 0.23 + Eg0;
Eb = 220.4; (*but Chiao had 70.4 here in his thesis-
why? all other values work! factor of 4.7?*)

V = 2.7; Eg0 = 1.42; Me = 0.067; Mhh = 0.51;
Mlh = 0.082; Mso = 0.154; Delta = 0.34;
x = 0.01;

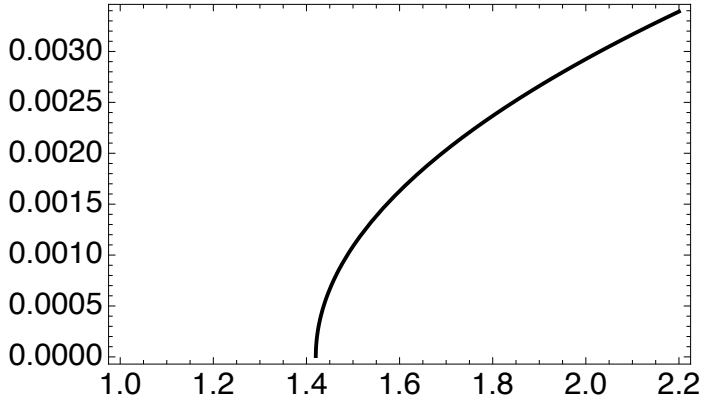
Eplus = 0.5 (Eg0 + Ed + Sqrt[(Eg0 - Ed)^2 + 4 V^2 x]);
Eminus = 0.5 (Eg0 + Ed - Sqrt[(Eg0 - Ed)^2 + 4 V^2 x]);
RO[EE_] := 4 * Pi * Sqrt[EE - Eg0] / Eb^(3/2);
Gm = Pi V^2 RO[Ed];

G[EE_, Ek_] := (EE - (Ed + I Gm)) / ((EE - Ek + I 10^(-6)) (EE - (Ed + I Gm)) - V^2 x);

R[EE_] := (1 / Pi) Abs[NIntegrate[RO[Ek] Im[G[EE, Ek]], {Ek, Eg0, Eb},
MinRecursion -> 3, MaxRecursion -> 10, WorkingPrecision -> 16]];
Rhh[EE_] := (1 / Pi) Abs[NIntegrate[RO[Ek] Im[G[EE - (Me / Mhh) Ek, Ek]],
{Ek, Eg0, Eb}, MinRecursion -> 3, MaxRecursion -> 10, WorkingPrecision -> 16]];

POGaAsN =
Plot[RO[Ek], {Ek, 1, 2.2}, AxesLabel -> {"Energy (eV)", "DOS (1/eV unit-cell)"},
PlotStyle -> {Directive[Thick, Black]},
LabelStyle -> Directive[FontFamily -> "Helvetica", 16], Frame -> True]

```



```

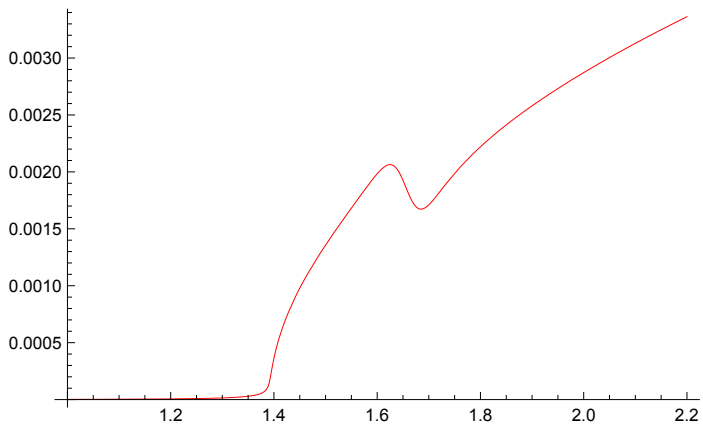
R[EE_] := (1 / Pi) Abs[NIntegrate[RO[Ek] Im[G[EE, Ek]], {Ek, Eg0, Eb},
Method -> Automatic, MinRecursion -> 0, MaxRecursion -> 15, WorkingPrecision -> 24]];

(*DiscretePlot[R[y], {y, 1, 3, .05}]*)

```

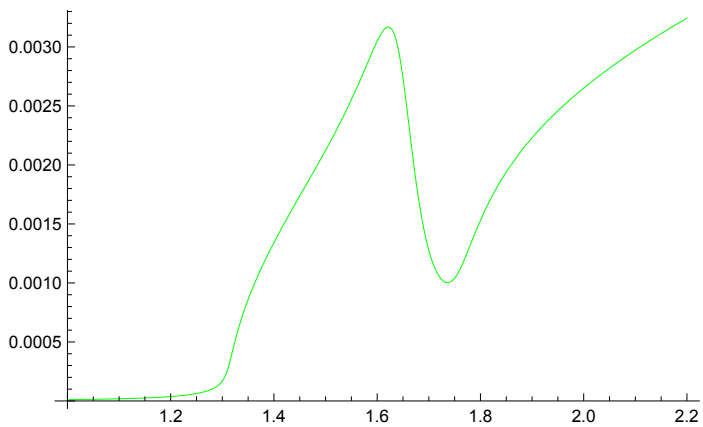
```
x = .001;
```

```
P001GaAsN = Plot[R[EE], {EE, 1, 2.2}, Filling -> None, PlotStyle -> {Directive[Red]}]
```



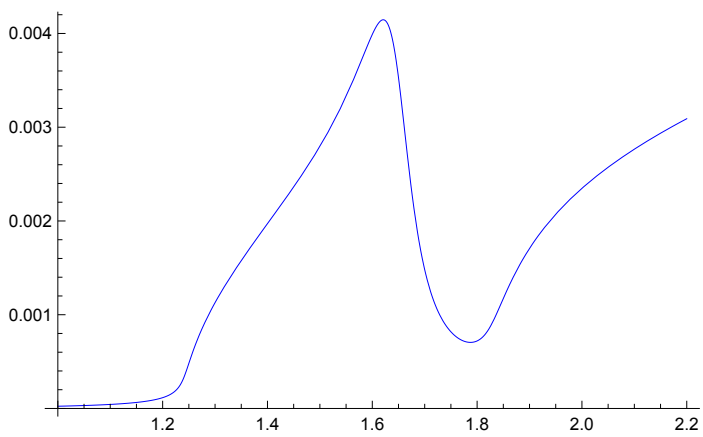
```
x = .005;
```

```
P005GaAsN = Plot[R[EE], {EE, 1, 2.2}, Filling -> None, PlotStyle -> {Directive[Green]}]
```



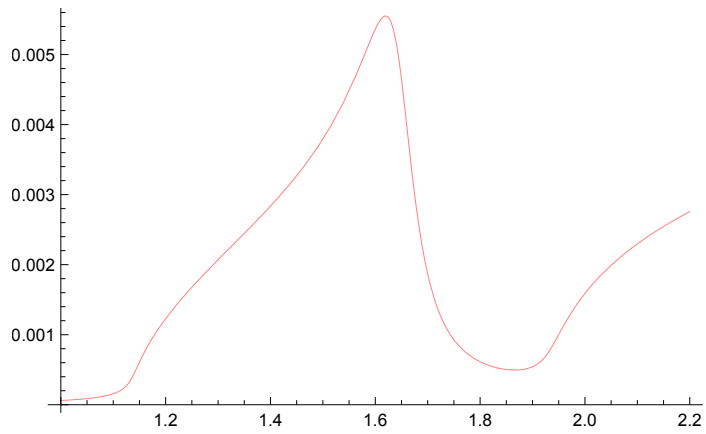
```
x = .01;
```

```
P01GaAsN = Plot[R[EE], {EE, 1, 2.2}, Filling -> None, PlotStyle -> {Directive[Blue]}]
```

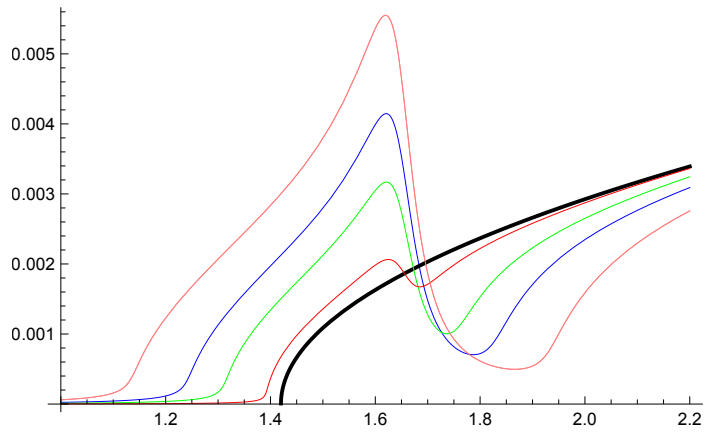


```
x = .02;
```

```
P02GaAsN = Plot[R[EE], {EE, 1, 2.2}, Filling -> None, PlotStyle -> {Directive[Pink]}]
```



```
Show[P02GaAsN, P01GaAsN, P0GaAsN, P005GaAsN, P001GaAsN, P02GaAsN]
```



Fermi Level in GaNAsP

We consider here GaN(x)As(y)P(1-x-y)

Definitions

From S.L Chuang, *Physics of Photonic Devices*. 2nd. ed.

Effective mass

from <http://www.iue.tuwien.ac.at/phd/palankovski/node40.html>

GaAs(y)P(1-y) for Y>50% is direct band gap

For electrons

me=0.067 (GaAs)

me=0.5 (GaP)

For holes

mh=0.49 (GaAs)

mh=0.6 (GaP)

```
ClearAll[mestar, mestary, mhstar, mhstary]
```

```
meA = 0.067;
```

```
meB = 0.5;
```

```
mhA = 0.49;
```

```
mhB = 0.6;
```

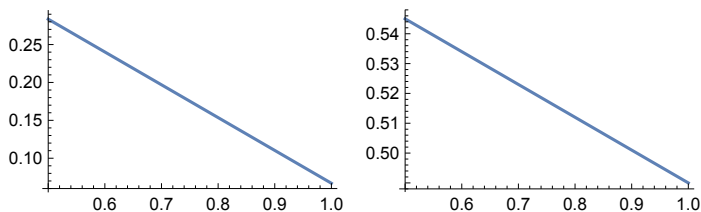
```
mestary[y_] := meA (y) + meB (1 - y)
```

```
mhstary[y_] := mhA (y) + mhB (1 - y)
```

```
p1 = Plot[mestary[x], {x, .5, 1}];
```

```
p2 = Plot[mhstary[x], {x, .5, 1}];
```

```
GraphicsRow[{p1, p2}]
```



Assume here that $y=54\%$ As

```

y := .54;
mestar := mestary[y]
mhstar := mhstary[y]
mestar
mhstar
0.26618
0.5406

```

Band Edge concentration parameters

$$N_c = 2 * \left(\frac{m_e * kBT}{2 \pi \hbar^2} \right)^{3/2}$$

$$N_v = 2 * \left(\frac{m_h * kBT}{2 \pi \hbar^2} \right)^{3/2}$$

eq. (2.2.39)

```

T = 300;
Nc = 2.51 * 10^19 (mestar * T / 300) ^ (3 / 2)
Nv = 2.51 * 10^19 (mhstar * T / 300) ^ (3 / 2)
2.95483 × 10^18
9.79458 × 10^18

```

Determination of Fermi Level (in eV)

let $\eta = (E_f - E_c) / kBT$
maximum error is 0.006

assume $kBT = 25.8 \text{ meV}$ at 300K

```

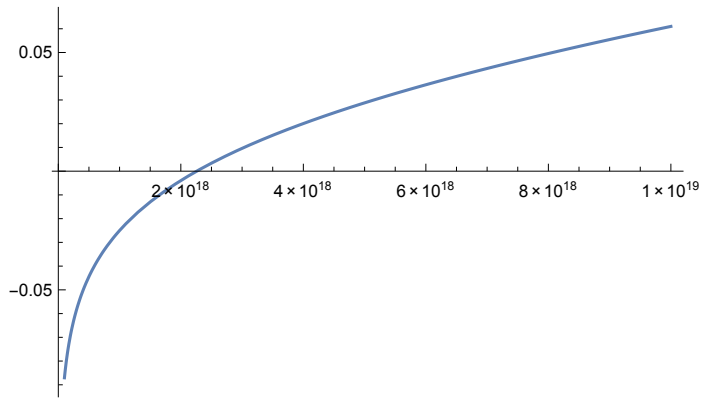
kBT = 0.0258;
u[n_] := n / Nc

v[n_] := (3 * Sqrt[Pi] * u[n] / 4) ^ (2 / 3)
eta[n_] := Log[u[n]] / (1 - u[n]^2) + v[n] / (1 + (0.24 + 1.08 * v[n]) ^ (-2))

eta[10^17] * kBT;

```

```
p2 = Plot[η[x] * kBT, {x, 1 * 10^17, 1 * 10^19}]
```



Program to fit lineshape for analysis of PR data. Written by AVL 4.2013.

```
{FileNameSetter[Dynamic[f]], Dynamic[f]}
```

```
data := Import[f];
```

```
data[[All, 1]] // TableForm;
```

```
data[[All, 1]];
```

```
(*this is just a check to make sure the data was imported correctly*)
```

Be careful how column 1 data is needed. If it is in nm you need to convert to eV (for raw data)

```
energy := 1240 / data[[All, 1]];
```

```
PRdata := data[[All, 3]];
```

```
Transpose[{energy, PRdata}];
```

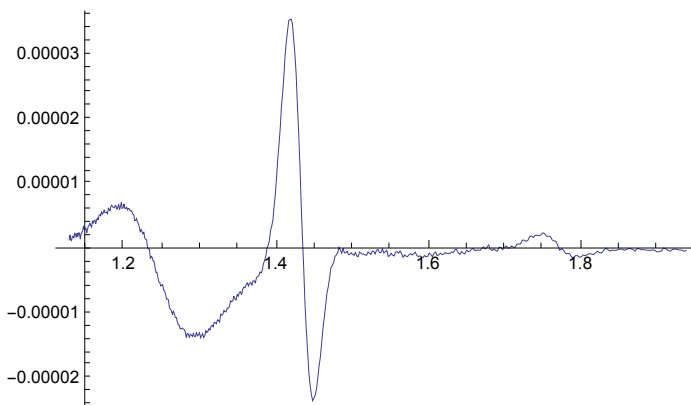
```
xy = Thread[{energy, PRdata}];
```

```
Length[PRdata]
```

```
ListLinePlot[xy, PlotRange -> Full]
```

```
ListLinePlot[xy[[250 ;; 461]], PlotRange -> Full]
```

```
ListLinePlot[xy[[80 ;; 180]], PlotRange -> Full]
```



```
ClearAll["Global`*"]
```

```
Eg = 1.4;
```

```
 $\Gamma$  = 1;
```

```
Const = .1;
```

```
 $\theta$  = 1;
```

```
ClearAll[PR, Eg,  $\Gamma$ , Const,  $\theta$ ]
```

We can attempt to model the transition to extract values for the fitting parameters (ballpark)

For a 3D system, $m=5/2$, for a 2D $m=3$

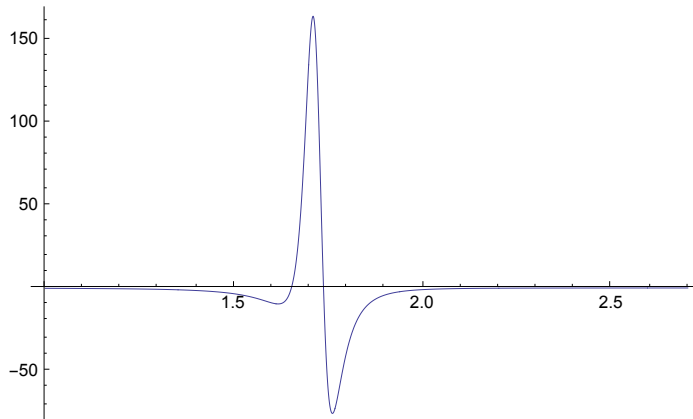
Below is the standard PR model from Aspenes

```

m = 5 / 2;
PR[E0_, Eg_, Const_,  $\theta$ _,  $\Gamma$ _] := Re[Const E^ (I  $\theta$ ) (E0 - Eg + I  $\Gamma$ ) ^ (-m)]
PRmodel = Re[Const1 E^ (I  $\theta$ 1) (E0 - Eg1 + I  $\Gamma$ 1) ^ (-m)]
Plot[PR[y, 1.72, .10, -2  $\pi$  / 4, .05], {y, 1, 2.7}, PlotRange -> Full]

```

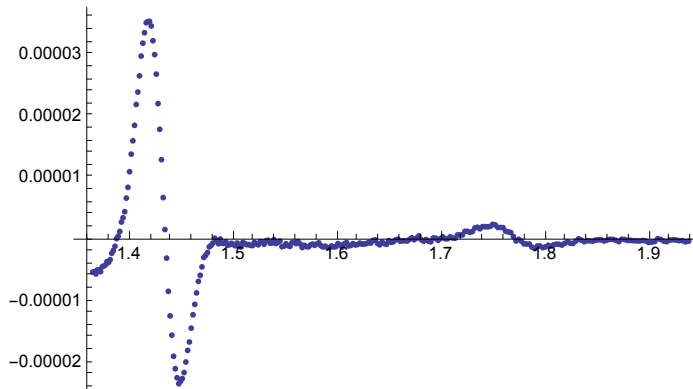
$$\text{Re} \left[\frac{\text{Const1 } e^{i \theta 1}}{(E0 - Eg1 + i \Gamma 1)^{5/2}} \right]$$



```

E01 = 1.2;
Manipulate[Plot[PR[y, E01, .00000001, theta1, gamma] +
  PR[y, E01 + deltaE, .00000001, theta2, gamma2], {y, 1.1, 1.9}, PlotRange -> Full],
  {theta1, 0, 2  $\pi$ }, {theta2, 0, 2  $\pi$ }, {gamma, .005, .1}, {gamma2, .005, .1},
  {deltaE, 0, 0.4}, UnsavedVariables -> {theta1, theta2, gamma, gamma2, deltaE},
  LocalizeVariables -> False]
ListPlot[xy[[1 ;; 270]], PlotRange -> All]

```



```

Show[ ListPlot[xy[[120 ;; 460]], PlotRange -> All],
  Plot[{PR[y, E01, .00000001, theta1, gamma] +
  PR[y, E01 + deltaE, .00000002, theta2, gamma2]},
  {y, 1.1, 2.0}, PlotRange -> Full, PlotStyle -> Red]]

```

Double peak fitting

```
(*double peak fit*)
m = 3;
fitdata = xy[[120 ;; 460]];
ClearAll[E0, E01]

fit2 = FindFit[fitdata, {PR[E0, E01, Const1,  $\theta$ 1,  $\Gamma$ 1] + PR[E0, E02, Const2,  $\theta$ 2,  $\Gamma$ 2]},
  {{E01, 1.2}, {Const1, .00000001}, { $\theta$ 1, theta1}, { $\Gamma$ 1, gamma},
  {E02, 1.42}, {Const2, .00000002}, { $\theta$ 2, theta2}, { $\Gamma$ 2, gamma2}}, E0,
  AccuracyGoal  $\rightarrow$  10, PrecisionGoal  $\rightarrow$  10, MaxIterations  $\rightarrow$  Automatic]

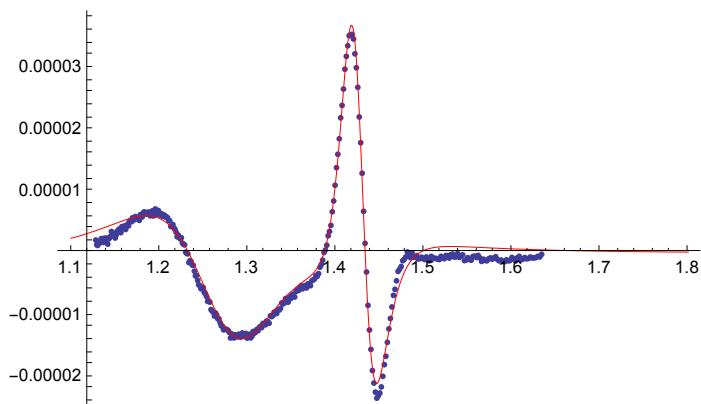
Show[ListPlot[fitdata, PlotRange  $\rightarrow$  All],
  Plot[Evaluate[(PR[y, E01, Const1,  $\theta$ 1,  $\Gamma$ 1] + PR[y, E02, Const2,  $\theta$ 2,  $\Gamma$ 2]) /. fit2],
  {y, 1.1, 1.8}, PlotRange  $\rightarrow$  Full, PlotStyle  $\rightarrow$  Red]]
fit2
```

```
(*calculate RMS Error for Fit*)
fitFunc[y_] :=
  Evaluate[(PR[y, E01, Const1,  $\theta$ 1,  $\Gamma$ 1] + PR[y, E02, Const2,  $\theta$ 2,  $\Gamma$ 2]) /. fit2]
RMSerror1 = RootMeanSquare[fitdata[[All, 2]] - Map[fitFunc, fitdata[[All, 1]]]]
```

```
Plot[Evaluate[( $\rho$ [y, E01, Const1,  $\Gamma$ 1]) /. fit2],
  {y, 1.1, 1.9}, PlotRange  $\rightarrow$  Full, PlotStyle  $\rightarrow$  Green];
```

```
Plot[{ $\rho$ [y, E01, Const1,  $\Gamma$ 1]} /. fit2,
  {y, 1.1, 2.0}, PlotRange  $\rightarrow$  Full, PlotStyle  $\rightarrow$  Green];
```

```
{E01  $\rightarrow$  1.27203, Const1  $\rightarrow$   $-2.47425 \times 10^{-8}$ ,  $\theta$ 1  $\rightarrow$  4.04241,  $\Gamma$ 1  $\rightarrow$  0.121044,
  E02  $\rightarrow$  1.42711, Const2  $\rightarrow$   $1.55486 \times 10^{-9}$ ,  $\theta$ 2  $\rightarrow$  -0.536708,  $\Gamma$ 2  $\rightarrow$  0.0337091}
```



```
{E01  $\rightarrow$  1.27203, Const1  $\rightarrow$   $-2.47425 \times 10^{-8}$ ,  $\theta$ 1  $\rightarrow$  4.04241,  $\Gamma$ 1  $\rightarrow$  0.121044,
  E02  $\rightarrow$  1.42711, Const2  $\rightarrow$   $1.55486 \times 10^{-9}$ ,  $\theta$ 2  $\rightarrow$  -0.536708,  $\Gamma$ 2  $\rightarrow$  0.0337091}
```

```
 $1.23205 \times 10^{-6}$ 
```

```
E01 + deltaE1
deltaE1 + E01
```

3 peak fitting

```
(*Triple peak fit*)
m = 3;
fitdata = xy[[1 ;; 460]];
ClearAll[E01]
deltaE = 0.15

fit3 = FindFit[fitdata, {A * E0^2 + B * E0 + C + PR[E0, E01, Const1,  $\theta$ 1,  $\Gamma$ 1] +
  PR[E0, E02, Const2,  $\theta$ 2,  $\Gamma$ 2] + PR[E0, E03, Const3,  $\theta$ 3,  $\Gamma$ 3]},
  {{A}, {B}, {C}, {E01, 1.27}, {Const1, 2.47424651245195`*^-8}, { $\theta$ 1, theta1},
  { $\Gamma$ 1, gamma1}, {E02, 1.42}, {Const2, 1.5548626772687124`*^-9}, { $\theta$ 2, theta2},
  { $\Gamma$ 2, gamma2}, {E03, 1.8}, {Const3, 1 * 10^-8}, { $\theta$ 3, .4}, { $\Gamma$ 3, .1}},
  E0, AccuracyGoal  $\rightarrow$  10, PrecisionGoal  $\rightarrow$  10, MaxIterations  $\rightarrow$  Automatic]

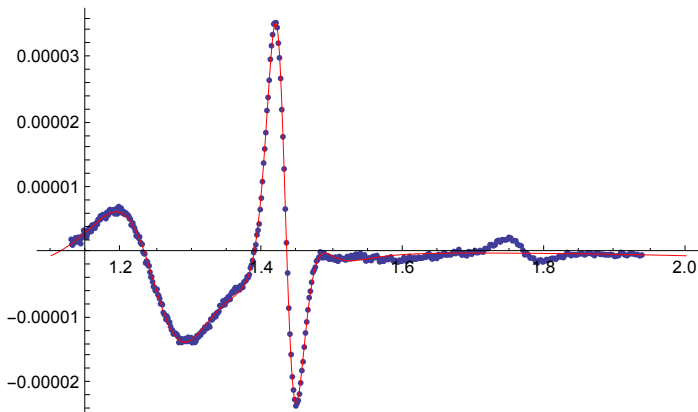
Show[ListPlot[fitdata, PlotRange  $\rightarrow$  All],
  Plot[Evaluate[(A * y^2 + B * y + C + PR[y, E01, Const1,  $\theta$ 1,  $\Gamma$ 1] +
    PR[y, E02, Const2,  $\theta$ 2,  $\Gamma$ 2] + PR[y, E03, Const3,  $\theta$ 3,  $\Gamma$ 3]) /. fit3],
  {y, 1.1, 2.0}, PlotRange  $\rightarrow$  Full, PlotStyle  $\rightarrow$  Red]]

Plot[Evaluate[( $\rho$ [y, E01, Const1,  $\Gamma$ 1]) /. fit2],
  {y, 1.1, 2.0}, PlotRange  $\rightarrow$  Full, PlotStyle  $\rightarrow$  Green];

Plot[({ $\rho$ [y, E01, Const1,  $\Gamma$ 1]) /. fit2},
  {y, 1.1, 2.0}, PlotRange  $\rightarrow$  Full, PlotStyle  $\rightarrow$  Green];
```

0.15

```
{A  $\rightarrow$  -5.03259  $\times$  10^-6, B  $\rightarrow$  0.0000176475, C  $\rightarrow$  -0.0000156206,
  E01  $\rightarrow$  1.25346, Const1  $\rightarrow$  2.05642  $\times$  10^-8,  $\theta$ 1  $\rightarrow$  0.396297,  $\Gamma$ 1  $\rightarrow$  0.114444,
  E02  $\rightarrow$  1.46113, Const2  $\rightarrow$  1.98402  $\times$  10^-9,  $\theta$ 2  $\rightarrow$  7.95636,  $\Gamma$ 2  $\rightarrow$  -0.0648032,
  E03  $\rightarrow$  1.42961, Const3  $\rightarrow$  2.23165  $\times$  10^-9,  $\theta$ 3  $\rightarrow$  -6.6072,  $\Gamma$ 3  $\rightarrow$  0.0367403}
```



4 peak fitting

```
(*Four peak fit*)
m = 3;
fitdata = xy[[1 ;; 460]];
ClearAll[E01, A, B, c]
deltaE = 0.15

fit4 = FindFit[fitdata,
  {A * E0^2 + B * E0 + c + PR[E0, E01, Const1,  $\theta$ 1,  $\Gamma$ 1] + PR[E0, E02, Const2,  $\theta$ 2,  $\Gamma$ 2] +
  PR[E0, E03, Const3,  $\theta$ 3,  $\Gamma$ 3] + PR[E0, E04, Const4,  $\theta$ 4,  $\Gamma$ 4]},
  {{A}, {B}, {c}, {E01, 1.2}, {Const1, .0000001}, { $\theta$ 1, theta1}, { $\Gamma$ 1, gamma},
  {E02, 1.42}, {Const2, .0000001}, { $\theta$ 2, theta2}, { $\Gamma$ 2, gamma2},
  {E03, 1.78}, {Const3, .00000005}, { $\theta$ 3, 0.227}, { $\Gamma$ 3, gamma},
  {E04, 1.5}, {Const4, .0000001}, { $\theta$ 4, theta1}, { $\Gamma$ 4, .15}},
  E0, AccuracyGoal  $\rightarrow$  8, PrecisionGoal  $\rightarrow$  8, MaxIterations  $\rightarrow$  200]

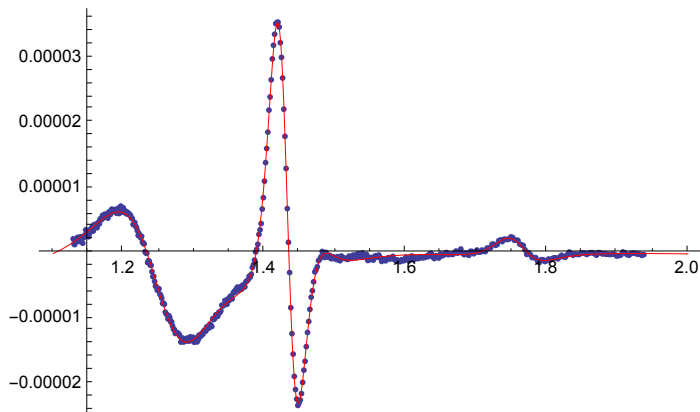
Show[ ListPlot[fitdata, PlotRange  $\rightarrow$  All], Plot[
  Evaluate[(A * y^2 + B * y + c + PR[y, E01, Const1,  $\theta$ 1,  $\Gamma$ 1] + PR[y, E02, Const2,  $\theta$ 2,  $\Gamma$ 2] +
  PR[y, E03, Const3,  $\theta$ 3,  $\Gamma$ 3] + PR[y, E04, Const4,  $\theta$ 4,  $\Gamma$ 4]) /. fit4],
  {y, 1.1, 2.0}, PlotRange  $\rightarrow$  Full, PlotStyle  $\rightarrow$  Red]]

Plot[Evaluate[( $\rho$ [y, E01, Const1,  $\Gamma$ 1]) /. fit2],
  {y, 1.1, 2.0}, PlotRange  $\rightarrow$  Full, PlotStyle  $\rightarrow$  Green];

Plot[({ $\rho$ [y, E01, Const1,  $\Gamma$ 1]) /. fit2,
  {y, 1.1, 2.0}, PlotRange  $\rightarrow$  Full, PlotStyle  $\rightarrow$  Green];

0.15

{A  $\rightarrow$   $-3.33471 \times 10^{-6}$ , B  $\rightarrow$  0.0000123033, c  $\rightarrow$  -0.0000115027,
  E01  $\rightarrow$  1.2551, Const1  $\rightarrow$   $2.00155 \times 10^{-8}$ ,  $\theta$ 1  $\rightarrow$  0.446281,  $\Gamma$ 1  $\rightarrow$  0.113518,
  E02  $\rightarrow$  1.42944, Const2  $\rightarrow$   $2.36083 \times 10^{-9}$ ,  $\theta$ 2  $\rightarrow$  -0.359819,  $\Gamma$ 2  $\rightarrow$  0.0372287,
  E03  $\rightarrow$  1.75693, Const3  $\rightarrow$   $4.85926 \times 10^{-10}$ ,  $\theta$ 3  $\rightarrow$  -0.800407,  $\Gamma$ 3  $\rightarrow$  0.0583703,
  E04  $\rightarrow$  1.45924, Const4  $\rightarrow$   $-1.7745 \times 10^{-9}$ ,  $\theta$ 4  $\rightarrow$  -5.02666,  $\Gamma$ 4  $\rightarrow$  0.0601303}
```

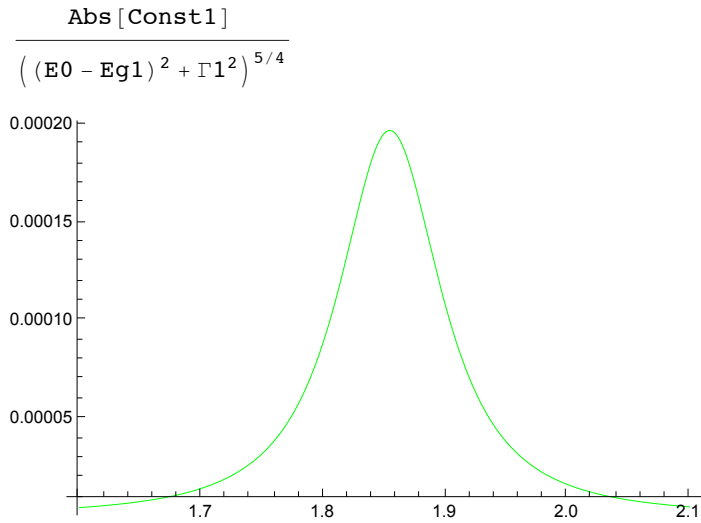


Fitting

Fitting and Plotting the PR modulus

$$\rho[E_0, E_{g1}, \text{Const1}, \Gamma_1] = \text{Abs}[\text{Const1}] / ((E_0 - E_{g1})^2 + \Gamma_1^2)^{(m/2)}$$

```
Plot[\rho[y, E_{g1}, \text{Const1}, \Gamma_1] /. fit, {y, 1.6, 2.1}, PlotRange -> Full, PlotStyle -> Green]
```



Overlay the fit and the PR modulus

```
Show[ListPlot[fitdata, PlotRange -> All],
Plot[Evaluate[PR[y, E_{g1}, \text{Const1}, \Theta_1, \Gamma_1] /. fit], {y, 1.6, 1.9},
PlotRange -> Full, PlotStyle -> Red], Plot[\rho[y, E_{g1}, \text{Const1}, \Gamma_1] /. fit,
{y, 1.6, 1.9}, PlotRange -> Full, PlotStyle -> Green]]
```

